

Development and Verification of a CFD Based Simulation Software for Floating Offshore
Wind Turbines

A Dissertation

Presented in Partial Fulfillment of the Requirements for the

Degree of Doctorate of Philosophy

with a

Major in Mechanical Engineering

in the

College of Graduate Studies

University of Idaho

by

Sean M. Quallen

Major Professor: Tao Xing, Ph.D.

Committee Members: Ralph Budwig, Ph.D.; John Crepeau, Ph.D.; Jim Liou, Ph.D.

Department Administrator: Steven Beyerlein, Ph.D.

August, 2015

AUTHORIZATION TO SUBMIT DISSERTATION

This dissertation of Sean M Quallen, submitted for the degree of Doctor of Philosophy with a Major in Mechanical Engineering and titled "Development and Verification of a CFD Based Simulation Software for Floating Offshore Wind Turbines," has been reviewed in final form. Permission, as indicated by the signatures and dates below, is now granted to submit final copies to the College of Graduate Studies for approval.

Major Professor: _____ Date: _____
Tao Xing, Ph.D.

Committee
Members: _____ Date: _____
Ralph Budwig, Ph.D.

_____ Date: _____
John Crepeau, Ph.D.

_____ Date: _____
Jim Liou, Ph.D.

Department
Administrator: _____ Date: _____
Steven Beyerlein, Ph.D.

ABSTRACT

A coupled aerodynamic-hydrodynamic-servo simulation software capable of motion and performance predictions for floating offshore wind turbines (FOWT) is developed. The computational fluid dynamics (CFD) solver CFDSHIP-IOWA is used for pressure, velocity, and motion predictions. A multi-segmented mooring line model (crowfoot) is designed for securing the turbine and limiting motions. Variable-speed (VS) and blade-pitch (BP) controllers designed by the National Renewable Energy Laboratory (NREL) are also utilized to help maximize power and to prevent generator overload.

The developed software is demonstrated with multiple simulation load cases (LC) from the Offshore Code Comparison Collaboration (OC3), increasing complexity with each simulation. Free-decay tests are first performed for hydrodynamic validation against experimental data provided by the OC3 using a coarse grid set. A URANS simulation featuring steady wind and regular wave patterns, modeled after the OC3's LC 5.1, is performed with a fixed rotor rotational velocity. The motion and aerodynamic power predictions are compared to those of NREL's OC3 results.

A finer gridset is constructed and utilized in a study of offshore blade-tower interaction (BTI) to determine the effect of unsteady platform motions on the aerodynamic disruption caused by the blade passing directly upwind of the tower. The results show that BTI effects are strongly affected by platform motions, notably in pitch, and that BTI is more significantly affected by platform velocities than by overall displacements.

This finer gridset is again utilized, but combined with a VS controller in a duplicate LC 5.1 simulation using DDES. The drivetrain is modeled with rotational inertia allowing for prediction of the rotor velocity based on developed generator torque. Generator torque and power predictions are compared to NREL's results. The present results agree in frequency trends but predict separation on blades during platform upstream pitching and surging.

The BP controller is employed in a simulation modeled after the OC3's LC 5.2, which uses irregular waves and the Mann wind turbulence model. Results are transformed to the frequency domain for comparison with NREL. The present results agree with NREL generated torque and power. Grid dissipation and modeling error in the present study produce less overall wind and wave fluctuations.

ACKNOWLEDGEMENTS

First, and foremost, I wish to express gratitude to my major professor Tao Xing, who stood by me and guided me throughout this dissertation. I would never have achieved this work without his support and advice over the past few years. Appreciation is also extended to the members of my committee—John Crepeau, Jim Liou, and Ralph Budwig, for devoting their time and efforts to this composition. Thanks go to both the Idaho National Laboratory and the National Institute for Computational Sciences for providing computing resources and help. This dissertation was partially funded by the National Science Foundation under the project title "Simulation Based Design for Deep Water Offshore Wind Turbines Including Wave loads and Motions" (award #1066873) and partially by the University of Idaho-College of Engineering. Appreciation is extended to both of these entities for their support. Simulations were performed using the Idaho National Laboratory's Falcon HPC, an SGI ICE machine with 16,416 cores. Thanks go to both of these organizations for their assistance and resources.

It would be impossible to produce an exhaustive list of all of the individuals who helped during the day-to-day details and development of this work, and this list is not intended to leave anyone out. A thank you, for their assistance and support, is offered to Becky Schoenberg, Elaine Queener, Molly Steiner, Joseph George, Adam Oster, Jose Ramirez, Rory Lilley, Sam Wos, John Kawula, Matthew Riley, Mike Anderson, Dan Cordon, and Peter Cebull.

DEDICATION

To Sarah, Julius, and Guenevere: You never left my side with your love and compassion and I will be forever grateful.

TABLE OF CONTENTS

Authorization to Submit Dissertation	ii
Abstract.....	iii
Acknowledgements.....	v
Dedication.....	vi
Table of Contents.....	vii
List of Figures.....	xii
List of Tables.....	xvi
Abbreviations.....	xvii
CHAPTER 1: INTRODUCTION.....	1
1.1 Abstract.....	1
1.2 Offshore Wind in the United States.....	1
1.3 Status of Offshore Technology.....	2
1.4 Floating Offshore Wind Turbine Simulation.....	4
1.5 Objective.....	7
1.6 Dissertation Organization	7
1.7 Figures	9
CHAPTER 2: BASE CFD SOLUTION SOFTWARE AND METHODS	10
2.1 Abstract.....	10
2.2 Fluid Solution Module.....	10
2.2.1 URANS Governing Equations.....	10
2.2.2 Turbulent Modeling.....	11
2.2.3 Numerical Methods	11

2.3 Turbine Motion Prediction Module	12
2.4 Free-Surface Modeling	14
2.5 Overset Grid Capabilities	15
2.6 Solution Strategy	15
2.7 Figures	17
CHAPTER 3: OC3-HYWIND DETAILS AND GRID SETS	18
3.1 Abstract.....	18
3.2 OC3-Hywind Geometry.....	18
3.3 Grid Design.....	20
3.4 Figures	24
3.5 Tables.....	36
CHAPTER 4: DEVELOPMENT AND VALIDATION OF A QUASI-STATIC CROWFOOT MOORING-LINE MODEL	39
4.1 Abstract.....	39
4.2 Introduction.....	39
4.3 Mathematical Modeling and Methods	40
4.3.1 OC3-Hywind Mooring Models.....	40
4.3.1.1 2-Point, Single-line, 2D Model.....	41
4.3.1.2 OC3 Added Yaw Stiffness Model	42
4.3.1.3 Crowfoot Model.....	42
4.3.2 Numerical Methods and Solution Strategy.....	46
4.4 Simulation Conditions and Design	46
4.5 Results and Discussion	47
4.5.1 Case 1.4 Tests	47
4.5.2 Case 5.1 Tests	48

4.6 Conclusions.....	51
4.7 Figures	53
4.8 Tables.....	63
CHAPTER 5: AN INVESTIGATION OF THE BLADE TOWER INTERACTION OF A FLOATING OFFSHORE WIND TURBINE.....	64
5.1 Abstract.....	64
5.2 Introduction.....	64
5.3 Mathematical Modeling and Methods	66
5.3.1 Numerical Methods and Solution Strategy.....	66
5.4 Simulation Conditions and Design	66
5.5 Results and Discussion	68
5.6 Conclusions.....	71
5.7 Future Work.....	72
5.8 Figures	73
5.9 Tables.....	81
CHAPTER 6: CFD SIMULATION OF A FLOATING OFFSHORE WIND TURBINE SYSTEM USING A VARIABLE-SPEED GENERATOR-TORQUE CONTROLLER	82
6.1 Abstract.....	82
6.2 Introduction.....	82
6.3 Mathematical Modeling and Methods	83
6.3.1 Geometry	83
6.3.2 Drivetrain Modeling	83
6.3.3 Variable-Speed Generator-Torque Controller	85
6.3.4 Numerical Methods and Solution Strategy.....	86
6.4 Simulation Conditions and Design	86

6.5 Results and Discussion	87
6.5.1 Overview of Flow Field.....	87
6.5.2 Cases 1 and 2	88
6.5.3 Case 3.....	90
6.6 Conclusions.....	93
6.7 Figures	95
6.8 Tables.....	100
CHAPTER 7: CFD SIMULATION OF A FLOATING OFFSHORE WIND TURBINE SYSTEM EXPERIENCING IRREGULAR WAVES AND INCOMING WIND TURBULENCE.....	102
7.1 Abstract.....	102
7.2 Introduction.....	102
7.3 Mathematical Modeling.....	106
7.3.1 Blade-Pitch Controller	106
7.3.2 JONSWAP Irregular Waves	108
7.3.3 Mann Turbulence Model	109
7.4 Simulation Conditions and Design	113
7.5 Results and Discussion	114
7.5.1 Case 1.....	114
7.5.2 Case 2.....	117
7.5.3 Case 3.....	121
7.6 Conclusions.....	125
7.7 Figures	127
7.8 Tables.....	134
CHAPTER 8: CONCLUSIONS AND FUTURE WORK	137

REFERENCES	140
APPENDICES	147
A1: Mooring Line Code (Fortran 90)	147

LIST OF FIGURES

Figure 1 Three dominant platform designs. (<i>Source: DOE</i>)	9
Figure 2 Base CFD solution strategy.....	17
Figure 3 Overall OC3-Hywind geometric details.....	24
Figure 4 Combined tower and platform geometry	25
Figure 5 Nacelle geometry.....	26
Figure 6 Hub geometry.....	26
Figure 7 Blade geometry showing airfoil section profiles.....	27
Figure 8 Airfoil profiles along length of blade from root (blue) to tip (red).....	27
Figure 9 Coarse grid set mid-plane slice. 5 grid points skipped in all directions in all grids	28
Figure 10 Fine grid set mid-plane slice. 5 grid points skipped in all directions in all grids..	29
Figure 11 Combined tower and platform grids. (left) Coarse grid, (right) fine grid	30
Figure 12 Nacelle grids. (left) Coarse grid, (right) fine grid	31
Figure 13 Hub grids. (left) Coarse grid, (right) fine grid.....	31
Figure 14 Composite coarse blade grid with sub-component grids	32
Figure 15 Composite fine blade grid with sub-component grids	33
Figure 16 Coarse blade refinement grid with embedded coarse blade grid	34
Figure 17 Wake refinement grids. 5 grid points skipped in all directions for clarity. (left) coarse grid, (right) fine grid.....	34
Figure 18 Background grids. 5 grid points skipped in all directions for clarity. (left) coarse grid, (right) fine grid.....	35

Figure 19 Catenary mooring line configurations and coordinate frames: (a) 2-Point line fairlead connections (from above), (b) Crowfoot line fairlead connections (from above)	53
Figure 20 Two-dimensional catenary forces and line configurations. (reproduced from (Jonkman, 2007)): (a) Line resting on seabed,(b) Taut line,(c) Slack line	54
Figure 21 Crowfoot connection to fairleads with descriptions.....	54
Figure 22 Crowfoot XY plane angles	55
Figure 23 Broyden's method solution process	55
Figure 24 Solution strategy.....	56
Figure 25 Surge, heave, pitch, and yaw results in cases 1.4b and 1.4c	57
Figure 26 Surge and yaw restoring comparison of a single crowfoot line and a single AYS line	58
Figure 27 Net restoration comparison of crowfoot and AYS mooring lines.....	58
Figure 28 Platform motions in case 5.1	59
Figure 29 Fourier transform of yaw motions from case 5.1	59
Figure 30 Power and thrust time histories in case 5.1	60
Figure 31 Predicted vortical structures (iso-surfaces of $Q=0.5$ colored by pressure). Free-surface is maximum (3 m) in light gray and minimum (-3 m) in dark gray.....	61
Figure 32 Aerodynamic effects of tower on pressure contours at $r/R=0.2$ along the blade length: (a) Blade passing in front of tower, (b) Blade 180° from tower.....	62
Figure 33 Three coordinate frames: earth-fixed frame (X,Y,Z), turbine system frame (x_T, y_T, z_T), and 2-D blade section system.....	73
Figure 34 Three different configurations used	74

Figure 35 Azimuth vs. shaft thrust for R1	74
Figure 36 Azimuth vs. shaft thrust for R2	75
Figure 37 Azimuth vs. shaft thrust for R3	75
Figure 38 Azimuth vs. shaft thrust for R4	76
Figure 39 C_P differences for R1	76
Figure 40 C_P differences for R2	77
Figure 41 C_P differences for R3	77
Figure 42 C_P differences for R4	78
Figure 43 Q-isosurface of 1x simulation in R1 colored by C_P	79
Figure 44 Q-isosurface of no TNP simulation in R1 colored by C_P	80
Figure 45 Three coordinate systems: earth-fixed frame (X, Y, Z), turbine system frame (x_T , y_T , z_T), and rotor system (x_R , y_R , z_R)	95
Figure 46 Drivetrain schematic	95
Figure 47 Generator torque vs. generator speed response of the variable-speed controller (Reproduced from (Jonkman, 2009) with edits from (Jonkman, 2010))	96
Figure 48 Solution strategy including VS controller module	96
Figure 49 3D views of turbine and Q=1 isosurfaces in (a), (b), (c) (d) Streamwise velocity contours	97
Figure 50 Comparison of torque and speed predictions of case 1, case 2, and NREL-FAST97	
Figure 51 Comparison of platform motions between case 3 and NREL-FAST	98
Figure 52 Comparisons of aerodynamic torque and generator predictions between case 3 and NREL-FAST	98

Figure 53 Limiting streamlines on suction side of blade, colored by C_p . (a) Maximum downstream platform velocity; (b) Maximum upstream velocity	99
Figure 54 Outboard 20% of blade showing limiting streamlines and colored by C_p . (a) Maximum downstream platform velocity; (b) Maximum upstream velocity. Inset shows detail of separation zone at 82% blade span.....	99
Figure 55 Solution strategy including VS and BP controller modules.....	127
Figure 56 PSD of wave elevation in case 1 compared to that of NREL	127
Figure 57 Platform motion PSD plots of case 1 compared to NREL.....	128
Figure 58 Time history of streamwise velocity at hub height for cases 2 and 3	128
Figure 59 Contours of normalized streamwise velocity at inlet, mid-plane, and outlet.....	129
Figure 60 PSD plots of turbulent wind velocity components.....	129
Figure 61 PSD plots of generator predictions of case 2 compared to those of NREL	130
Figure 62 Platform motion PSD plots of case 3 compared to NREL.....	131
Figure 63 Generator prediction PSD plots of case 3 compared to NREL.....	132
Figure 64 Limiting streamlines on suction side of blade at maximum upstream velocity ..	132
Figure 65 Clockwise from top-left: Rear view with isosurfaces of $Q=1$; Top view with $Q = 1$ and wave surface; Top-front view with $Q=0.5$; Streamwise velocity contours at $Y=0$ slice	133

LIST OF TABLES

Table 1 Structural and geometric details	36
Table 2. Coarse grid names and points with directions	37
Table 3. Fine grid names and points with directions	38
Table 4 Mooring model properties	63
Table 5. Simulation matrix.	63
Table 6 Descriptions of motion regions R1-R4.....	81
Table 7 Thrust loss of 1x & 2x simulations compared to No TNP in kN	81
Table 8. Drivetrain Properties.....	100
Table 9. VS controller control regions with corresponding generator and rotor speeds	100
Table 10. Simulation case matrix	100
Table 11 Comparison of motions and power characteristics between case 2, case 3, and NREL.....	101
Table 12 Simulation case matrix	134
Table 13 Wave elevation and platform motions of case 1 compared to those of NREL.....	134
Table 14 Statistics of wind field of case 2 and case 3 compared to those of NREL	135
Table 15 Generator predictions of case 2 compared to those of NREL	135
Table 16 Platform motion of case 3 compared to those of NREL.....	136
Table 17 Generator predictions of case 3 compared to those of NREL	136

ABBREVIATIONS

6-DOF	six rigid-body degrees of freedom
AYS	augmented yaw stiffness
BP	blade-pitch
BEM	blade-element momentum
BTI	blade tower interaction
CFD	computational fluid dynamics
DDES	delayed detached eddy simulation
DOE	Department of Energy
DOF	degree of freedom
FAST	fatigue, aerodynamics, structure, and turbulence (NREL software)
FOWT	floating offshore wind turbine
GSPI	gain-scheduled proportional-integral
GWEC	Global Wind Energy Council
HSS	high-speed shaft
IEA	International Energy Agency
IEC	International Electrotechnical Commission
JONSWAP	Joint North Sea Wave Project
LC	load case
LSS	low-speed shaft
MIMOSS	multiple-input multiple-output state-space
NREL	National Renewable Energy Laboratory

NSE	Navier-Stokes equations
OC3	Offshore Code Comparison Collaboration
PSD	power spectral density
SST	shear stress transport
SWL	still water line
TE	trailing edge
TNP	tower-nacelle-platform
URANS	unsteady Reynolds-averaged Navier-Stokes
VS	variable-speed

CHAPTER 1: INTRODUCTION

1.1 Abstract

An introduction to offshore wind power is presented along with a brief status of current technology. The importance of simulation is emphasized, leading to the objective of this dissertation as a whole. Finally the organization of the dissertation, highlighting the incremental process followed throughout the entire software development, is provided.

1.2 Offshore Wind in the United States

Wind power has been adopted as a clean utility-scale renewable source of energy both globally and domestically. Installed capacity has grown on an exponential scale since 2000. At year end 2014 the global cumulative installed wind capacity reached 369.6 GW with the United States reaching 65.8 GW of installed capacity (GWEC, 2015), all of which is land-based. As technologies mature the US has begun looking offshore for wind energy extraction. Offshore wind power provides many advantages over land-based wind turbines, including large continuous areas suitable for farm deployment, higher and steadier wind velocities, and less wind turbulence, all of which promote increased efficiency and reliability (Musial et al., 2010). Offshore capacity is also recognized for the potential of alleviating aesthetic and noise concerns by relocating turbines far away from population. NREL has reported that 4,150 GW of offshore wind power is available within 50 nautical miles of the country's coastlines (Schwartz et al., 2010), approximately 4 times the current US usage. Most of this power, however, comes from waters too deep to feasibly fix a turbine to the seabed and floating structures become a necessity (Musial et al., 2010). The Department of Energy (DOE) envisions a potential 86 GW of offshore capacity by 2050 in their *Wind Vision* report (DOE, 2015), which can provide extra capacity to highly populated coastal areas and onshore regions, notably the southeastern US, where wind resources are low. Efforts to achieve this goal require continued technological development and predictions to help offset the increased capital costs and physical uncertainties associated with offshore wind capacity (Fingersh et al., 2006). This dissertation aims to aid in these efforts.

1.3 Status of Offshore Technology

Offshore wind power is being investigated by multiple countries worldwide, especially as turbine technology has matured over the past few decades. Fixed base offshore turbines were first installed at the Vindeby Wind Farm off the northern shore of Denmark—11 turbines with a 5 MW total capacity—in 1991 (Burton, 2011). Contrast this with large modern farms such as the Gwynt y Môr Wind Farm off the northern shores of Wales with a 576 MW total capacity, expected to power about 40% of the homes in Wales and scheduled to be commissioned in mid-2015 (RWE Innogy, 2014). In the US initial manufacturing has begun, in mid-2015, on the Block Island Wind Farm (Deepwater Wind, 2015), expected to be in service in late 2016. The Block Island farm, featuring 5 fixed-base turbines, is expected to produce 0.03 GW of power, a mere 1% of the 3 GW of offshore power required by 2020 as laid out in the DOE's *Wind Vision* (DOE, 2015). This makes the DOE's goal of 86 GW by 2050 that much more aggressive. Siting concerns regarding noise, visual aesthetics, shipping lanes, and marine ecology have made waters farther from shore attractive, and FOWT technology will probably be required in order to meet these goals. Other countries with deeper waters, notably China and most countries in Western Europe, are also exploring FOWT technologies to access and exploit deep-water wind resources.

Designing offshore wind technology offers significant challenges. This is especially true for floating offshore wind turbines (FOWT) where buoyant stability and mooring system forces are introduced on top of the already complex coupling of aerodynamic and oceanic-hydrodynamic loadings. Motion of the floating platform produces unsteady aerodynamic forces on all solid surfaces of the turbine. While pitching and surging (downstream translation) additional velocities are superimposed onto the velocities experienced from simple rotor rotation. These additional velocities also switch sign as the system shifts between upstream motion and downstream motion, most notably due to platform pitching, which produces an oscillation at the same frequency as the pitching motion. The pitching motion frequency is strongly correlated to wave excitation.

Multiple floating platform designs have been identified by the research community, typically classified by stability concept. The three platform designs, which are generally

considered to be the most viable current designs (see (NREL, 2011)), are shown in Figure 1. Spar-buoy platforms utilize a deep-draft slender cylindrical hull, heavily ballasted with a center of gravity well below the center of buoyancy for stability. In this configuration the catenary mooring lines are mostly passive and simply ensure the turbine doesn't drift. The spar-buoy platform is recognized for its design simplicity and low-cost of anchoring, but is subject to complex platform motions and becomes a less viable platform as water depth increases due to increased mooring line costs (Musial et al., 2003). While the spar-buoy platform uses ballast for stability, the semi-submersible platform (center of Figure 1) utilizes a large water-plane area increasing geometric inertial moments and, therefore, increasing buoyant restoration in pitch. The increased platform area also pushes mooring fairleads farther from the platform's principal rotation axes, such that catenary mooring lines also play a role, albeit smaller, in platform stability. Semi-submersible platforms use significantly less material than their spar-buoy counterparts and can be installed in shallower waters as they feature less draft than the spar-buoy design. However the semi-submersible platform is exposed to more wave excitation due to this increased water-line footprint and may not be sufficiently damped to effectively stop platform pitching motions (Jonkman, 2007). Advanced control algorithms can be used to avoid these large scale platform pitching motions, but these algorithms run the risk of increasing blade and tower bending fatigue or decreasing aerodynamic efficiency depending on optimization set-point (Jonkman et al., 2008, Namik et al., 2010, Lackner, 2013). Also presented at right in Figure 1 is the tension-leg platform (TLP) which utilizes mooring tension as the primary source of platform stability. The TLP is subject to less wave excitation than either the spar-buoy or semi-submersible as the bulk of the platform is well below the surface, which minimizes platform motions and, subsequently, blade and tower fatigue loading. The TLP also may also be more cost efficient in deeper waters due to shorter mooring line lengths than the slack, catenary mooring designs (Musial et al., 2003). TLP designs, however, have high installation costs and increased anchoring requirements (Musial et al., 2003, Matha, 2010).

The compromises inherent with each platform design, coupled with individual site conditions and concerns, make FOWT platform design a rich and active area of study. However, as of mid-2015, the only two utility-scale FOWT models in service (both as

prototypes) are Statoil's Hywind (Skaare et al., 2011, Skaare et al., 2015) and Principle Power's WindFloat (Principle Power, 2011). The Hywind, floating in the North Sea 10 km off the southwestern coast of Norway, is a 2.3 MW turbine utilizing a slender spar-buoy platform and has successfully been in service since June 2009. The 2MW WindFloat was installed 5 km off the shores of Portugal in October 2011 and is floating upon a semi-submersible platform. Both of these prototypes are standalone units; all existing offshore farms utilize fixed-base turbine platforms in shallower, calmer waters. The relatively short service lives and proprietary nature of these two full-scale turbines have produced little data for the research community at large. Results from experiments using scale models are similarly frustrating as the rotor should be scaled down using Reynolds similarity to maintain the proper ratio between inertial forces and viscous forces, but the platform should be scaled using Froude similarity to maintain the ratio between inertial forces of the incident waves and gravitational forces (Robertson et al., 2013). Various methods have been investigated for overcoming this issue. The scaling differences can simply be ignored, as was done by Robertson et al in (Robertson et al., 2013), where a TLP model was scaled using only Froude similarity for both air and water phases. The authors noted that Froude scaling reduced the Reynolds number of the study by 3 orders of magnitude, which they assumed to bring the flow from a turbulent regime to a laminar regime. In (Martin, 2011) and followed by (De Ridder et al., 2014) the authors made attempts to alter the blade airfoil profiles of the scaled model in order to more closely match the aerodynamic performance of the full-scale model. It is unclear if this method allows design modifications at the model-scale which translate properly to the full-scale. In both of these studies the results were compared to "full-scale" results from NREL's FAST wind turbine simulation software (Jonkman et al., 2005). One thing is clear from all of these studies: accurate or viable experimental FOWT data may not be readily available, and the importance of accurate simulation data cannot be understated.

1.4 Floating Offshore Wind Turbine Simulation

Accurate simulation of offshore wind technology is a substantial task, particularly with very limited large-scale experimental data. With this in mind ten countries participated in the International Energy Agency (IEA) approved Task 23 subtask 2: The Offshore Code

Comparison Collaboration (OC3). The OC3 performed simulations of four offshore wind turbines using various software packages and then compared results with the intent of facilitating improvements in models or analysis methodologies. Only one FOWT was investigated by the OC3: A spar-buoy concept referred to as the OC3-Hywind. This system was chosen for study in the OC3's Phase IV due to its simplicity and potential for validation against the smaller full-scale Hywind from Statoil (Jonkman, 2010, Statoil, 2012).

Predictions of power and motions require accurate predictions of loading, both aerodynamic and hydrodynamic. Most FOWT simulations to date, including all simulations presented in the OC3's results, have used the blade-element momentum theory (BEM), explained in detail in (Burton, 2011), to determine aerodynamic loading on the rotor and Morison's equation (Morison et al., 1950) to determine hydrodynamic loading on the platform. The certified wind turbine simulator code FAST from NREL (Jonkman et al., 2005), widely used in both the industry and research communities and compared to in this dissertation, uses BEM and Morison's equation. BEM is a 2-dimensional lookup-table method utilizing empirically determined lift and drag coefficients and other correction models, such as dynamic stall and wake models. BEM was developed for analysis of flow perpendicular to the rotor plane. As such BEM, and its current corrections, may not be appropriate for general purpose offshore simulations given the varying yawed inflow conditions, dynamic stall, and potential for rotor-wake interaction (Sebastian et al., 2010, Matha et al., 2013). BEM, as designed, also does not consider the tower geometry and requires a correction model to account for the presence in the tower in wake deficit and blade-tower aerodynamic disruption (Bak et al., 2001, Quallen et al., 2015). Morison's equation is a 1-dimensional, semi-empirical function developed to determine hydrodynamic loading, requiring experimentally derived added mass and drag coefficients for any given geometry. It has no mechanism for viscous effects or hydrostatic restoring forces in the vertical and transverse directions. Morison's equation assumes the diameter of the structure is small relative to incident wavelength such that wave diffraction effects, caused by wave/structure interaction at the platform can be neglected. This is not appropriate for many FOWT platforms, notably buoyancy stabilized platforms such as barges and semi-submersibles (Matha et al., 2011,

Kvittem et al., 2012). The use of computational fluid dynamics (CFD) can help to overcome the limitations of BEM and Morison's equation.

With CFD the governing Navier-Stokes equations (NSEs) are discretized spatially and temporally into algebraic equations and solved. CFD can intrinsically solve in 3-dimensions, requiring empirical corrections only to determine turbulent characteristics, and can provide details of flow physics that BEM and Morison's equation cannot. With computational resources becoming more readily available, especially parallel-computing resources, finer resolution of both time and space discretization can be accomplished, allowing CFD to scale in a way that correction models may not be able to. 3-dimensional aerodynamic CFD simulations of a wind turbine require a relative rotational motion between a blade or rotor and the surrounding fluid. This presents a challenge to the usage of CFD as many solvers require static grids and cannot model dynamic geometric situations, such as an accelerating rotor. Techniques such as overset or "chimera" meshing (Steger et al., 1987) and sliding mesh (Sánchez-Caja et al., 1999) have been employed for the purposes of platform motion and rotor rotation relative to the tower. The most notable application of CFD to wind turbine technology to date are simulations based on NREL's onshore unsteady phase VI experiments (NREL, 2001, Zahle et al., 2009, Li et al., 2012). In these experiments the tower was fixed and the rotational velocity of the rotor was prescribed, making the dataset excellent for code validation. In service, however, the rotational velocity of the rotor is certainly not prescribed. The component of velocity provided by rotor rotation to the blade is usually the dominating component of overall magnitude, particularly on the outboard span of long blades like those used on FOWT. The rotor rotational velocity and developed aerodynamic torque cannot be de-coupled, especially considering underlying platform motions providing unsteady aerodynamic loading. Control mechanisms, which optimize power extraction in conditions below rated and protect against generator and fatigue overloading in conditions above rated, also play a significant role in the rotational velocity of the rotor and cannot be neglected from simulations. One of the main functions of these control strategies is to determine the distribution of developed aerodynamic torque between torque extracted at the generator and torque allowed to accelerate the rotor. Thus predictions of generator torque and aerodynamic loading, both stemming from aerodynamic torque developed by the rotor,

also cannot be de-coupled and require an inertial model of the drivetrain to predict rotor acceleration.

1.5 Objective

This dissertation aims to overcome these limitations by developing a CFD-based simulation software capable of predicting aerodynamic and hydrodynamic loading and response of a FOWT. The software is constructed with force prediction capability of multiple catenary mooring line configurations and uses VS and BP controller modules for predictions of generator power and torque as well as predictions of rotor rotational velocity. The software can also utilize design-specification empirical wind turbulence and irregular wave models for more accurate or configurable, site-specific predictions. The author is unaware of, to date, any CFD-based software complete with all of these capabilities.

1.6 Dissertation Organization

An incremental approach is followed in development, with levels of complexity added for each chapter. In each of chapters 3 through 7 the OC3-Hywind (Jonkman et al., 2009, Jonkman, 2010) is chosen as the representative turbine model for simulation considering a large quantity of OC3-Hywind simulation data from multiple independent entities is available for various levels of verification. A discussion of the preexisting capabilities of CFDSHIP-IOWA, the base CFD solution software used in this dissertation, is provided in chapter 2. The geometry and relevant details of the OC3-Hywind are presented in chapter 3 along with details of grid sets used.

In chapter 4 a crowfoot mooring model is developed and validated against experimental data. A simulation of the modeled FOWT—featuring steady winds and regular incoming waves as per OC3 LC 5.1 but with a time-averaged fixed rotor velocity—is performed utilizing the crowfoot mooring model for securing the platform. Motion and aerodynamic power results are compared to those of NREL for verification of the crowfoot model in service.

In chapter 5 the spatial resolution of the grid set components is significantly increased and this updated grid set is used for an examination of BTI of FOWT. Sinusoidal surge and pitch

motions are prescribed for the platform and the rotor is given a fixed rotational velocity. Three geometric configurations are tested to determine the effect of the distance between the rotor and tower on blade aerodynamics. Motions are partitioned into four regions, each corresponding to 90° of phase, and results are analyzed for each of these motion regions.

In chapter 6 the drivetrain components are given rotational inertia and a VS controller is implemented and employed supplying generator torque and power predictions. A simulation with OC3 LC 5.1 wind and wave conditions is again run using the refined grid set. Rotor rotational velocity is predicted based on an equation of motion applied to the drivetrain. Motion and power predictions are compared to NREL's results for verification of the VS controller.

In chapter 7 the BP controller is implemented and utilized in a simulation with OC3 LC 5.2 conditions, which includes irregular waves based on the JONSWAP spectrum and wind turbulence. The Mann turbulent wind model (Mann, 1998) is used to provide empirically-based stochastic fluctuations to the mean freestream velocity, which is set to the turbine's rated streamwise velocity. Results of this simulation are transformed, via FFT, to the frequency-domain for comparison to NREL's OC3 LC 5.2 results for verification of the BP controller.

Overall conclusions and potential future developments are discussed in chapter 8.

1.7 Figures

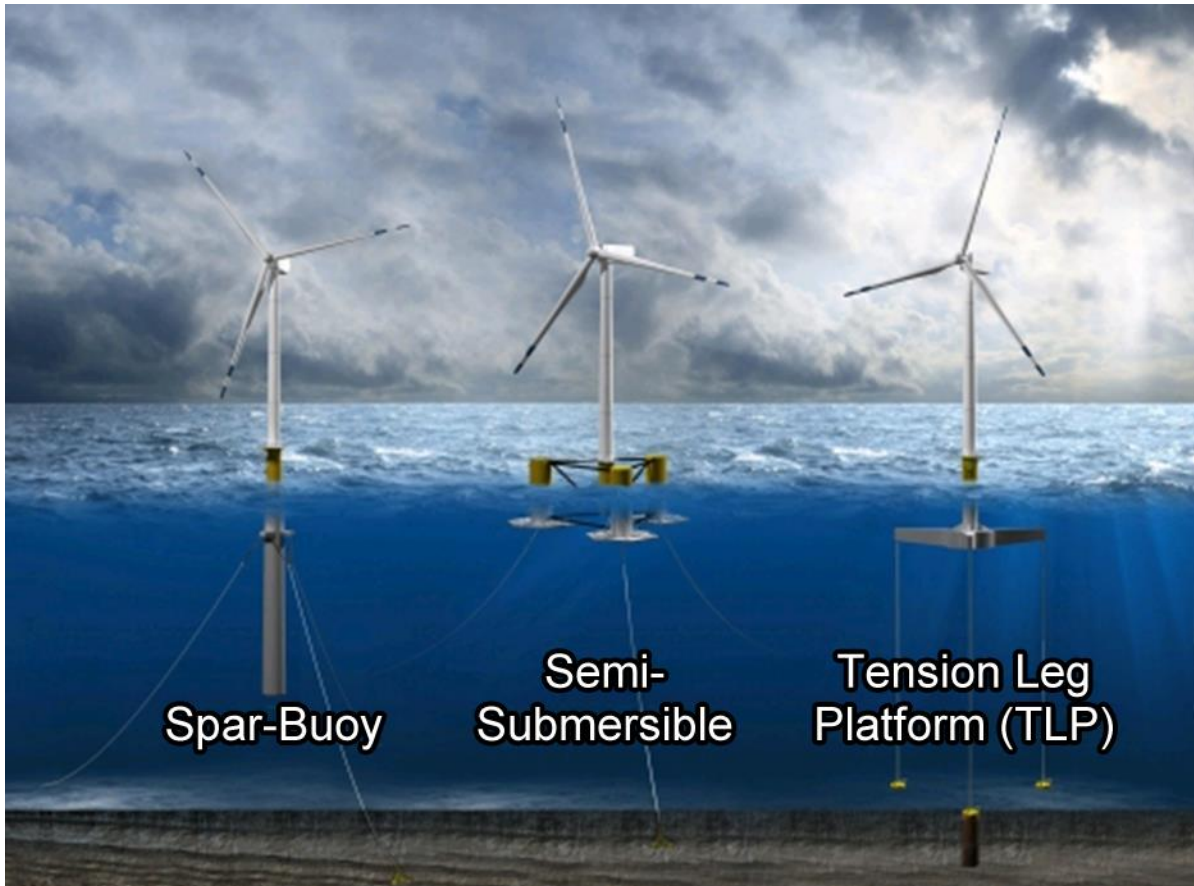


Figure 1 Three dominant platform designs. (Source: DOE)

CHAPTER 2: BASE CFD SOLUTION SOFTWARE AND METHODS

2.1 Abstract

The capabilities of the CFD solver used in this dissertation, CFDSHIP-Iowa v4.5, are explained. The governing equations and methods used by the fluid velocity and pressure solver, including turbulence modeling, are laid out. Similar descriptions are provided for the 6-DOF rigid-body motion prediction module and the free-surface location prediction module, both utilized extensively in this dissertation. A brief description of the overset capabilities of CFDSHIP-Iowa is also provided. Finally the overall CFD solution strategy and process, prior to amendments in subsequent chapters, is presented visually and described.

2.2 Fluid Solution Module

2.2.1 URANS Governing Equations

CFDSHIP-Iowa v4.5 provides a general purpose unsteady Reynolds-Averaged Navier-Stokes (URANS) finite-difference solver (Huang et al., 2008), featuring a two-phase solution module for simulations where both aerodynamics and hydrodynamics must be considered, such as those considering FOWT. Across all simulations in this dissertation the maximum freestream Mach number experienced is 0.05 and the maximum Mach number experienced at the blade tip is 0.25. Accordingly all air velocities are assumed to remain within the incompressible regime (i.e. Mach number below ~ 0.3) such that the mass and momentum conservation equations for both air and water are:

$$\nabla \cdot \mathbf{u} = 0 \quad (2.1)$$

$$\frac{\partial \mathbf{u}}{\partial t} + \mathbf{u} \cdot \nabla \mathbf{u} = -\nabla \hat{p} + \nabla \cdot \left[\frac{1}{\text{Re}_{eff}} (\nabla \mathbf{u} + \nabla \mathbf{u}^T) \right] \quad (2.2)$$

where \mathbf{u} is the fluid velocity, \hat{p} is the piezometric pressure, and Re_{eff} is the effective Reynolds number, which are defined as

$$\hat{p} = \frac{p}{\rho U_0^2} + \frac{z}{Fr^2} + \frac{2}{3}k \quad (2.3)$$

$$\text{Re}_{eff} = \frac{U_0 L_0}{\nu + \nu_t} \quad (2.4)$$

where p is the static pressure, ρ is the fluid density, U_0 is the free-stream velocity, z is the non-dimensional depth below the surface (negative for points above the surface, in air), Fr is the Froude number of the flow, L_0 is a characteristic length (chosen to be the length of the blade, 63 m, for this dissertation), ν is the fluid kinematic viscosity, and k and ν_t are the turbulent kinetic energy and turbulent kinematic viscosity, respectively, both of which are produced by a turbulent model.

2.2.2 Turbulent Modeling

Turbulent modeling in all simulations in this dissertation is provided by Menter's blended $k-\omega/k-\epsilon$ two equation shear stress transport (SST) model (Menter, 1994). This model switches between the $k-\omega$ model in the inner boundary layer and the $k-\epsilon$ model in the outer boundary layer (and outside the boundary layer), taking advantage of the strengths of both models. The SST model is used in URANS simulations in chapter 4, where all turbulent scales were modeled and not directly solved for. Delayed detached eddy simulation (DDES) (Spalart et al., 2006) implemented into CFDShip and validated in (Xing et al., 2010a), is used for all simulations in chapters 5, 6, and 7 for its ability to predict unsteady separated flows, which are expected along the blades in the simulations herein. In regions where the turbulent length scale is sufficiently large relative to the local grid size DDES uses large eddy simulation (LES) to directly solve for large-scale turbulent viscosity and kinetic energy and uses URANS with turbulent modeling to calculate parameters of small-scale turbulent structures.

2.2.3 Numerical Methods

Pressure does not appear in the incompressible continuity equation, shown in equation (2.1), and a method for coupling the pressure and velocity fields is needed. Bernoulli's equation is valid only for steady-state, irrotational flows and is not valid for the simulations considered herein. Thus a Poisson equation for pressure is derived by taking the divergence of the momentum equation in (2.2), which develops a function for pressure of velocity and space

for enforcing the incompressibility constraint. A projection algorithm (Bell et al., 1991) is utilized to solve the pressure Poisson equation incorporating the PETSc toolbox (Balay et al., 2010), a library of publically available data routines and methods developed at Argonne National Laboratory.

The momentum convection terms in (2.2) are discretized using a second-order upwind-biased finite-difference scheme in simulations in chapters 3 and 4, and with a fourth-order hybrid upwind-biased scheme in chapters 5 and 6. This hybrid strategy switches to second-order accuracy for the momentum convection terms in regions very close to solid surfaces for stability. The unsteady temporal term in (2.2) is discretized with a second-order backward difference in all simulations.

2.3 Turbine Motion Prediction Module

CFDShip-Iowa v4.5 features a rigid-body 6-DOF motion solution module (Carrica et al., 2006) utilized in this dissertation to predict platform response to wind and wave excitation. Two coordinate frames are first defined: an inertial, fixed-earth frame and a turbine frame. The fixed-earth frame originates at the still water line (SWL) and is referred to with capital letters in this dissertation (X, Y, Z). The turbine frame (x_T, y_T, z_T) is fixed to the turbine and translates and rotates with the moving system. All platform motions and velocities presented in this dissertation are given in the fixed-earth system. These are defined as:

$$\begin{aligned}\mathbf{r} &= [r_x, r_y, r_z, \phi, \theta, \psi] \\ \mathbf{V} &= [U, V, W, \dot{\phi}, \dot{\theta}, \dot{\psi}]\end{aligned}\tag{2.5}$$

where r_x, r_y, r_z represent the linear translation of the turbine frame origin and ϕ, θ, ψ (pitch, roll, and yaw) represent the platform's orientation about X, Y, and Z, respectively. \mathbf{V} represents the time derivatives of the components of \mathbf{r} . The velocity vector with respect to the turbine frame, \mathbf{V}_T , is defined as

$$\mathbf{V}_T = [u, v, w, p, q, r]\tag{2.6}$$

where u , v , and w are the surge, sway, and heave linear velocities of the platform, respectively, and p , q , and r are the roll, pitch, and yaw angular velocities, respectively. The rigid-body equations of motion for the platform, defined in the turbine system, are:

$$\begin{aligned}
F_x &= m \left[\dot{u} - vr + wq - x_G (q^2 + r^2) + y_G (pq - \dot{r}) + z_G (pr + \dot{q}) \right] \\
F_y &= m \left[\dot{v} - wp + ur - y_G (r^2 + p^2) + z_G (qr - \dot{p}) + x_G (qp + \dot{r}) \right] \\
F_z &= m \left[\dot{w} - uq + vp - z_G (p^2 + q^2) + x_G (rp - \dot{q}) + y_G (rq + \dot{p}) \right] \\
M_x &= I_x \dot{p} + (I_z - I_y) qr + m \left[y_G (\dot{w} - uq + vp) - z_G (\dot{v} - wp + ur) \right] \\
M_y &= I_y \dot{q} + (I_x - I_z) rp + m \left[z_G (\dot{u} - vr + wq) - x_G (\dot{w} - uq + vp) \right] \\
M_z &= I_z \dot{r} + (I_y - I_x) pq + m \left[x_G (\dot{v} - wp + ur) - y_G (\dot{u} - vr + wq) \right]
\end{aligned} \tag{2.7}$$

Here F_i and M_i are the summed forces and moments, respectively, produced from integration of fluid forces over the solid surfaces of the turbine, gravitational forces, and mooring forces. In this dissertation the center of rotation, coincident with the origin of the turbine frame, \mathbf{r} , is *not* coincident with the turbine's center of gravity (CG), \mathbf{r}_{CG} , and is instead defined at the SWL for appropriate comparison to OC3 results. Thus the moments of inertia are translated, via the parallel-axis theorem, to the turbine's center of rotation:

$$\begin{aligned}
I_x &= I_{x_{CG}} + m (y_G^2 + z_G^2) \\
I_y &= I_{y_{CG}} + m (x_G^2 + z_G^2) \\
I_z &= I_{z_{CG}} + m (x_G^2 + y_G^2)
\end{aligned} \tag{2.8}$$

where m is the turbine's mass and x_G , y_G , and z_G are the perpendicular distances between the center of rotation and CG, all seen in equation (2.7) as well as (2.8). The linear equations of motion in (2.7) are solved to provide accelerations of each DOF. The velocities of each DOF are then calculated explicitly between time steps (a predictor stage) and corrected implicitly multiple times during each time step (corrector stages). This predictor-corrector method is discussed in detail in (Wilson et al., 2006).

2.4 Free-Surface Modeling

The free-surface is modeled with a level set method (Carrica et al., 2007b), where a scalar distance function, ϕ , positive in water, negative in air, and identically zero at the interface surface. The transport function of ϕ , as simply a scalar, is thus:

$$\frac{\partial \phi}{\partial t} + \mathbf{u} \cdot \nabla \phi = 0 \quad (2.9)$$

The distance function ϕ is reinitialized at each non-linear iteration (see section 2.6) to account for convection updates during correction steps. Dynamic free-surface boundary conditions are enforced by ensuring a zero velocity gradient normal to the surface and setting pressure at the free-surface to atmospheric:

$$\begin{aligned} \nabla \mathbf{u} \cdot \mathbf{n} &= 0 \\ p &= \frac{z}{Fr^2} \end{aligned} \quad (2.10)$$

The free-surface interface solution of all two-phase simulations in this dissertation is determined in a "semi-coupled" fashion, where equations (2.9) and (2.10) are subject only to the conditions of the denser phase (water). The lighter phase (air) solution is then constrained by the calculated free-surface, viewing it as a moving immersed boundary. More details on the free-surface model solution is available in (Carrica et al., 2007b).

Multiple oceanic wave models are available in CFDSHIP-IOWA. When using one of these models the wave surface is initialized throughout the simulation domain for the first time step and is maintained at the inlet boundary during subsequent steps, propagating into the simulation domain and subject to solution conditions. Two of the available wave models are utilized in this dissertation. Airy waves (Airy, 1849), regular waves based on a simple, single frequency sine wave, are used in chapters 3 and 4. The JONSWAP wave model (Hasselmann, 1973), an irregular wave model based on empirical data from the North Sea, is used in chapters 5 and 6 and is detailed in section 6.3.2.

2.5 Overset Grid Capabilities

CFDShip-Iowa utilizes overset grids (Carrica et al., 2007a) to solve across multiple grids moving relative to each other. Grids are laid out in a parent-child hierarchal relationship. All the grids of the entire turbine assembly comprise the parent object, while the hub grid and each blade grid are designated as children objects. The children objects translate and rotate with the parent, but are allowed motion relative to the parent. In this dissertation that relative motion is rotor rotation as well as, in chapter 6, blade-pitch (BP) rotation. Additional refinement grids, allowing for local, dynamic spatial resolution in regions of interest, such as the rotor wake of a wind turbine, can also be used. The overset code SUGGAR (Noack, 2005) runs parallel to the CFD code and provides run-time overset connectivity. The solver moves the grids based on 6-DOF platform and rotor motions and then reassembles them upon every time step. SUGGAR then determines which points to cut from the resultant composite grid and returns this information to the CFD solver.

2.6 Solution Strategy

The overall CFD solution strategy is shown in Figure 2. Note that during the first time step the solutions are produced with the turbine in the initial position (i.e. not moved) and SUGGAR is called during initialization for provision of overset information. The velocity and pressure fields are also initialized to constant values. A nonlinear iteration is begun and the solver moves into the hydrodynamic solution loop. The grids are first moved and cut based on the previous time step's predicted 6-DOF platform and rotor/blade motions. The turbulent parameters are solved based on the current velocities and the level-set equation is solved to determine the new location of the free-surface. The projection algorithm is then called to solve the coupled hydrodynamic velocity and pressure fields. Forces and moments are calculated via integration of pressure and skin-friction, developed from viscosity and velocity. The hydrodynamic residuals are then evaluated against user defined tolerances. If any residual is still above its tolerance then the 6-DOF motions are corrected based on updated velocities and the grids are moved and cut accordingly. This loop will continue for a user specified number of iterations or until all variables have dropped below tolerances, at which point the solver moves into the aerodynamic solution loop. The steps for the

aerodynamic loop are identical to those of the hydrodynamic loop with two exceptions: the free-surface, which is not subject to the air and wind conditions, is not reinitialized and the 6-DOF motions are not corrected based on updated aerodynamic forces and moments. After the aerodynamic loop has run through its maximum number of iterations, or has converged, the 6-DOF motions of the platform and rotor are explicitly predicted based on accelerations solved by the 6-DOF equations of motion in (2.7). The grids are moved and SUGGAR is called to cut. The solution time is incremented and a new time step begins. This process will continue until a user specified maximum number of time steps is reached or until manually ended. Designed for dynamic simulations, CFDSHIP-Iowa has no true steady-state convergence criteria, and the end of transience must be determined by the user.

2.7 Figures

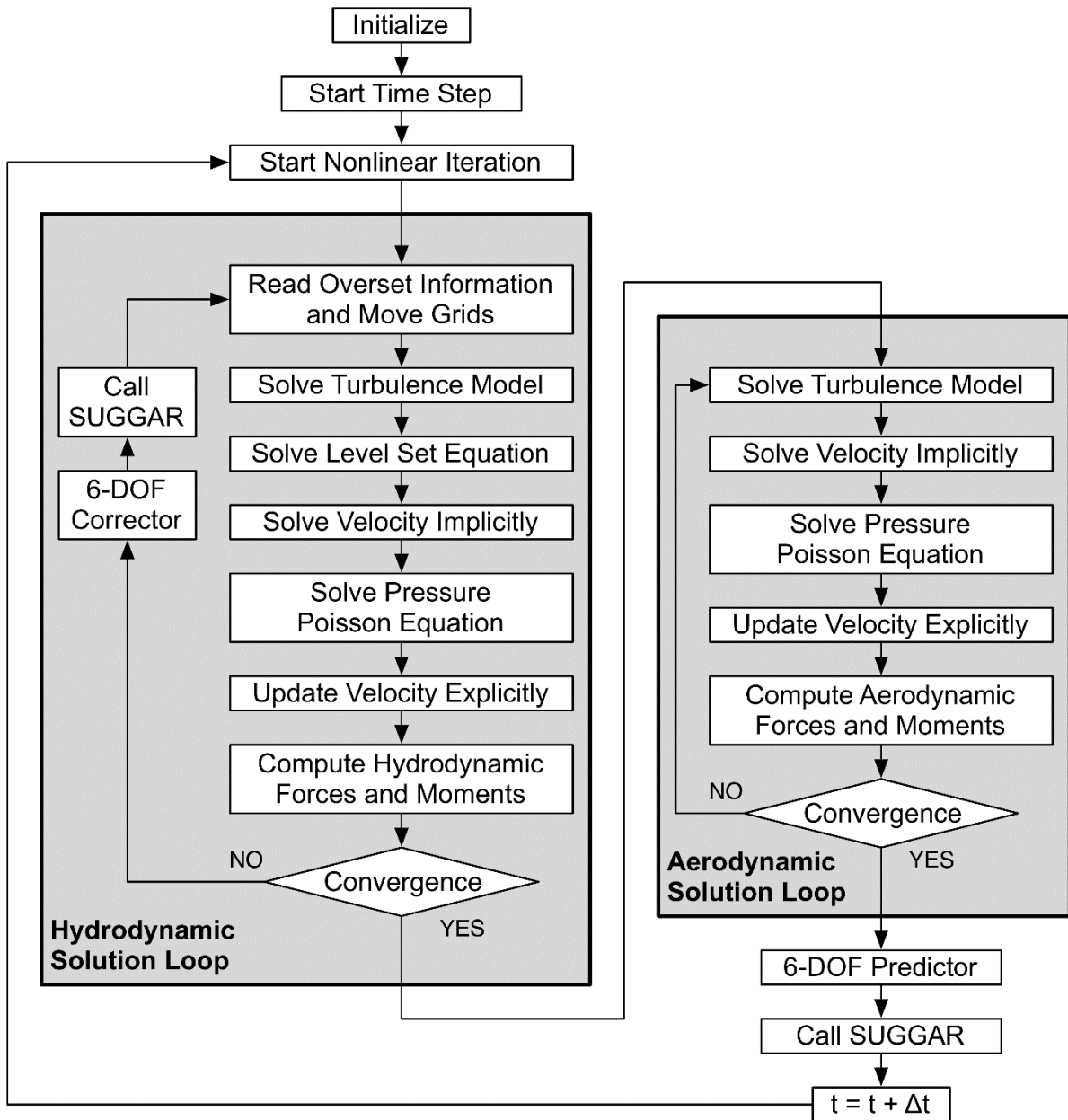


Figure 2 Base CFD solution strategy

CHAPTER 3: OC3-HYWIND DETAILS AND GRID SETS

3.1 Abstract

The key geometric and structural details of the OC3-Hywind, the turbine model utilized in all simulations in this dissertation, are presented. Each individual geometric component is described. The two grid sets used in this dissertation are then detailed.

3.2 OC3-Hywind Geometry

The OC3-Hywind is presented in Figure 3 with individual components colored uniquely. All geometry in this dissertation are modeled after the OC3-Hywind specifications in (Jonkman et al., 2009, Jonkman, 2010) except for the hub, where a more realistic geometry is used rather than the sphere dictated in (Jonkman et al., 2009). It is a 3-bladed horizontal axis FOWT with a 61.5 m blade length. Combined with a 3 m diameter hub this produces a 125 m rotor. The OC3-Hywind is shown in the initial, upright configuration in Figure 3, such that the platform and tower centerlines (CL) are coincident and vertical. The hub height is nominally located at 90 m above the SWL, which is 80 m above the junction of the platform and tower. The hub center is offset 5 m in the upstream direction to provide nacelle and tower clearance to the rotor. It is expected that the blades will deflect downstream during service, especially considering platform pitching motions. To provide a safe tower clearance a 5° tilt is given to the low-speed shaft (LSS) as well as a 2.5° blade pre-cone. Blade pre-cone is simply connecting the blade to the hub at an upstream angle, here seen in the aggregate 7.5° vertical blade clearance angle (red blade 1 in Figure 3). The platform draft from the static position is 120 m. The relevant geometric and structural details of the overall system, as well as each component, are summarized in Table 1.

The combined tower and platform geometry is shown in Figure 4. The platform joins the tower with a common 6.5 m diameter at 10 m above the SWL (seen in Figure 3). This 6.5 m diameter tapers linearly to the tower top to a final diameter of 3.87 m at a tower height of 77.6 m. The platform carries the 6.5 m diameter uniformly 14 m vertically downward (4 m below SWL) and then tapers linearly for 8 m to a final diameter of 9.4 m. The tower has a mass of 249,718 kg with its CG located 43.4 m above the SWL along its CL. The draft of

the platform is 120 m and its overall height is 130 m. The platform has a mass of 7,466,330 kg and its CG is located 99.92 m below the platform/tower junction.

The nacelle is modeled as a simple rectangular box with a streamwise length of 14.29 m, a width of 4.2 m and a height of 3.5 m. The nacelle is centered on the top of the tower in the transverse (Y) direction and the upstream (front) surface of the nacelle is located 3.095 m upstream of the CL of the tower. It has a large mass of 240,000 kg, accounting for the gearbox and generator masses, and its CG located 1.9 m downstream of the tower CL and centered in the vertical and transverse directions.

The hub geometry utilized is shown in Figure 6. Whereas the OC3 specifications dictated a 3 m diameter spherical hub in (Jonkman et al., 2009) a more realistic geometry was employed in this dissertation. This bullet-shaped hub has a 3.87 m diameter base, which tapers to a 2.85 m diameter. The hub is then capped with a hemisphere, clipped to provide a tangent angle to the tapered section of 8.05° . This clipped hemisphere adds an additional 1.36 m to the overall height of the hub, which is 5 m.

The complete blade geometry used, as per (Jonkman et al., 2009), is shown in Figure 7. The blade geometry is considerably more complex than the remaining components and only the relevant details are presented here. Multiple airfoil profiles are lined up along the pitch axis of the blade spaced with the dimensions shown in Figure 7. The DU designation on the inner profiles stands for Delft University while NACA stands for National Advisory Committee for Aeronautics. The blade is ‘twisted’ about the pitch axis—the inner profile of the blade is rotated 13.308° and the outer profile is at 0° pitch with a gradual decrease in between. This twist accounts for the different rotational velocity components seen by the inner sections and outer sections of the blade. The blade twist can be seen in Figure 8 where the individual profiles are shown along the pitch axis. The overall length of the blade is 61.5 m and the blade mass is 17,740 kg. The blade CG is located 20.475 m along the blade pitch axis. The blade is pre-coned, meaning its pitch axis is angled away from the tower to provide more clearance. The OC3-Hywind blades are pre-coned 2.5° , as seen in Figure 3 where the 7.5° angle between the rotor and the tower is a combination of the 5° LSS angle and 2.5° pre-cone angle.

3.3 Grid Design

Two grid sets, a “coarse” and a “fine” grid set, were utilized in this dissertation. Overlapping grid slices at the simulation domain mid-plane of the coarse and fine grid sets are shown in Figure 9 and Figure 10, respectively, showing the overall topology of each set. The coarse grid set was not developed during this dissertation and was provided pre-existing while the fine grid set was created herein.

For all solid surfaces considered a 2-dimensional surface grid is first fitted to the geometric surface and extruded normally outward to form 3-dimensional volume grids. This normal grid extrusion method allows for precise control of spacing immediately normal to solid surfaces— y^+ spacing (White, 2008)—which is critical for proper turbulent modeling. The maximum expected Reynolds number on the blades is determined using NREL's LC 5.3 maximum predicted rotor velocity with blade section chords for local length scales. The OC3 LC 5.3 features the maximum velocities of any considered by the OC3 and is chosen for conservative calculations (the simulations presented in this dissertation feature Reynolds numbers much lower than those of 5.3). The rotational velocity of the rotor is the most significant component of the local velocity at the maximum y^+ location and it is assumed that any variance in inflow conditions will scale equally along the entire blade, such that the location of the maximum y^+ spacing on the blade is constant. Thus the normal spacing of the first layer of points off solid-surface grids is assumed to keep the maximum y^+ spacing below 5 for the majority of grid points at all times.

The overall topology is similar between the sets, with large portions of points devoted to the aerodynamic solution at the rotor. The distribution of points in each of the coarse (5,473,564 total points) and fine (20,187,788 total points) grid sets are presented in Table 2 and Table 3, respectively. A description of each component grid is presented in the following sections.

The tower and platform geometries are combined for the purposes of grid development (simply referred to as the “tower” grid from here on). The coarse and fine tower grids are seen in Figure 11 left and right, respectively. In these images, as in the grid images to follow, the outer domain of the volume grids are shown in lighter gray and an interior slice is shown darker and in bold. The topology is changed considerably between the coarse and

fine tower grids. The coarse grid features a sharp-angled bowl at its top, accommodating a direct connection between the tower and nacelle surface grids. This feature was removed for the fine grid set, where overlapping regions were successfully cut from the tower and nacelle grids. The grid spacing of both grids is refined at the SWL for free-surface capture. The width difference between the two grids is visible in Figure 11. The overlapping region between grids must be sufficiently large for SUGGAR, and the grid spacing of the coarse grid set requires a much larger spatial domain. The refined spacings of the fine grid set allow for a considerably more slender tower grid, increasing refinement at the tower surface.

The coarse and fine nacelle grids are shown in Figure 12 left and right, respectively. An identical topology was used to form both nacelle volume grids. The fine nacelle grid provides slightly finer resolution in all 3-dimensions compared to the coarse nacelle grid. The overall resolution of the fine nacelle grid, however, is deliberately kept coarse to keep the total point count reasonable.

The coarse and fine hub grids are shown in Figure 13 left and right, respectively. Similar to the nacelle grids, the coarse and fine hub grids use an identical topology and size. The hub grid is expected to have little effect on the overall aerodynamic solution and, as such, the fine hub grid is given only slight increases in resolution.

The bulk of the points of the grids in this dissertation are located in the rotor to capture the highly unsteady aerodynamics surrounding the blades and wake. The coarse blade volume grid is split into two separate grids, the blade main and the blade tip grid, shown in Figure 14. The coarse blade main volume is relatively slender, with a diameter of ~ 4 blade chords for the majority of the length of the blade. This helps to keep points closer to the surface of the blade, but requires a larger refinement volume around the blade to prevent diffusion. This blade refinement grid is discussed in section 3.3.5. The blade tip grid closes the surface of the blade to a rounded tip which transitions smoothly between the blunt LE and the sharp TE. The tip grid is very small relative to the span of the blade (about 1.25%) and its primary function is to provide a stable solution at the tip considering its extreme topology and the shedding of tip vortices.

The overall grid strategy is varied for the fine grid, shown in Figure 15, where the blade root grid is separated from the blade main. Substantial increases in surface resolution (i- and k- directions, the span-wise and blade azimuth directions, respectively) are given to the fine blade grid as observed in comparing Table 2 and Table 3. This higher surface resolution helps capture the high pressure gradients expected on the blade and works to keep as much of the blade volume grids in the LES region of the DDES solution (see section 2.2.2) as possible considering computational and time constraints. The surface grid of the fine blade is coarser in the root grid than in the main grid as a considerably lower Reynolds number is expected at the blade root. Both the fine blade main and root volume grids have expanded spatially, extending over 5 blade chords of diameter at the root and growing slightly to accommodate a longer wake at the outer span of the blade. This grid was broadened to eliminate the need for a blade refinement grid and, as such, only a rotor refinement grid was used in the fine grid set.

The wake refinements used in the coarse and fine grid sets are shown in Figure 17 left and right, respectively. Both refinements are simple rectangular volume grids designed to capture vortical activity and large gradients in the rotor plane and wake. The wake refinement grid is fixed in the turbine coordinate system and translates and rotates with the platform. The coarse wake refinement grid extends about $1/6$ of a rotor diameter upstream, $1/2$ of a rotor diameter downstream, and a full $1-1/3$ rotor diameter in width to cover the entire rotor plane. However the wake refinement grid was not properly placed vertically and about $1/6$ of the bottom of the rotor plane was not captured by the refinement grid. The fine wake refinement grid is significantly resolved compared to the coarse refinement, with an average 250% increase in point count in each direction. The fine grid is extended to a full rotor diameter downstream and its width is extended to $1-1/2$ rotor diameters to ensure downstream capture of an expanding wake, while still reaching $1/6$ of a rotor diameter upstream. The spatial location error of the coarse grid is also corrected, with the fine wake refinement grid centered on the rotor plane.

The coarse grid set requires refinement around the blade region for spatial refinement as well as for stability with SUGGAR. These grids, the blade refinement grids listed in Table 2 and shown in Figure 16, are simple rectangular grids that encompass the entirety of the

blade grid. The blade refinement grids have two separate motions imposed upon them—they translate and rotate with the platform but also rotate with the rotor to maintain a fixed position relative to the blade they individually refine. The resolution of the overlap region between fine blade grids and fine wake refinement grid is made sufficient to eliminate the need for a blade refinement grid in the fine grid set.

Early tests with the fine grid set showed the need for a refinement grid at the bottom of the tower grid for stability during grid cutting. This refinement grid is named the “platform refinement” grid in Figure 10. This refinement grid also translates and rotates with the tower. It provides slight spatial resolution refinement at the bottom of the tower, but is designed almost exclusively to produce an intermediate overlap region, for SUGGAR, between the fine tower grid and background grids.

3.4 Figures

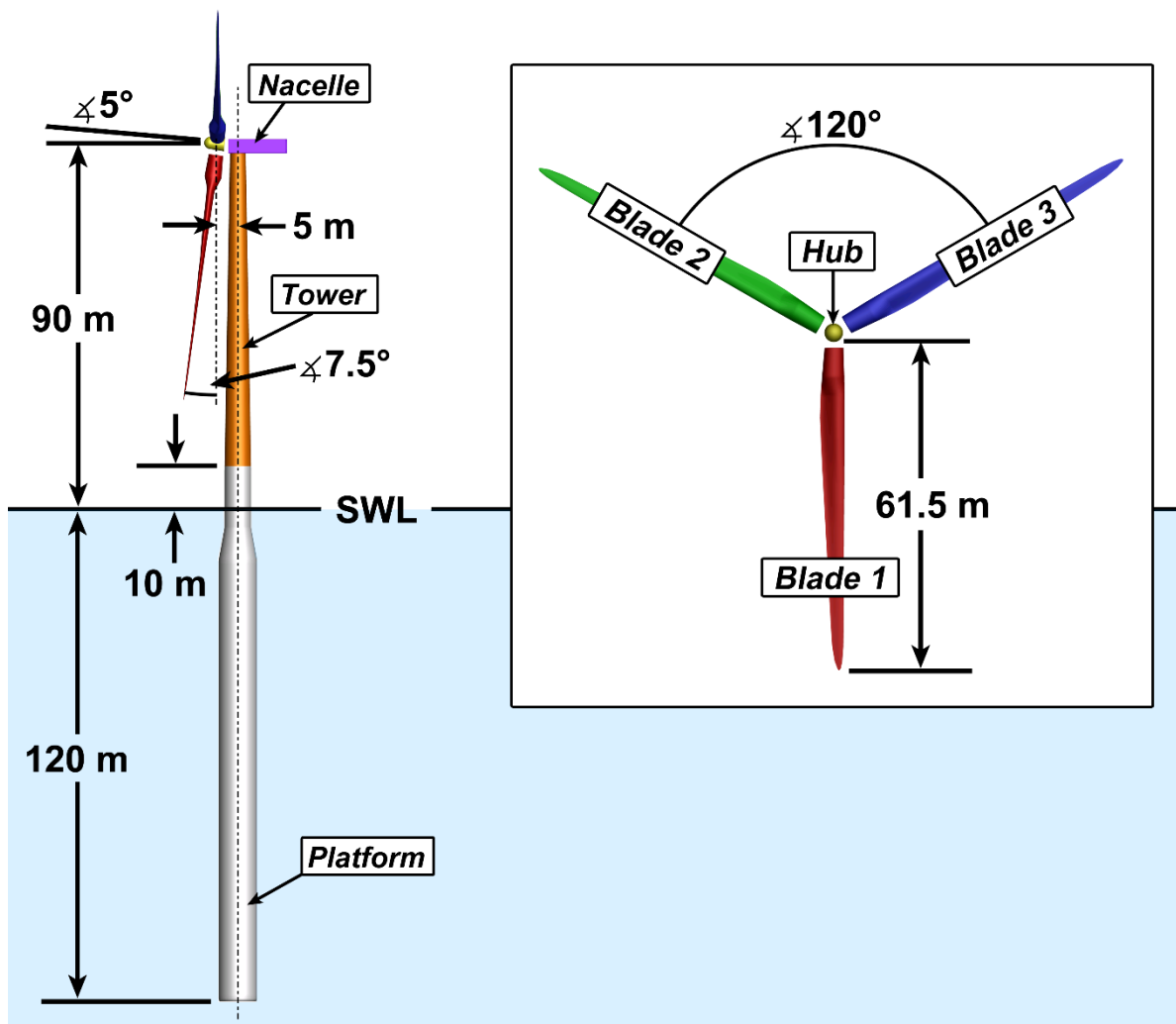


Figure 3 Overall OC3-Hywind geometric details

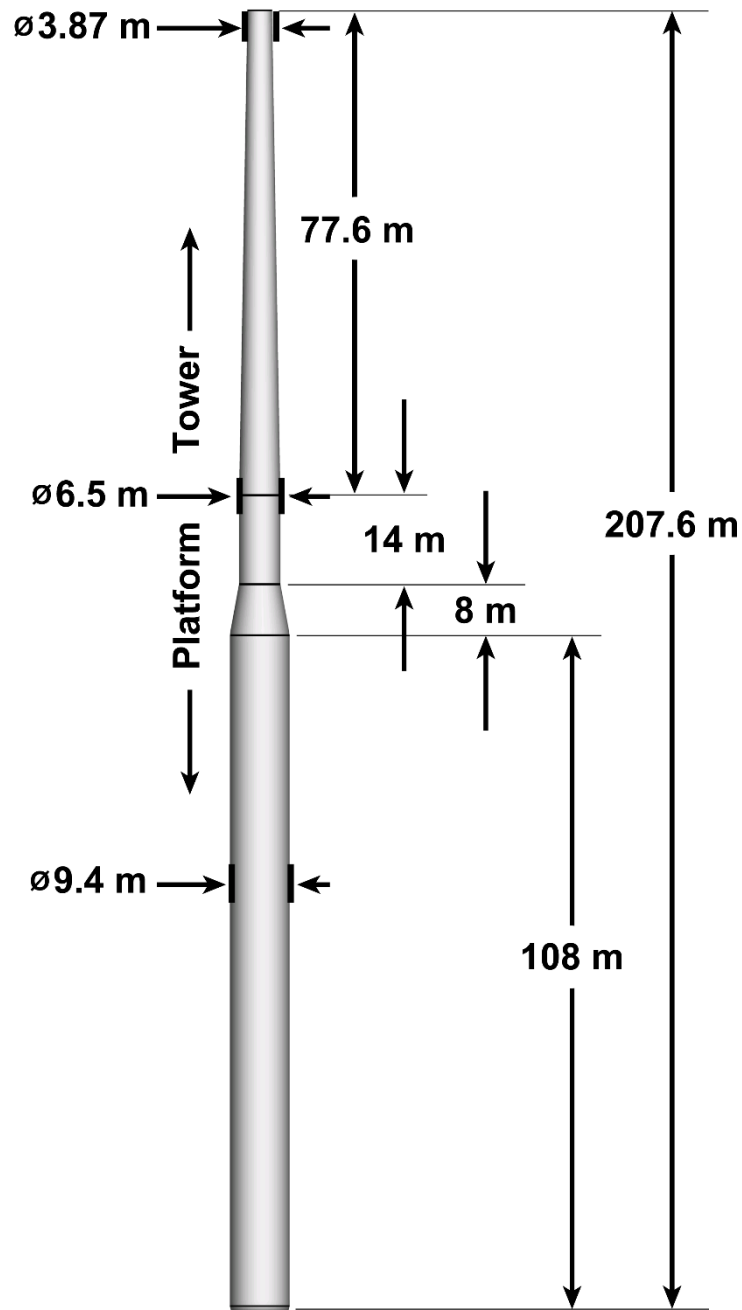


Figure 4 Combined tower and platform geometry

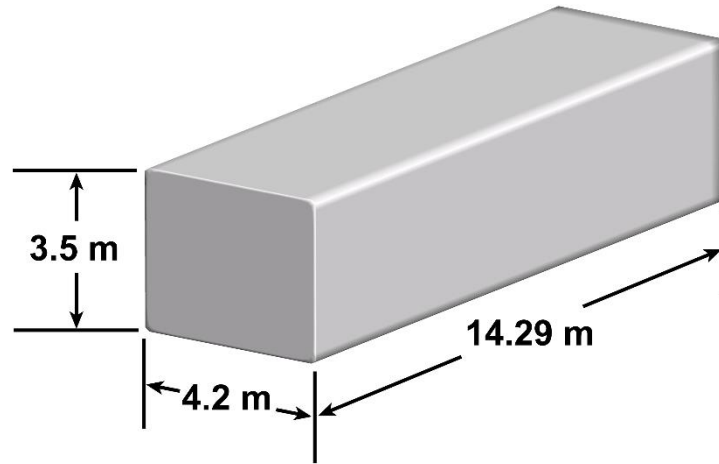


Figure 5 Nacelle geometry

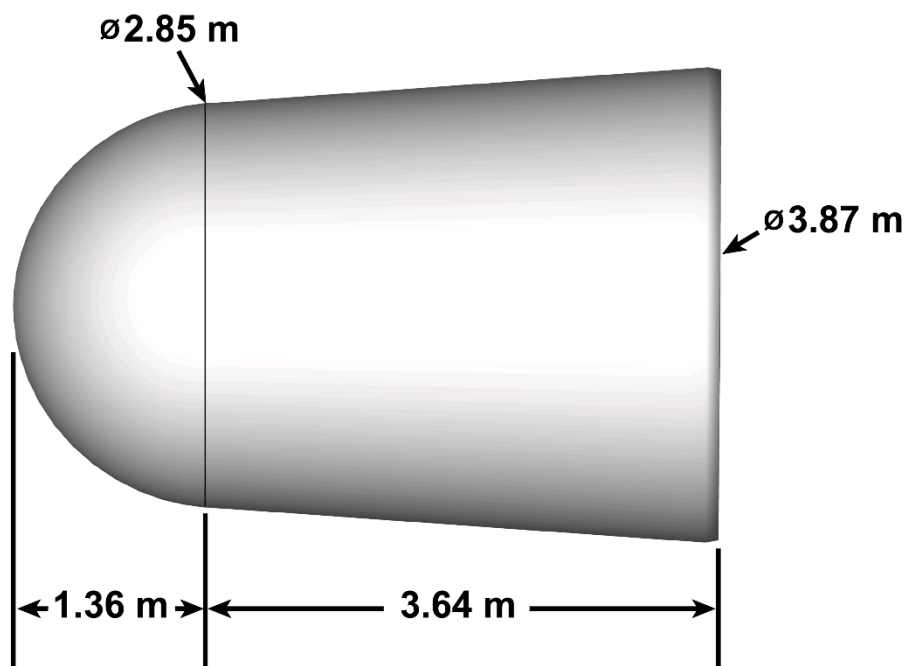


Figure 6 Hub geometry

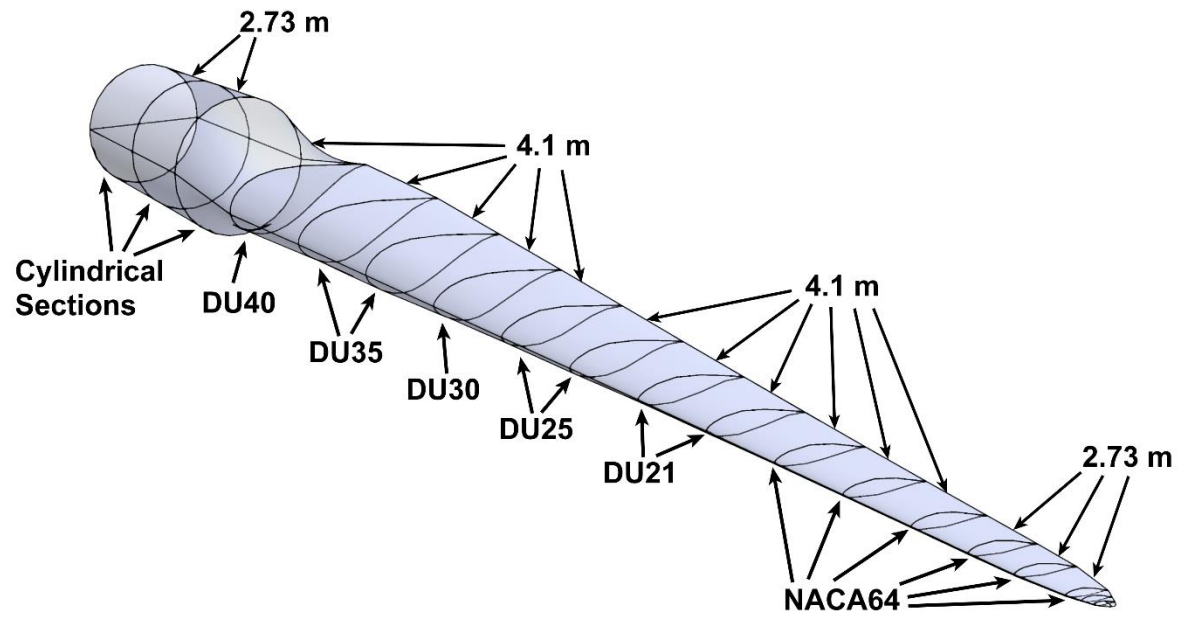


Figure 7 Blade geometry showing airfoil section profiles

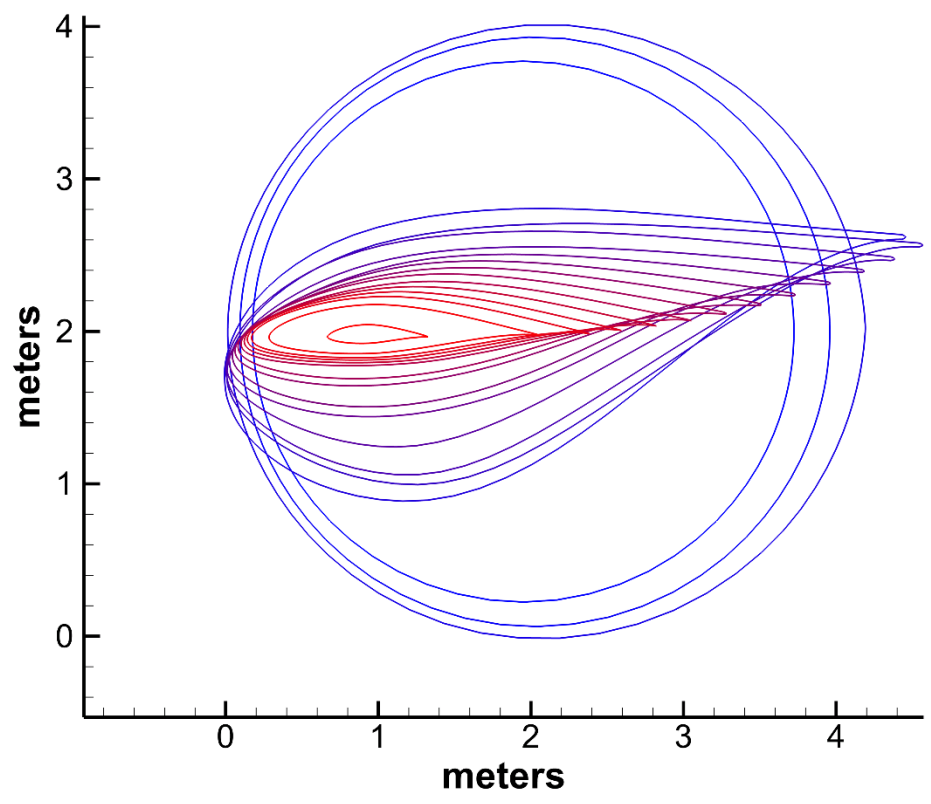


Figure 8 Airfoil profiles along length of blade from root (blue) to tip (red)

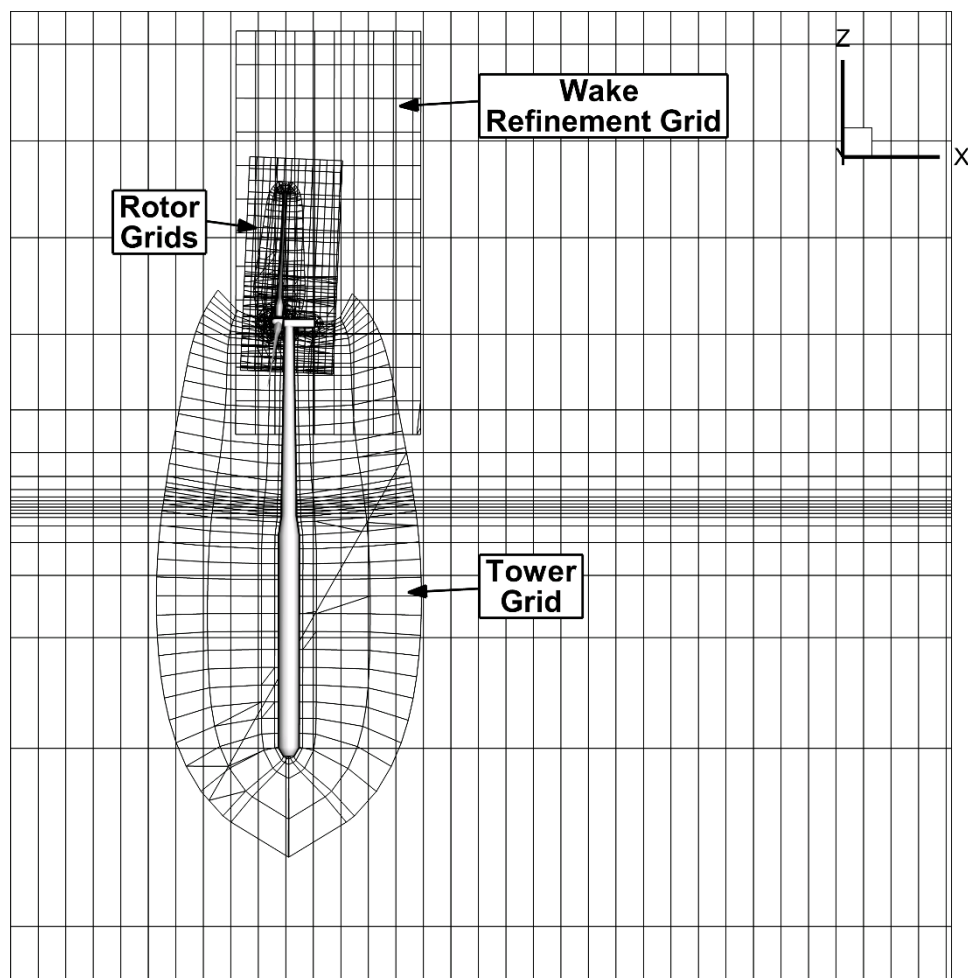


Figure 9 Coarse grid set mid-plane slice. 5 grid points skipped in all directions in all grids

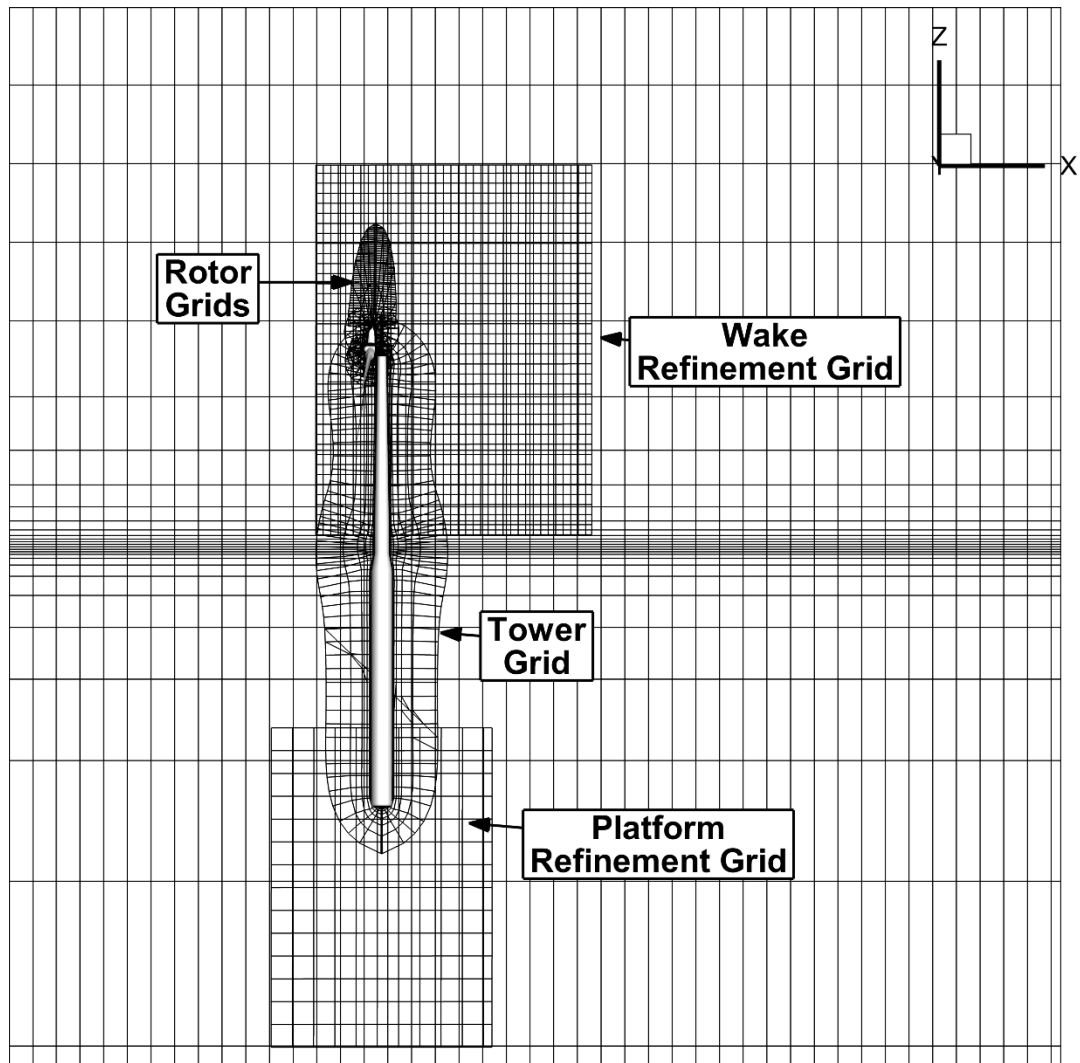


Figure 10 Fine grid set mid-plane slice. 5 grid points skipped in all directions in all grids

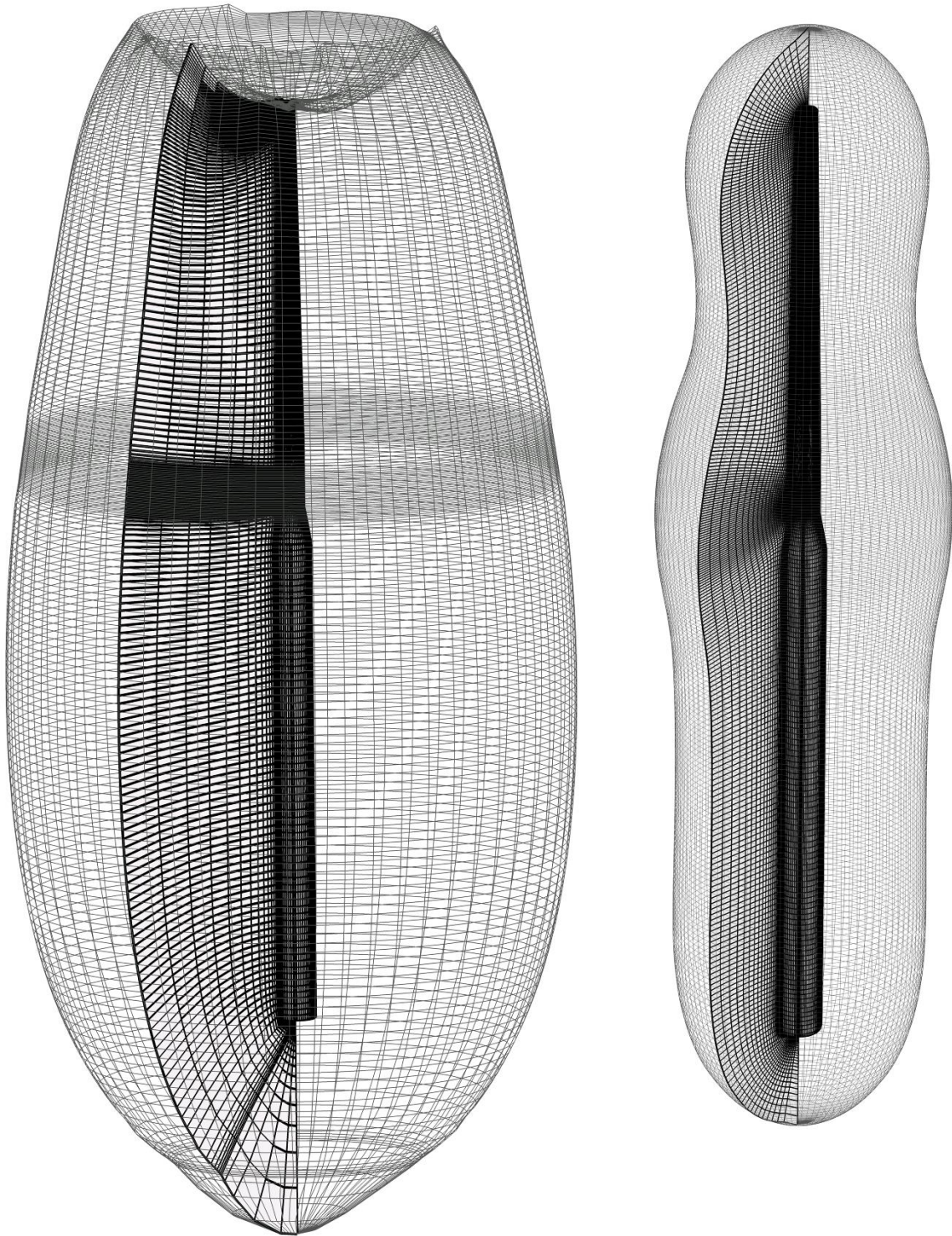


Figure 11 Combined tower and platform grids. (left) Coarse grid, (right) fine grid

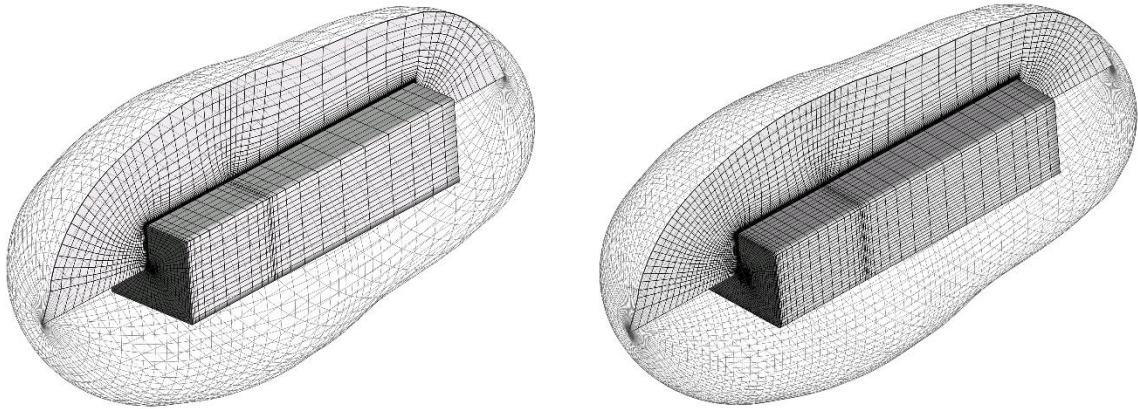


Figure 12 Nacelle grids. (left) Coarse grid, (right) fine grid

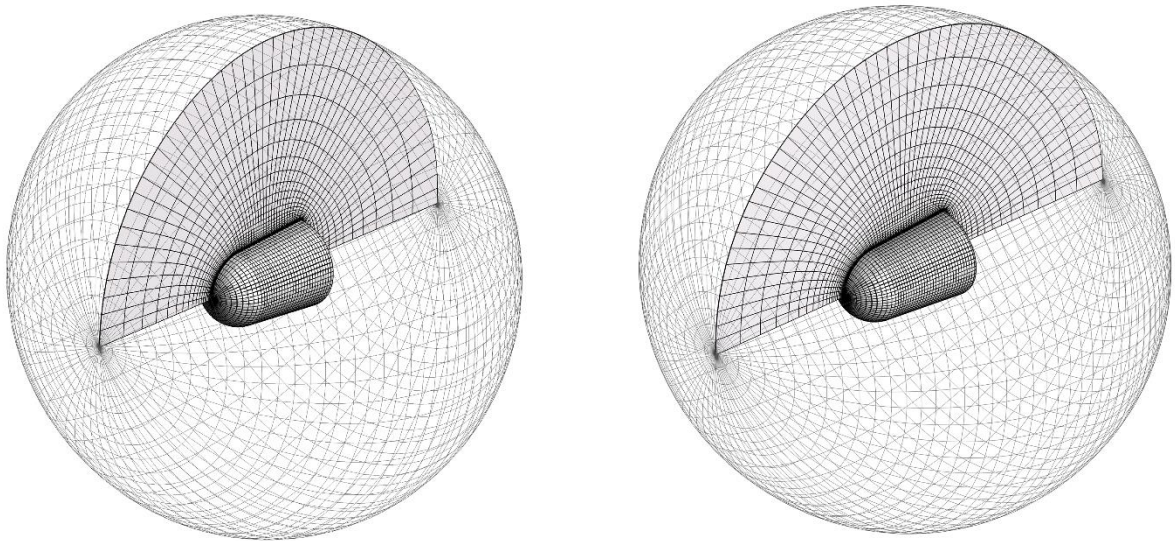


Figure 13 Hub grids. (left) Coarse grid, (right) fine grid

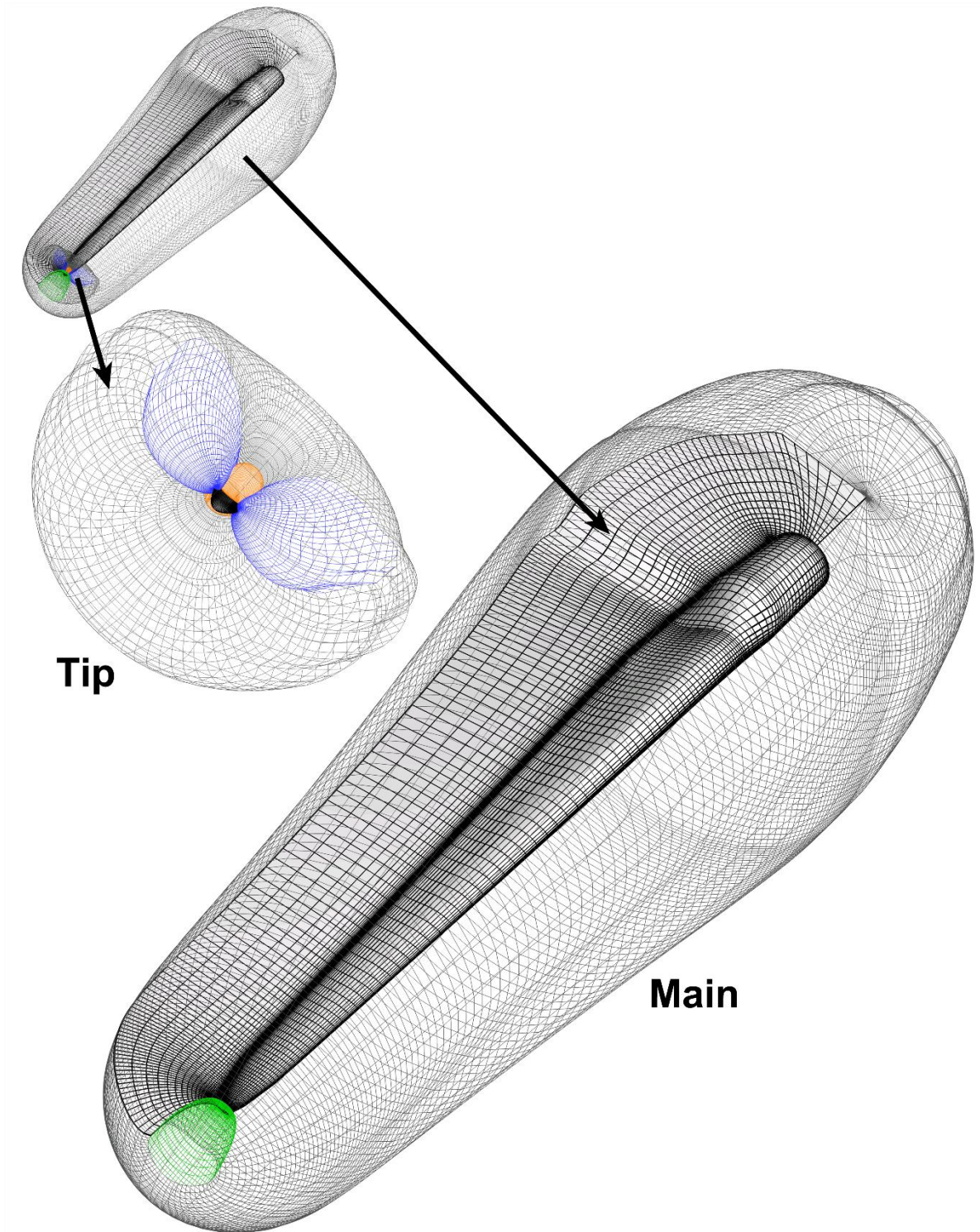


Figure 14 Composite coarse blade grid with sub-component grids

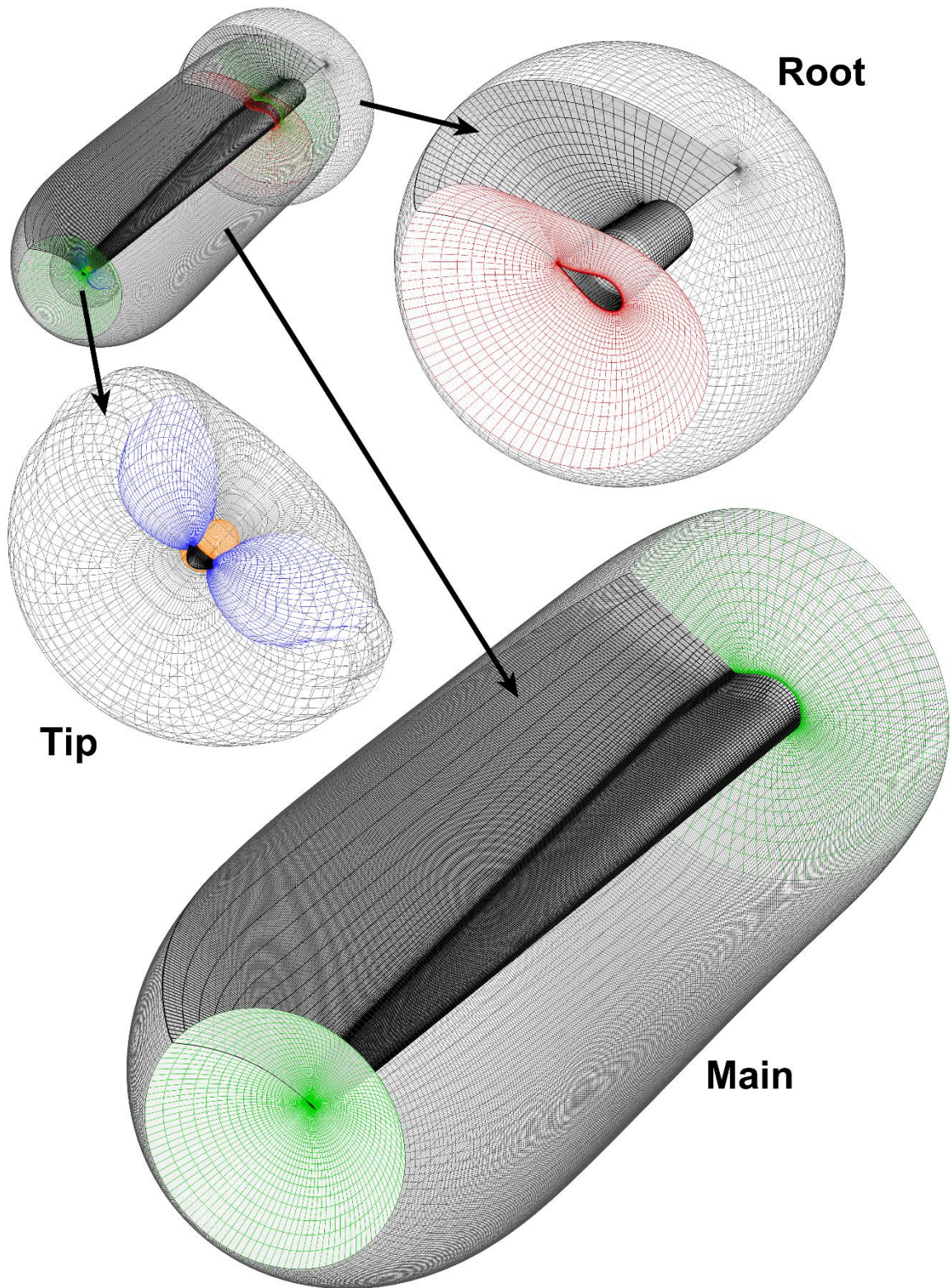


Figure 15 Composite fine blade grid with sub-component grids

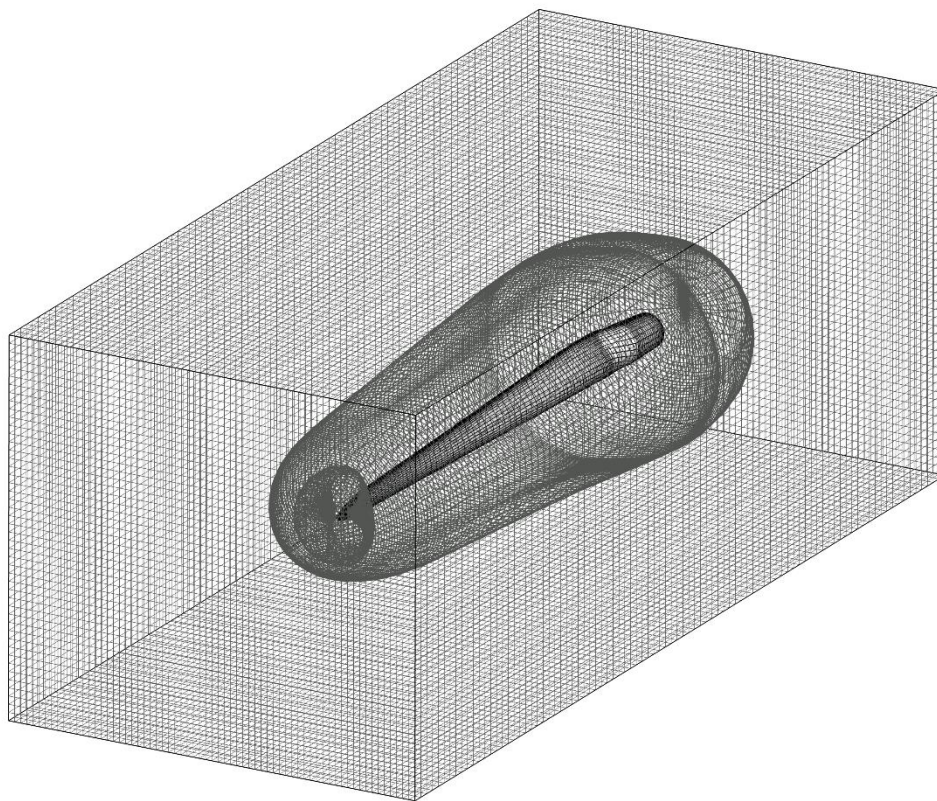


Figure 16 Coarse blade refinement grid with embedded coarse blade grid

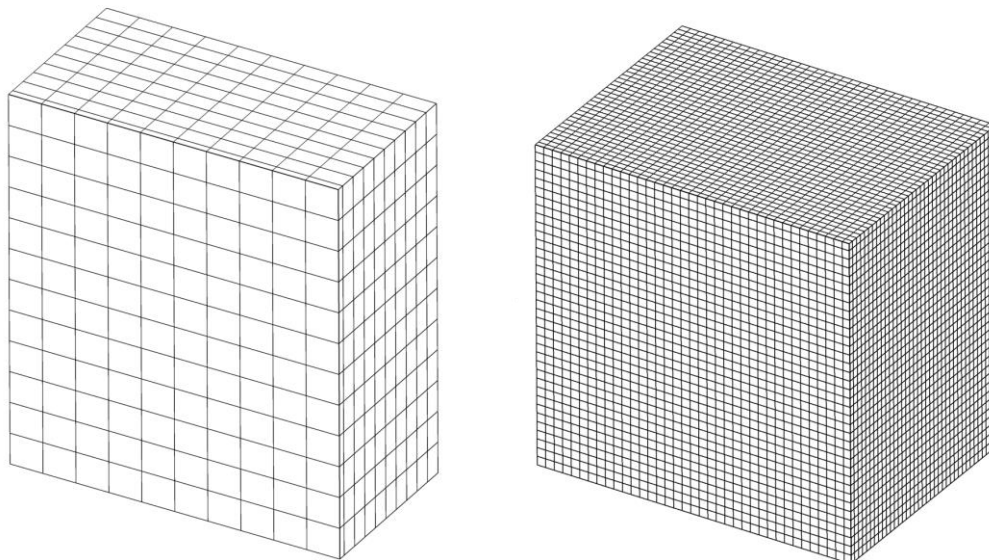


Figure 17 Wake refinement grids. 5 grid points skipped in all directions for clarity.
(left) coarse grid, (right) fine grid

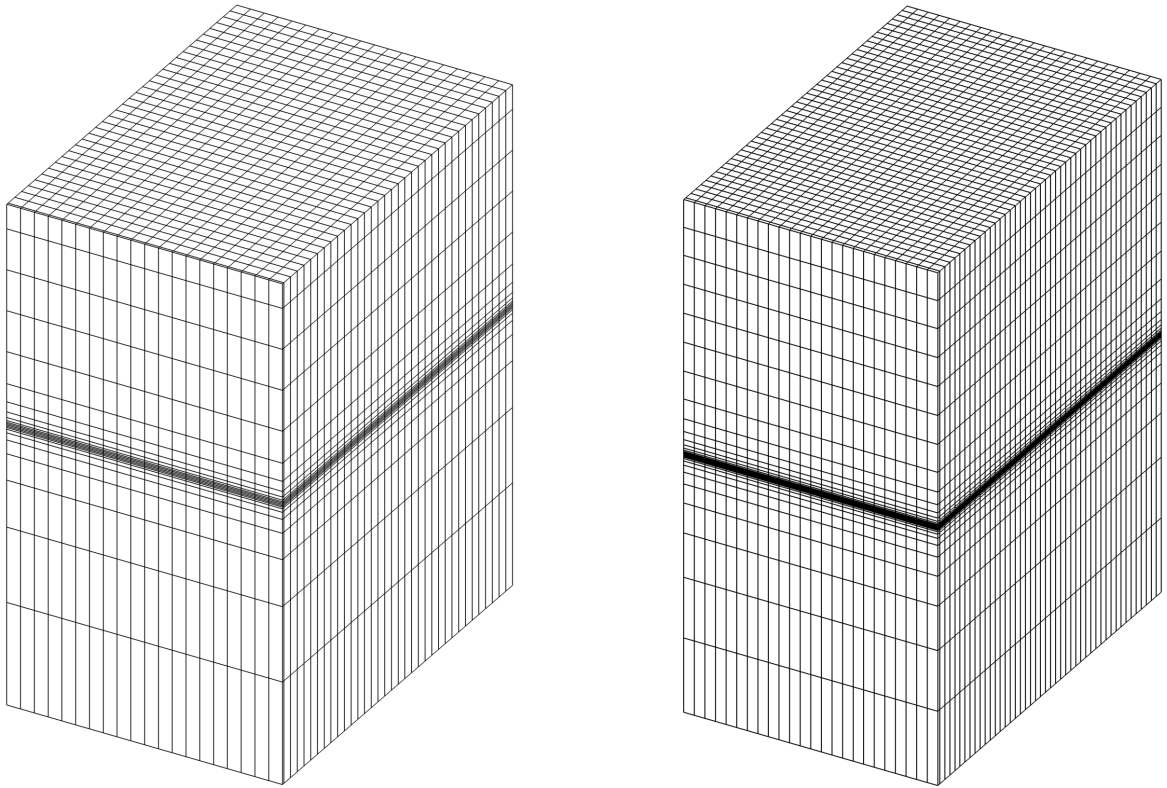


Figure 18 Background grids. 5 grid points skipped in all directions for clarity.
(left) coarse grid, (right) fine grid.

3.5 Tables

Table 1 Structural and geometric details

Gross Properties	Mass	8,066,000 kg
	CG Location (from initial)	(-0.018 m, 0, -78 m)
	Hub Height	90 m
	Draft	120 m
	LSS angle	5°
	Blade pre-cone	2.5°
	Rotor diameter	125 m
Tower	Height	77.6 m
	Mass	249,718 kg
	CG location	43.4 m above SWL along CL
	Bottom diameter	6.5 m
	Top diameter	3.87 m
Platform	Height	130 m
	Mass	7,466,330 kg
	Top diameter	6.5 m
	Bottom diameter	9.4 m
	CG location	99.92 m below platform top along CL
Nacelle	Length	14.29 m
	Width	4.2 m
	Height	3.5 m
	Front surface location	3.095 m upwind of tower CL
	Mass	240,000 kg
	CG location	Center of nacelle in transverse and vertical directions 1.9 m downstream of tower CL
Hub	Base diameter	3.87 m
	Top of taper diameter	2.85 m
	Height of hemisphere	1.36
	Mass	56,780 kg
	CG location	90 m vertically above SWL 5 m upstream of tower CL Centered in transverse direction
Blade	Length	61.5 m
	Average chord	3.42 m
	Inner profile twist	13.308°
	Blade pre-cone	2.5°
	Mass	17,740 kg
	CG location	20.475 m along blade pitch axis

Table 2. Coarse grid names and points with directions

Grid Name	i,j,k Points	Grid Dimension Direction	Total Points
Tower	i – 201	Along length of tower/platform (z_T)	609,024
	j – 48	Outward normal to tower surface	
	k – 61	Circumferential around tower/platform	
Nacelle	i – 51	Along streamwise length of nacelle	149,328
	j – 48	Outward normal to nacelle surface	
	k – 61	Circumferential around nacelle	
Rotor Hub	i – 51	Along length of hub	149,328
	j – 48	Outward normal to hub surface	
	k – 61	Circumferential around hub	
Blade Main (x3)	i – 151	Along length of blade ($-z_B$)	442,128
	j – 48	Outward normal to blade surface	
	k – 61	Circumferential around blade	
Blade Tip (x3)	i – 51	Along chord of blade tip	149,328
	j – 48	Outward normal to blade tip surface	
	k – 61	Lengthwise wrapped over blade tip	
Blade Refinement (x3)	i – 67	Perpendicular to blade chord	295,872
	j – 48	Along chord of blade	
	k – 92	Along length of blade	
Wake Refinement	i – 48	Fore-aft of tower/platform (x_T)	149,328
	j – 51	Horizontally transverse to flow (y_T)	
	k – 61	Along length of tower/platform (z_T)	
Background	i – 172	In streamwise direction (X)	1,754,572
	j – 101	Horizontally transverse to streamwise (Y)	
	k – 101	Vertically upward (Z)	
Total			5,473,564

Table 3. Fine grid names and points with directions

Grid Name	i,j,k Points	Grid Dimension Direction	Total Points
Tower	i – 271	Along length of tower/platform (z_T)	1,750,931
	j – 71	Outward normal to tower surface	
	k – 91	Circumferential around tower/platform	
Nacelle	i – 71	Along streamwise length of nacelle	394,121
	j – 61	Outward normal to nacelle surface	
	k – 91	Circumferential around nacelle	
Rotor Hub	i – 56	Along length of hub	198,856
	j – 53	Outward normal to hub surface	
	k – 67	Circumferential around hub	
Blade Main (x3)	i – 313	Along length of blade ($-z_B$)	2,122,140
	j – 60	Outward normal to blade surface	
	k – 113	Circumferential around blade	
Blade Root (x3)	i – 45	Along length of blade root ($-z_B$)	272,700
	j – 60	Outward normal to blade root surface	
	k – 101	Circumferential around blade root	
Blade Tip (x3)	i – 51	Along chord of blade tip	149,328
	j – 48	Outward normal to blade tip surface	
	k – 61	Lengthwise wrapped over blade tip	
Platform Refinement	i – 53	Fore-aft of tower/platform (x_T)	199,439
	j – 53	Horizontally transverse to flow (y_T)	
	k – 71	Along length of tower/platform (z_T)	
Wake Refinement	i – 185	Fore-aft of tower/platform (x_T)	6,331,625
	j – 185	Horizontally transverse to flow (y_T)	
	k – 185	Along length of tower/platform (z_T)	
Background	i – 223	In streamwise direction (X)	4,074,433
	j – 121	Horizontally transverse to streamwise (Y)	
	k – 151	Vertically upward (Z)	
Total			20,187,788

CHAPTER 4: DEVELOPMENT AND VALIDATION OF A QUASI-STATIC CROWFOOT MOORING-LINE MODEL[†]

4.1 Abstract

A general quasi-static crowfoot mooring model providing restoration forces is developed and tied into the CFD solver CFDSHIP-IOWA V4.5. The developed code is applied to the OC3-Hywind geometry in multiple CFD simulations. The crowfoot model is first validated against experimental data for free-decay tests. Following this a full system simulation with wave and wind excitation is performed utilizing the crowfoot model for securing the FOWT. The results predict less overall platform motions. Developed aerodynamic power is shown to rely heavily on system pitching and surging motions. The system simulation shows that the crowfoot model eliminates the need for a geometric line approximation and is ready to be utilized in future simulations

4.2 Introduction

The OC3-Hywind's mooring system consists of three crowfoot catenary lines shown in Figure 19b. This crowfoot connection increases the yaw stiffness of the overall mooring system (Nielsen et al., 2006). As a model for their Phase IV studies, the OC3 averaged the crowfoot line properties and removed the delta connection, producing only a single 2-point (anchor and fairlead) mooring structure. The OC3 also eliminated the crowfoot connection and instead added a constant yaw-spring stiffness to compensate (referred to as augmented yaw stiffness, or AYS in this chapter). Unfortunately the magnitude of this stiffness depends on the geometry and line properties and will also likely be different under various environmental conditions. The mooring system of FOWT platforms is important to the dynamic behavior of the FOWT and may also significantly affect the stability of the tower. Appropriate modeling of this system is critical during the overall system design (Matha et al., 2011, Brommundt et al., 2012). An excellent background on the analysis of mooring

[†]Development and results published in *CFD Simulation of a Floating Offshore Wind Turbine System Using a Quasi-Static Crowfoot Mooring-Line Model*
Journal of Ocean and Wind Energy (ISSN 2310-3604)
Copyright © by The International Society of Offshore and Polar Engineers
Vol 1, No.3, August 2014, pp. 143-152

systems for floating structures is presented in (Chakrabarti, 2005). To examine variations and potentially optimize a crowfoot mooring connection for the OC3-Hywind, as well as other slender spar-buoy designs, a more general model that considers the genuine crowfoot geometry and eliminates the need for an added yaw stiffness approximation is needed.

4.3 Mathematical Modeling and Methods

The OC3-Hywind is shown in Figure 19 in the initial position of the system with the coordinate systems used in this chapter. The earth-fixed system (X, Y, Z) originates at the still water line (SWL). The turbine frame (x_T, y_T, z_T), which translates and rotates with the moving system, originates at $[-.018 \text{ m}, 0, -78 \text{ m}]$ in earth frame coordinates with the z_T axis pointing upward along the centerline of the platform, the x_T axis pointing from front to back in the circular cross-section of the platform, and the y_T axis pointing to the left when the system is viewed from the front, forming a right-handed orthogonal frame. In the initial position the tower frame is identically oriented to the earth frame. The instantaneous position and orientation of the turbine frame in earth coordinates provide the surge, sway, and heave (X, Y, Z , respectively) of the system and its orientation is used to determine the roll, pitch, and yaw (rotation about x_T, y_T, z_T , respectively).

4.3.1 OC3-Hywind Mooring Models

The OC3-Hywind simulations were moored using three catenary lines offset at 120° . The 2-point OC3 AYS mooring lines attach to the platform at the fairlead connections shown in Figure 19a. The crowfoot mooring line fairlead connections are shown in Figure 19b. It is seen that the fairlead connections of the crowfoot lines are mirrored about the platform pitch axis relative to those of the AYS lines in order to keep the anchor placements consistent. However, an investigation of the effect of the fairlead relocation is left to future study.

Three mooring line models are tied into the CFD code for the purpose of securing the OC3-Hywind. The first is a base quasi-static 2-point single-line catenary model that solves for fairlead and anchor forces. The second is a single-line model that supplements the yaw-axis rotational stiffness of the turbine with the aforementioned yaw-spring stiffness utilized by participants of the OC3. The third is a crowfoot connection model, developed herein, that

iterates over a force balance between three separate catenary lines connected at a common position (see Figure 21) and then produces fairlead forces. In all three models viscous drag and dynamic effects of mooring line motion have been neglected and the effective mass of the lines is integrated into the calculated fairlead forces.

4.3.1.1 2-Point, Single-line, 2D Model

Jason Jonkman of NREL derived a 2-dimensional 2-point catenary mooring line model that solves for the effective horizontal and vertical components, H_F and V_F respectively, of the line tension at the fairlead (Jonkman, 2007). It is presented as a non-linear system of two equations in two unknowns, H_F and V_F , representing the horizontal (H_F) and vertical (V_F) forces at the fairlead in a local two-dimensional coordinate system. This model allows for three catenary configurations: a portion of the line sitting on the seabed, no portion of the line sitting on the seabed, and no seabed at all (or a ‘floating anchor’) as shown in Figure 20a, b, and c, respectively. The floating anchor solution is crucial for the crowfoot configuration as this allows a line to go slack. The model accounts for the weight of the line in fluid, elastic stretching, and seabed friction, while bending stiffness and structural dynamic effects are neglected. In the case where a portion of the mooring line sits on the seabed (neglecting frictional interaction between the line and the seabed) the system of two equations in two unknowns and the corresponding fairlead and anchor forces, from (Jonkman, 2007) are:

$$x_F = L_B + \frac{H_F}{\omega} \operatorname{asinh}\left(\frac{V_F}{H_F}\right) + \frac{H_F L}{EA} \quad (4.1)$$

$$z_F = \frac{H_F}{\omega} \left[\sqrt{1 + \left(\frac{V_F}{H_F}\right)^2} - \sqrt{1 + \left(\frac{V_F - \omega L}{H_F}\right)^2} \right] + \frac{V_F L - \frac{\omega L^2}{2}}{EA} \quad (4.2)$$

$$H_A = H_F \quad (4.3)$$

$$V_A = 0 \quad (4.4)$$

where x_F and z_F are the in-plane horizontal and vertical distances, respectively, between the anchor and fairlead (see Figure 20a), L_B is the length (unstretched) of line resting on the seabed, L is the total (unstretched) length of the line, ω is the apparent weight of the line in seawater per unit length, and EA is the extensional stiffness of the line.

For linking with the CFD code the earth-fixed frame anchor and fairlead positions are translated into a local coordinate frame as shown in Figure 20a. These translated positions, along with line properties, are input to the catenary solution module and the resulting fairlead forces are calculated. These forces are then translated to the moving tower coordinate frame, where the CFD code calculates the system's 6-DOF motions about its CG. This process is repeated for each simulation time step.

4.3.1.2 OC3 Added Yaw Stiffness Model

The AYS model is identical to the 2-point model except that the aforementioned supplemental yaw-stiffness utilized by the OC3 is added in. All force and moment calculations in CFDSHIP-Iowa are calculated in the moving tower coordinate system making this a simple linear addition to the yaw moment calculation:

$$M'_z = M_z + \psi \left(98,340,000 \frac{\text{Nm}}{\text{rad}} \right) \quad (4.5)$$

Here M_z is the moment about the z-axis in the local tower frame, ψ is the tower yaw in radians, and M'_z is the augmented moment. This process is also repeated for each simulation time step.

4.3.1.3 Crowfoot Model

The crowfoot model is composed of three catenary lines connected at a single junction point (Point J) shown in Figure 21. The anchor of line JA is the physical anchor of the individual crowfoot structure and its fairlead is defined as point, J. The other two lines of the crowfoot model, lines JB and JC, have their anchors defined as point J and their fairlead locations defined as B and C, respectively. Accurate prediction of the location of point J is crucial to the calculation of the fairlead forces at B and C as small displacements of this point can

result in large force differences at the fairleads. To calculate the position of J, all three lines are translated into their respective local coordinate frames. It is assumed that all lines have a positive Z_F (i.e. anchors never pass above fairleads):

$$x_{F_A} = \sqrt{(J_X - A_X)^2 + (J_Y - A_Y)^2} \quad (4.6)$$

$$z_{F_A} = J_Z - A_Z \quad (4.7)$$

$$x_{F_B} = \sqrt{(B_X - J_X)^2 + (B_Y - J_Y)^2} \quad (4.8)$$

$$z_{F_B} = B_Z - J_Z \quad (4.9)$$

$$x_{F_C} = \sqrt{(C_X - J_X)^2 + (C_Y - J_Y)^2} \quad (4.10)$$

$$z_{F_C} = C_Z - J_Z \quad (4.11)$$

where $J_{x,y,z}$ is the location of J in the earth-fixed frame (similar for the anchor point, A, and fairleads B and C). Forces are then calculated in the lines' local coordinate frames using the catenary solutions module (see Force Solution Block in Figure 23). For line JA the coefficient of seabed friction can be set to any positive value for the case of modeled static friction between the line and the seabed or seabed friction may be neglected altogether. Lines JB and JC, however, have no seabed at all. Here comes in the importance of the aforementioned 'floating anchor' scenario. Modeling lines JB and JC as having no seabed, yet a fixed anchor point, allows one of lines JB or JC to go to a slackened position and the other to assume the bulk of the line tension, effectively shifting the yaw-angle correcting moment arm to the side that requires it. This shifting of the moment arm from B to C, or vice-versa, is the main strength of the crowfoot connection concept. These forces are then summed in a three-dimensional force balance at point J. The vertical forces translate directly, but the horizontal forces must be split into X and Y components. The mooring lines are represented by geometrically linear bodies in the XY plane such that the angle each of the three individual crowfoot component lines form with the X-axis can be calculated by their respective endpoints. See Figure 22 for a description of these angles. Eqs. (4.12) and (4.13) produce the cosine and sine of α (similar for β and γ):

$$\cos \alpha = \frac{J_X - A_X}{\sqrt{(J_X - A_X)^2 + (J_Y - A_Y)^2}} \quad (4.12)$$

$$\sin \alpha = \frac{J_Y - A_Y}{\sqrt{(J_X - A_X)^2 + (J_Y - A_Y)^2}} \quad (4.13)$$

Through the use of these angles the lines' horizontal forces are separated into X and Y components in the earth-fixed frame. The force balance system of equations in fixed X, Y, and Z components is setup at point J. The locations of A, B, and C are fixed at any individual time step, such that the force balance becomes a system of 3 equations in 3 unknowns:

$$f_1(J_X, J_Y, J_Z) = H_{F_A} \cos \alpha + H_{A_B} \cos \beta + H_{A_C} \cos \gamma \quad (4.14)$$

$$f_2(J_X, J_Y, J_Z) = H_{F_A} \sin \alpha + H_{A_B} \sin \beta + H_{A_C} \sin \gamma \quad (4.15)$$

$$f_3(J_X, J_Y, J_Z) = -V_{F_A} + V_{A_B} + V_{A_C} \quad (4.16)$$

where f_1 , f_2 , and f_3 are the net-forces in the X, Y, and Z dimensions, respectively. Eqs. (4.14), (4.15), and (4.16) are iterated to solve for the final position of point J using Broyden's method (Broyden, 1965) outlined in Figure 23. The resultant fairlead forces are transferred back to the CFD code for 6-DOF motion calculations (see Figure 24).

Broyden's method works by directly solving the Jacobian matrix of a system of equations. This direct solution of the Jacobian eliminates the need to take analytical derivatives of Eqs. (4.14), (4.15), and (4.16). The initial Jacobian matrix, $\mathbf{\Omega}_0$, is only an estimate of the final one. Therefore a finite-difference scheme will provide sufficiently accurate results. The Jacobian matrix is defined as

$$\mathbf{\Omega}_{j,i}^n = \left(\frac{\partial f_j^n}{\partial J_i^n} \right) = \begin{bmatrix} \frac{\partial f_1^n}{\partial J_X^n} & \frac{\partial f_1^n}{\partial J_Y^n} & \frac{\partial f_1^n}{\partial J_Z^n} \\ \frac{\partial f_2^n}{\partial J_X^n} & \frac{\partial f_2^n}{\partial J_Y^n} & \frac{\partial f_2^n}{\partial J_Z^n} \\ \frac{\partial f_3^n}{\partial J_X^n} & \frac{\partial f_3^n}{\partial J_Y^n} & \frac{\partial f_3^n}{\partial J_Z^n} \end{bmatrix} \quad (4.17)$$

Each differential term is differenced using a first-order forward scheme using $\Delta J_i = 0.0001$ m, chosen for its numeric stability given the desired tolerance of the force balance at point J and computational cost:

$$\frac{\partial f_j}{\partial J_i} = \frac{f_{j+\Delta J_i} - f_j}{\Delta J_i} \quad (4.18)$$

The earth-system coordinates of point \mathbf{J}^n are first assumed using its position at the previous time step, \mathbf{J}^{t-1} . Here n represents the crowfoot solution iteration index and t represents the time step. For the first time step \mathbf{J}^n is assumed to be the location $R\%$ along a single line, where R is defined as the ratio of the lengths of lines JB and the total of JB and JA. Eqs. (4.14), (4.15), and (4.16) are repeatedly evaluated by using \mathbf{J}^n and the ΔJ coordinates as per Eq. (4.18) to assemble the initial Jacobian. The iterative loop begins after the calculation of the initial Jacobian matrix. Eqs. (4.14), (4.15), and (4.16) are evaluated to determine the X,Y,Z-component values of the force balance at point \mathbf{J}^n . This vector of net-force values, $\mathbf{f}(\mathbf{J}^n)$, is then used to calculate a correction vector, $\delta\mathbf{J}^n$:

$$\delta\mathbf{J}^n = -(\mathbf{\Omega}^n)^{-1} \mathbf{f}(\mathbf{J}^n) \quad (4.19)$$

Eq. (4.19) requires taking the inverse of the Jacobian matrix. The formulae for inverting a 3x3 matrix are readily available and are not included for brevity. The correction vector is then summed with the current point \mathbf{J}^n to produce an updated junction point position, \mathbf{J}^{n+1} :

$$\mathbf{J}^{n+1} = \mathbf{J}^n + \delta\mathbf{J}^n \quad (4.20)$$

Eqs. (4.14), (4.15), and (4.16) are again evaluated using the newly calculated \mathbf{J}^{n+1} coordinates to produce an updated net-force vector, $\mathbf{f}(\mathbf{J}^{n+1})$. This new net-force vector is then used to check for convergence. Multiple useable convergence criteria exist for this scenario but as, ultimately, the desired result of the net-force vector is $\mathbf{f}(\mathbf{J}) = \mathbf{0}$, the maximum absolute value of $\mathbf{f}(\mathbf{J}^{n+1})$ is checked against a predefined input tolerance:

$$\mathbf{IF} \left(\max |\mathbf{f}(\mathbf{J}^{n+1})| < \text{tolerance} \right) \quad (4.21)$$

If Eq. 25 returns false then the solution has not converged within tolerance and requires more iterations. The coordinates of point J and the Jacobian matrix are updated as:

$$\begin{aligned}\mathbf{J}^n &= \mathbf{J}^{n+1} \\ \boldsymbol{\Omega}^n &= \boldsymbol{\Omega}^{n+1}\end{aligned}\tag{4.22}$$

and the process is repeated. If Eq. (4.21) returns true, then the solution has converged, and the values calculated as \mathbf{J}^{n+1} are returned to CFDShip-Iowa as the determined position of point \mathbf{J}' .

4.3.2 Numerical Methods and Solution Strategy

In all simulation in this chapter both the momentum and level-set convection terms are discretized with a second-order upwind finite-difference scheme. The unsteady term of the momentum equation is discretized with a second-order backward difference scheme. The overall solution strategy, including the newly developed crowfoot mooring line module, is shown in Figure 24.

4.4 Simulation Conditions and Design

Using the OC3 specifications from (Jonkman, 2010) the seabed depth is set to 320 m and the mooring fairleads are located 70 m below the SWL giving an initial, static z_F of 250 m. The anchors are placed 853.87 m radially from the tower's vertical z-axis. This combined with a 5.2 m fairlead radius (the fairlead connections protrude 0.5 m beyond the platform surface) gives an initial x_F of 848.67 m. The crowfoot model splits the single line and connects to three common fairleads offset 60° from the radial line from the tower axis to the anchor as shown in Figure 19b. Specific geometry of the original crowfoot lines was unattainable. However, based on private email conversations with an industry expert from Statoil of Norway, the lengths of lines JB and JC for each crowfoot structure were estimated to be 10% of the length of the 2-point lines developed in (Jonkman, 2010), 90.22 m. The catenary solution routine requires the line weight in water, the unstretched length of the line, and the extensional stiffness of the line. Details about line properties used for each model tested are shown in Table 4.

CFDShip-Iowa features a static initialization mode that computes the mass and static wetted area of the tower based on initial grid placement and external forces. Both the AYS and crowfoot models are assumed to have the same initial position and experience, therefore, the

same buoyant force. However the two mooring line models, viewed by the FOWT as external forces, do not produce the same initial fairlead forces. The crowfoot lines have approximately 90 m more line per mooring structure than the AYS lines and yet initialize at the same location, increasing the line weight and, thus, the vertical force experienced at the fairlead. This added line weight is absorbed into the weight of the tower, such that the mass of the crowfoot tower is slightly less than that of the AYS tower, as shown in Table 4. Both model masses closely match the OC3's mass of 8.066E6 kg.

Cases 1.4, and 5.1, of the OC3's phase IV are simulated. Case 1.4 consists of six free-decay time-series tests where each of the six rigid-body DOFs are individually perturbed and the system allowed to decay to a static position. Case 5.1 introduces excitation from regular Airy waves and a steady wind. The rotor rotation is fixed at 9.4 RPM, which is the average rotor speed calculated by the NREL in their OC3 results. See Table 5 for a summary of cases. The coarse grid set, discussed in chapter 3, is utilized in all simulations in this chapter.

4.5 Results and Discussion

The results of the cases detailed in Table 5 are presented. The results of case 1.4 are compared to experimental data provided to the NREL by Statoil of Norway (Jonkman et al., 2010). Case 5.1 results are presented against NREL's OC3 results using FAST.

4.5.1 Case 1.4 Tests

Six individual DOF decay tests are performed using both the AYS and crowfoot lines. The tower is perturbed a prescribed amounts (as per Jonkman, 2010) along the DOF of interest and then released to move freely from that position. The results of four of the six simulations from cases 1.4b and 1.4c are presented in Figure 25 along with experimental results from Phase IV of the OC3 (Jonkman et al., 2010). The decay tests show good amplitude agreement with those of the experimental results and, important to the validity of the proposed crowfoot model, amplitude agreement with each other. The crowfoot model (0.00939 Hz) shows a 16.7% increase, and the AYS model (0.00866 Hz) shows a 7.6% increase, in surge natural frequency when compared to the experimental results (0.00805 Hz). One source of this difference is numerical error derived from the spatial and temporal

discretization utilized in the present study. Modeling error is also present in both models, as both are assumed to be solid wire lines with no dynamic effects. The neglected dynamic effects of the lines will be most pronounced in surge. The AYS model is a geometric approximation of the experimental lines and the crowfoot model in the present study utilizes the line properties used by the OC3, as the specifications of the experimental lines were not made available. This suggests that the surge restoration forces provided by the two models might not match those of the experimental lines. The crowfoot model shows a 10% higher frequency in surge free-decay than the AYS. This frequency difference is likely due to the increased surge restoration forces provided by the crowfoot model (see Figure 26). Both models show strong amplitude and frequency agreement with the experimental results in both heave and pitch tests. The crowfoot model shows a slight (-1.6%) difference in frequency (0.119 Hz) compared to the experimental data (0.121 Hz) in yaw as well as a 5% decrease in amplitude, while the AYS model agrees well in both amplitude and frequency. Tower mass differences between the two models and the difference in yaw restoration between them account for these differences. Both models agree well with the experimental results.

4.5.2 Case 5.1 Tests

Case 5.1 introduces regular sea wave motions and steady wind excitation. The tower is initialized at its static position and wind and waves are introduced with parameters shown in Table 5. The time series results of the platform surge, heave, pitch, and yaw in case 5.1 are shown in Figure 28 along with the NREL-FAST results. The transient start-up period has been removed from the results and two 10s wave periods are shown. The plots have been arranged such that the wave height at the platform centerline is at a maximum at 0 s. In case 5.1 the present CFD results predict a mean surge of 12.87 m downstream, which is 5.5% less than the 13.62 m predicted by NREL-FAST. Dynamic range of the platform surge (2.23 m) is 75% of that predicted by NREL-FAST. This difference in surge is likely due to NREL-FAST's usage of a constant drag coefficient in Morison's equation. This doesn't account for the increase in drag at lower Reynolds numbers nor any turbulent behavior associated with oscillation. The current predictions show a -0.16 m mean heave, 26% closer to the SWL, as well as a slight phase lag when compared to the NREL-FAST results. The augmented

viscous-drag term from Morison's equation only considers flow perpendicular to the central axis of the platform and does not account for skin friction in heave. The present CFD results completely resolve the viscous boundary layer at the platform surface and hydrodynamic (not just buoyant) heave forces are solved for. The captured viscous effects in heave, as well as different mooring restoration characteristics between models, are likely the reasons for both the phase and mean differences. A mean pitch of 2.83° is calculated in the current study, which agrees well with the NREL-FAST results. A 25% decrease in pitch dynamic range is predicted, likely due to drag forces experienced by the tower, hub, and nacelle—forces which are neglected in the NREL's results. The current results predict the same mean yaw (-0.029°) but 62.3% less overall yaw than that of the NREL-FAST results, although both predict well less than 1° of dynamic range. This is due to the crowfoot model providing more yaw restoration at very low yaw than NREL's single-line AYS model, although this is difficult to discern in Figure 26. In pure yaw the crowfoot model provides more yaw restoration at yaw angles less than $\pm 1.37^\circ$. Figure 27 shows a comparison of restoration forces and moments between the AYS and crowfoot configurations utilized by NREL and this dissertation, respectively, in 4 single-DOF displacements. The crowfoot model is observed to provide greater restoration for both platform surge and pitch displacements in the intervals of interest. The AYS and crowfoot models agree very well for platform yaw displacements of less than $\pm 2^\circ$, well within the expected range of the simulations herein. Vertical forces due to heave displacements are linear in the range shown as additional line weight is being lifted off or placed onto the seabed. The constant shift between the two models is due to the additional weight of the delta connection of the crowfoot, which uses ~10% additional line per mooring structure.

The aerodynamic power and thrust time-histories for load case 5.1 of the present study are shown in Figure 30 along with the generator power generation predictions of the NREL-FAST. In the current study the power is calculated via integrating both pressure and friction effects over the surface of the blade and multiplying by the constant angular velocity. The CFD results using the crowfoot model predicts 1.76 MW in mean power delivered to the shaft. Also included in Figure 30 is the surge velocity of the current study. This curve has been included for timing reference only and, as such, its axis has been inverted and left off

the plot for clarity. The pitch velocity is almost perfectly in phase with the surge velocity (see motions in Figure 28) and is left off the plot. Note the thrust and power are seen to be in phase with these velocities which are, in turn, 180° phase shifted from wave height. This suggests that the maximum aerodynamic power is developed at the wave trough and the minimum power at the wave crest. The generator power curve of NREL has substantially less deviation and is shifted almost a full 90° and thus cannot be properly compared to the aerodynamic power curve developed in this chapter. A variable-speed (VS) controller is necessary, therefore, for proper power and performance predictions, which is detailed in chapter 6. An instantaneous prediction of the vortical structures in air is shown in Figure 31 using iso-surfaces of the second invariant of the rate of strain tensor—the Q-criterion from (Hunt et al., 1988). This is defined as:

$$Q = \frac{1}{2} \left(|\mathbf{\Omega}|^2 - |\mathbf{S}|^2 \right) > 0 \quad (4.23)$$

where $\mathbf{\Omega}$ and \mathbf{S} are the vorticity tensor and strain rate tensor, respectively. For a continuous velocity field $\mathbf{v}(\mathbf{x}, t)$ these are defined as:

$$\begin{aligned} \mathbf{\Omega} &= \frac{1}{2} \left(\nabla \mathbf{v} - (\nabla \mathbf{v})^T \right) \\ \mathbf{S} &= \frac{1}{2} \left(\nabla \mathbf{v} + (\nabla \mathbf{v})^T \right) \end{aligned} \quad (4.24)$$

In Figure 31 the platform has reached the crest of the wave and is at maximum surge/pitch velocities away from the incoming wind and waves. The rotor is interacting with its wake and power development is at a minimum.

The black circles on the power time-history plot represent the blades passing in front of the tower. An instantaneous result of this is shown in Figure 32. In Figure 32a the blade is passing in front of the tower, marked in the image. In Figure 32b the rotor has rotated 180° and the blade is now pointing away from the tower in the freestream. Significant discontinuities in power generation occur when the tower interferes with the blade aerodynamics. Note, however, not all of these discontinuities necessarily produce decreases in power. The platform begins surging/pitching away from the incoming wind and waves as

the wave trough passes the platform (at $t=5, 15$ s in Figure 28) and the system begins shifting toward the vortex ring state described in (Sebastian et al., 2010) which may be affecting the BTI. A better understanding of these aerodynamic phenomena and their coupling could be used to minimize these power discontinuities. This, in turn, can lead to smoother electrical operation as well as less vibration and fatigue.

4.6 Conclusions

A general quasi-static crowfoot mooring line model is developed and applied to the OC3-Hywind FOWT system. Free-decay time-series tests are performed for both the crowfoot model and the OC3's AYS model for validation. The time-series results of cases 1.4b and 1.4c agree on amplitude with the results of the OC3's simulations but the two models both show frequency differences, when compared to experimental data, in surge caused by variances between simulations, including different restoration between mooring models and modeling error. These results, coupled with the low computational cost of the crowfoot model, alleviate the need to approximate a crowfoot mooring system and open avenues for optimization and application to other FOWT models.

The crowfoot model is used in a full system two-phase CFD simulation with steady wind and wave excitation based on OC3 case 5.1. Results are compared to those of the NREL's OC3 results using FAST. The trends of the present results' motions agree well with the NREL, showing 25% less mean surge and a slight phase difference in heave. Morison's equation utilizes a streamwise drag coefficient, set to a constant 0.6 in the OC3's simulations, and has no mechanism for capturing viscous effects in heave. These hydrodynamic solution differences are likely the reason for most of the motion discrepancies between FAST and the present study. The crowfoot model is shown to decrease yaw from the AYS model used by NREL-FAST. The present results also show that system yaw is largely a function of the instantaneous rotor position, which implies that wind is a significant factor in system yaw. The power generated is strongly correlated with relative changes in wind velocity due to superimposed surge and pitching velocities. These surge and pitch velocities are 180° phase shifted from the instantaneous wave height such that the maximum aerodynamic power is seen at the trough of the wave and the minimum aerodynamic power

at the crest. It is observed that aerodynamic disruption, occurring when the blade passes in front the tower, causes substantial discontinuities in power generation, but that these discontinuities may have varying effects on power generation depending on instantaneous pitch and surge velocity. The crowfoot model is concluded to be ready for application in further simulations in this dissertation.

4.7 Figures

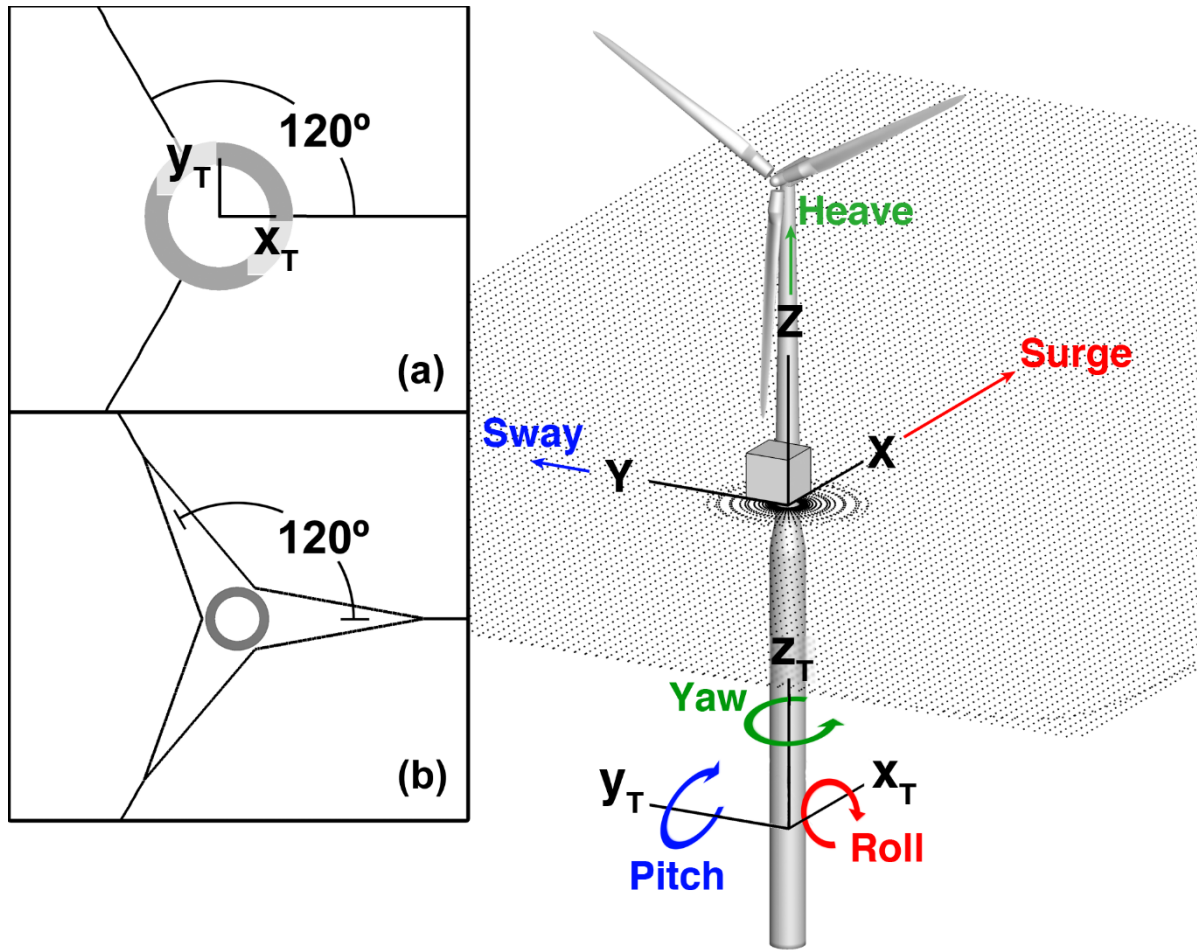


Figure 19 Catenary mooring line configurations and coordinate frames: (a) 2-Point line fairlead connections (from above), (b) Crowfoot line fairlead connections (from above)

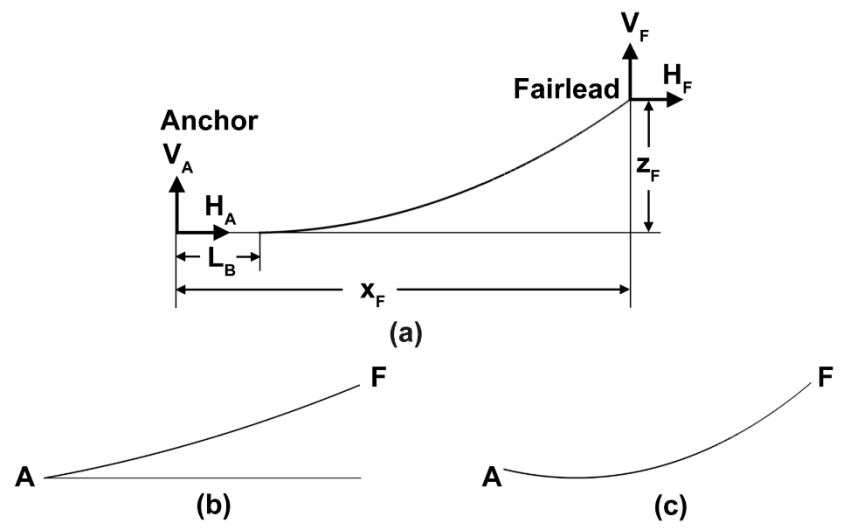


Figure 20 Two-dimensional catenary forces and line configurations. (reproduced from (Jonkman, 2007)): (a) Line resting on seabed,(b) Taut line,(c) Slack line

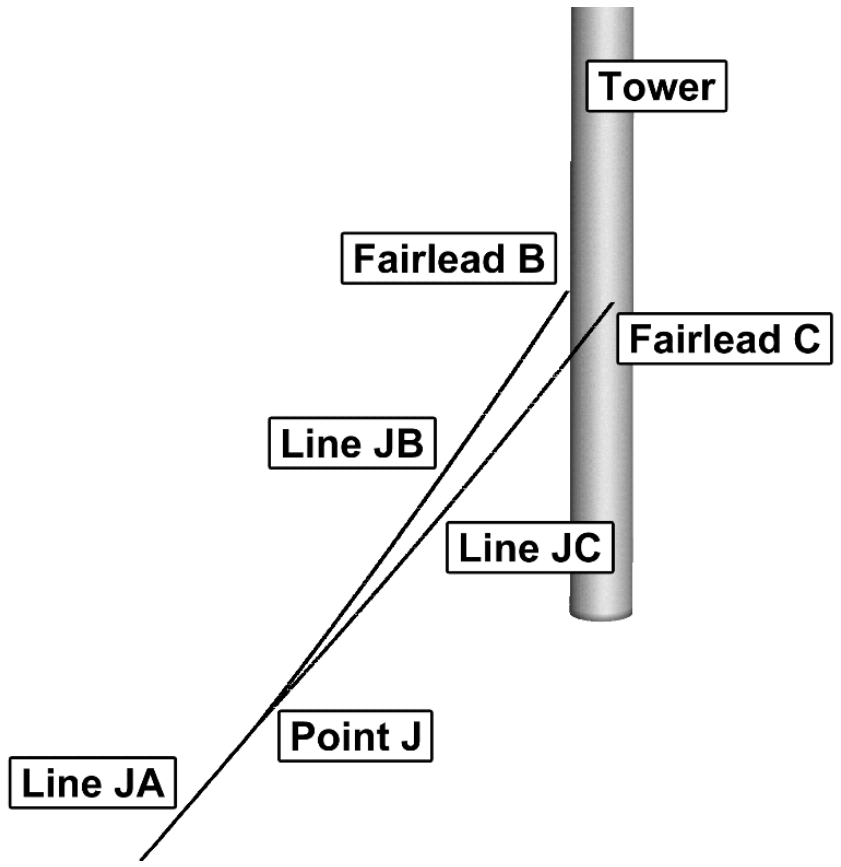


Figure 21 Crowfoot connection to fairleads with descriptions

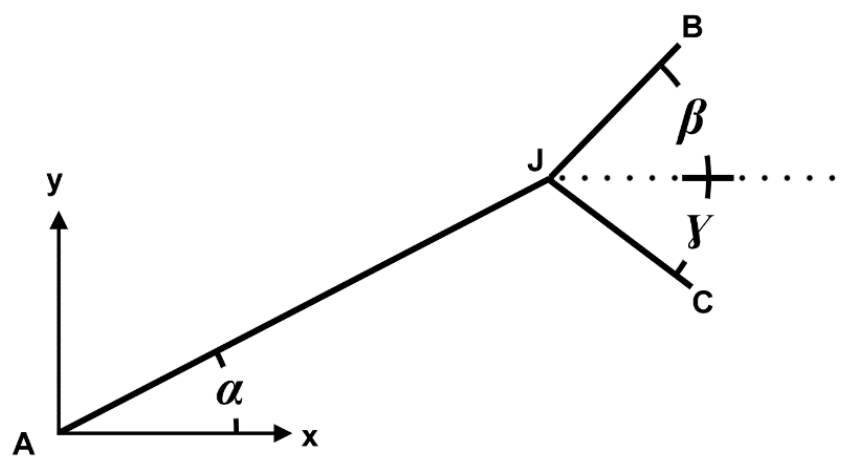


Figure 22 Crowfoot XY plane angles

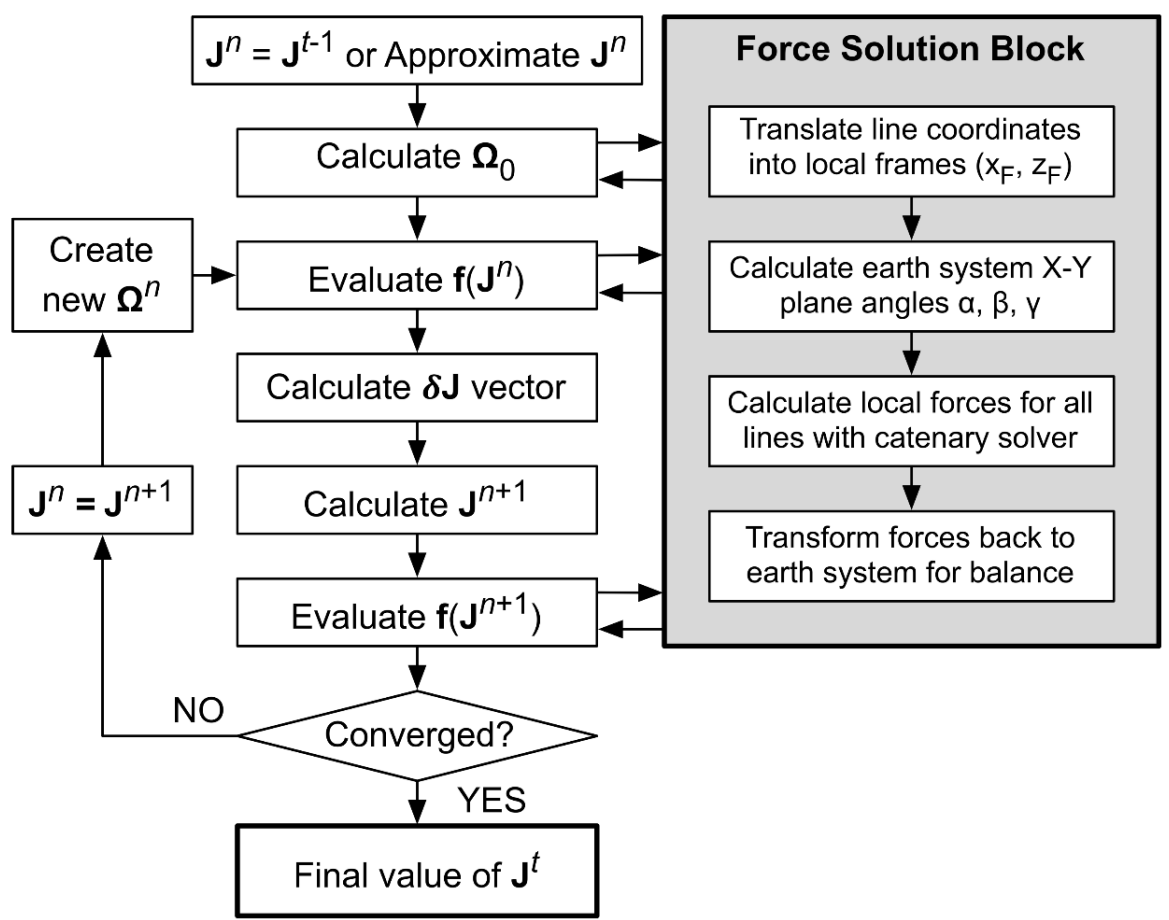


Figure 23 Broyden's method solution process

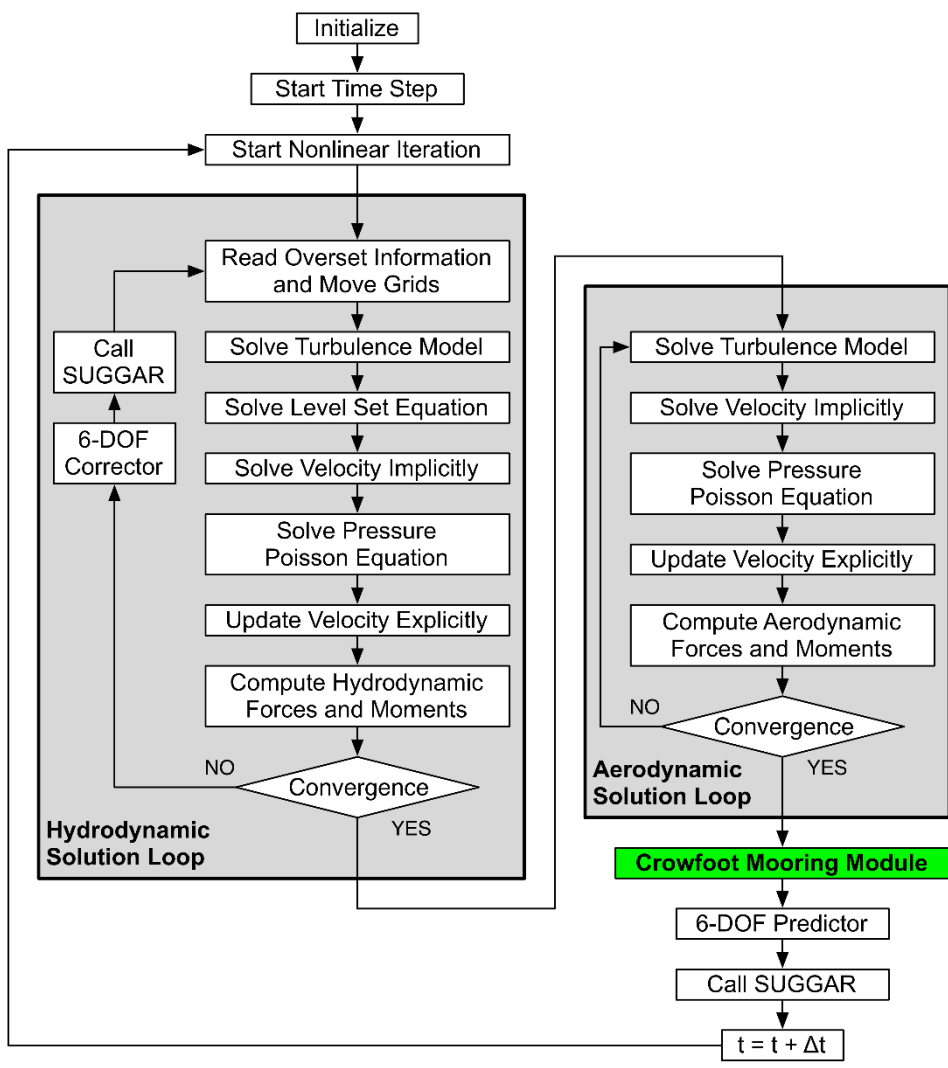


Figure 24 Solution strategy

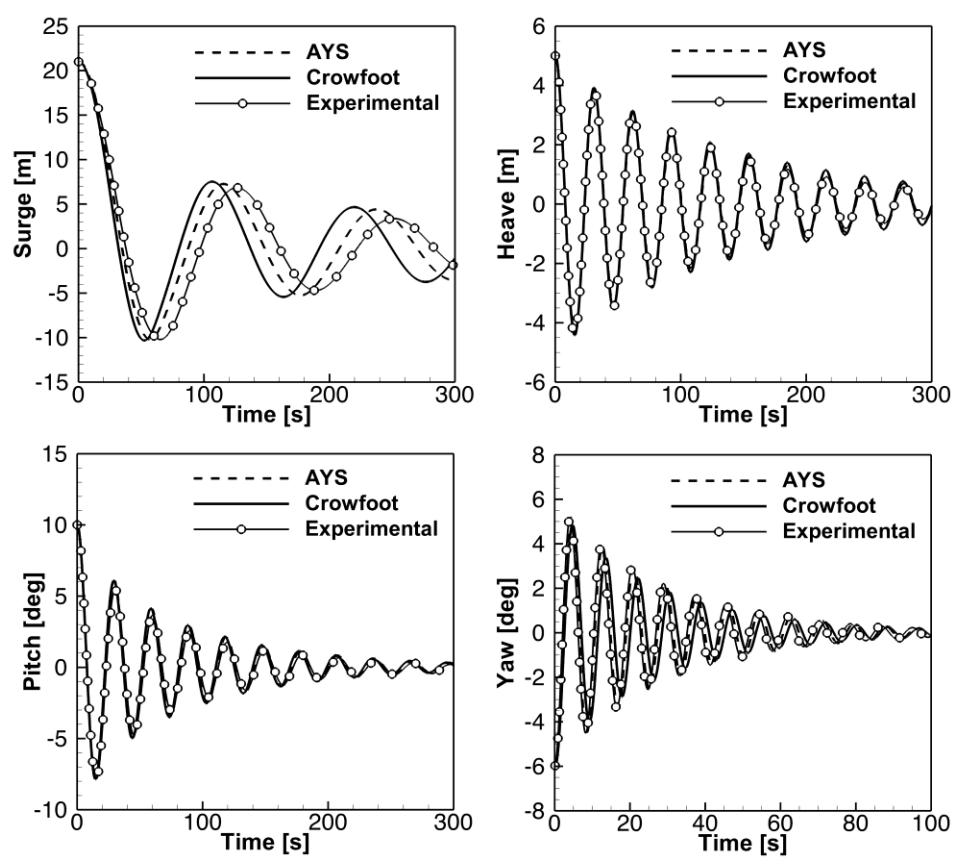


Figure 25 Surge, heave, pitch, and yaw results in cases 1.4b and 1.4c

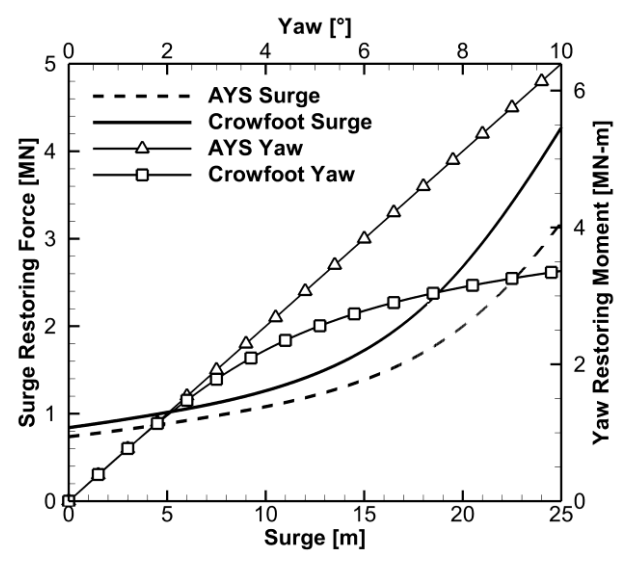


Figure 26 Surge and yaw restoring comparison of a single crowfoot line and a single AYS line

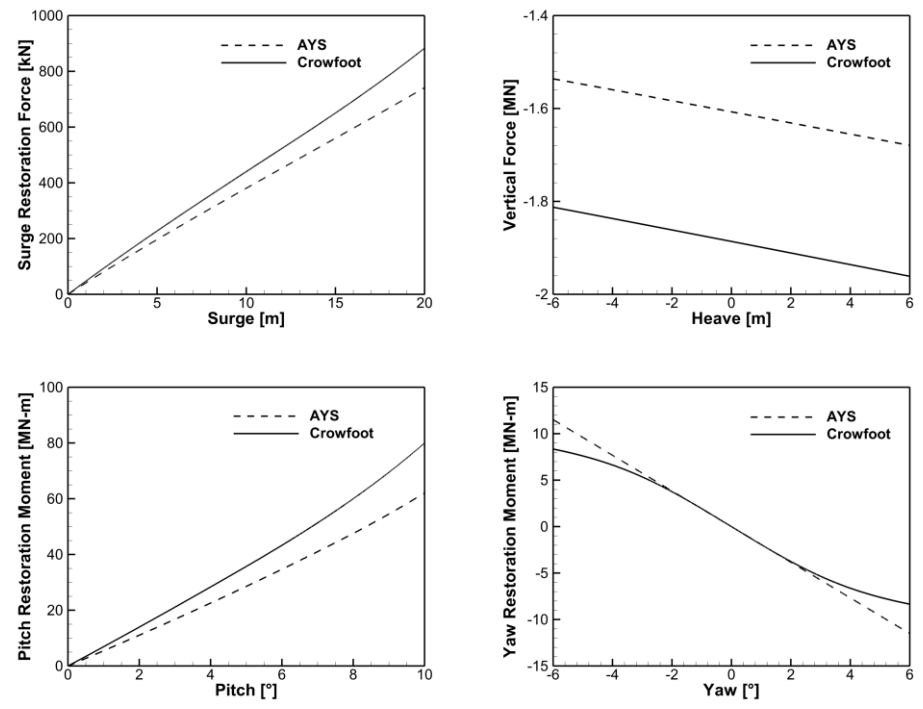


Figure 27 Net restoration comparison of crowfoot and AYS mooring lines

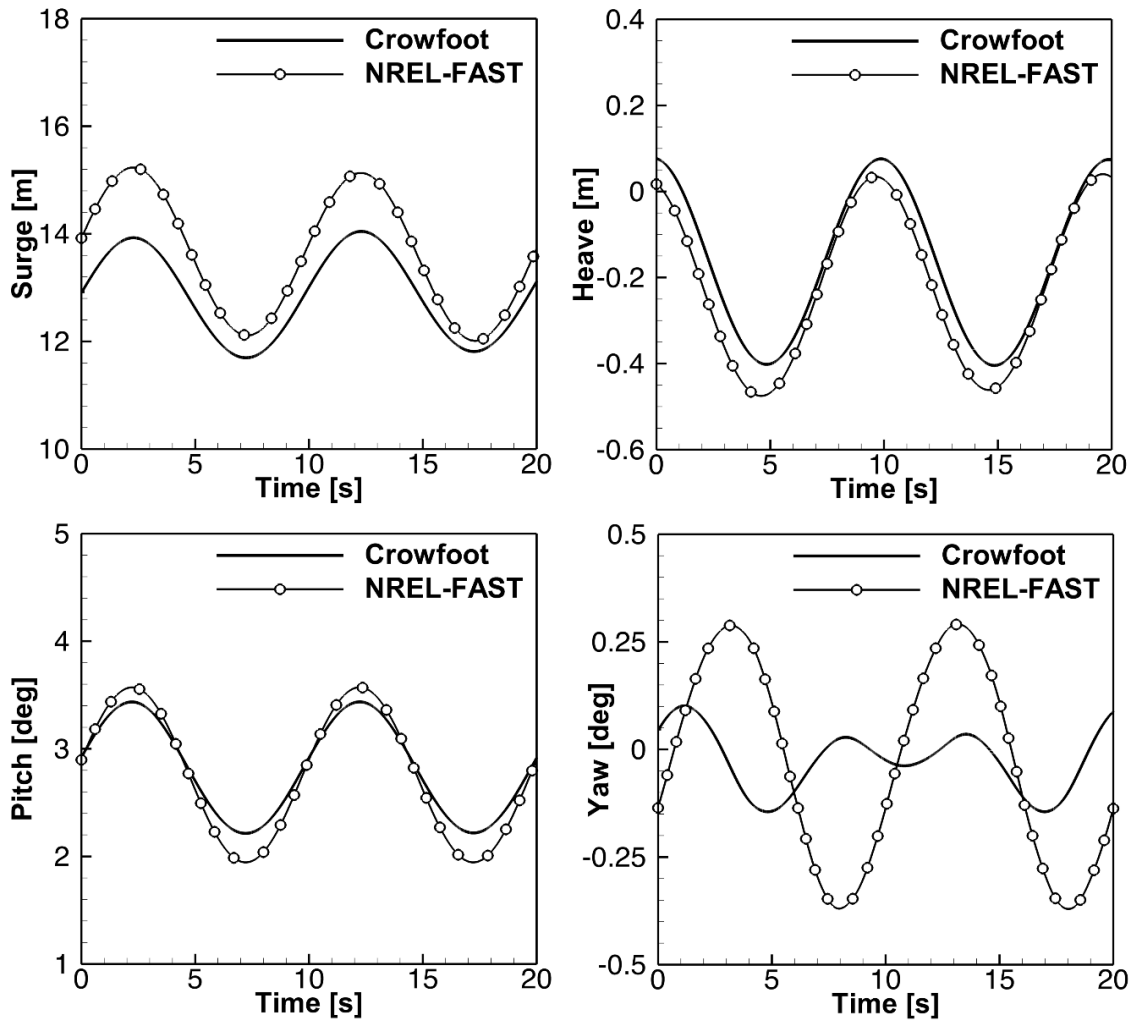


Figure 28 Platform motions in case 5.1

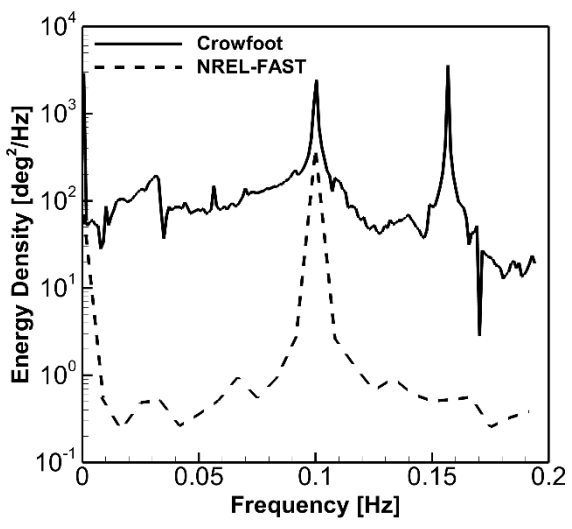


Figure 29 Fourier transform of yaw motions from case 5.1

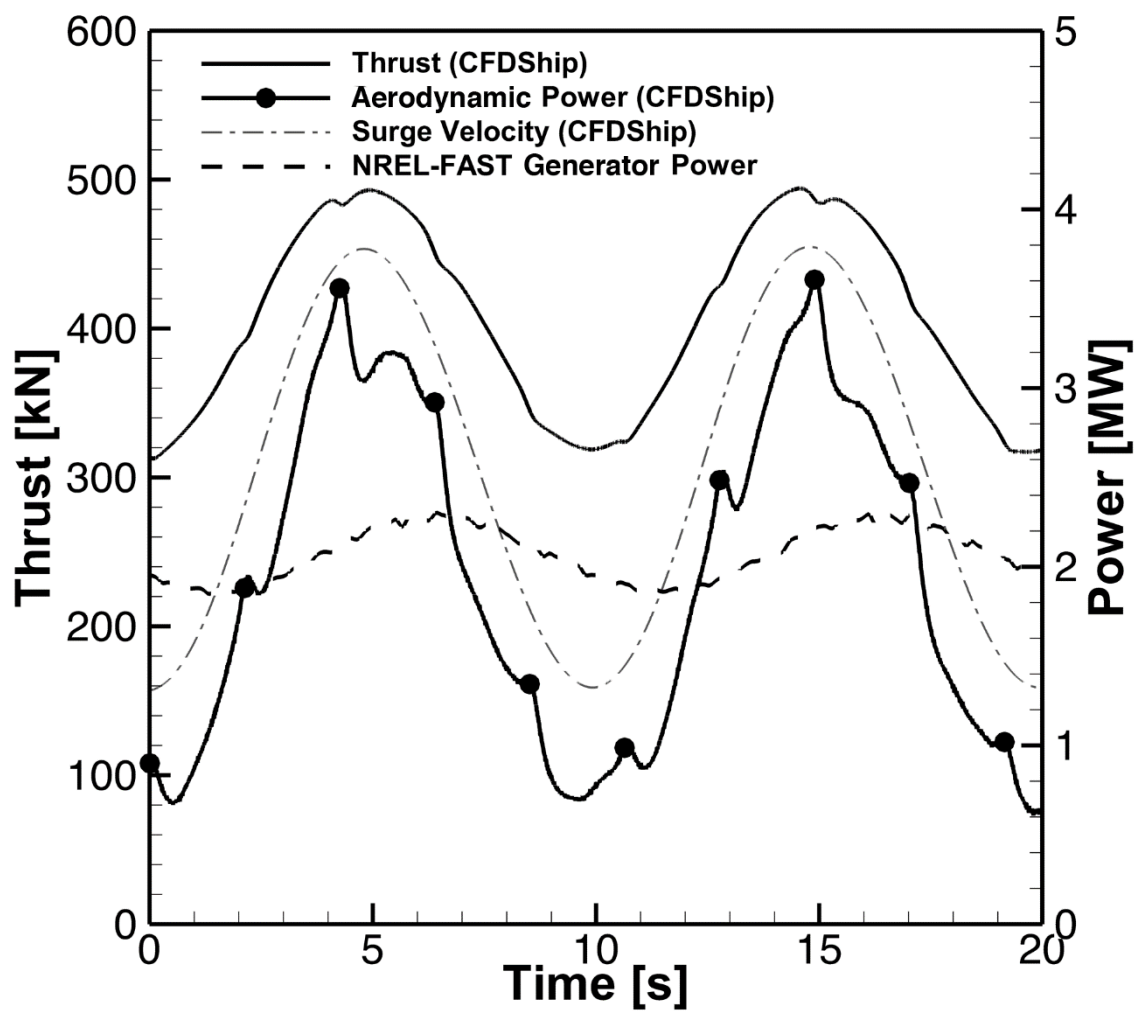


Figure 30 Power and thrust time histories in case 5.1

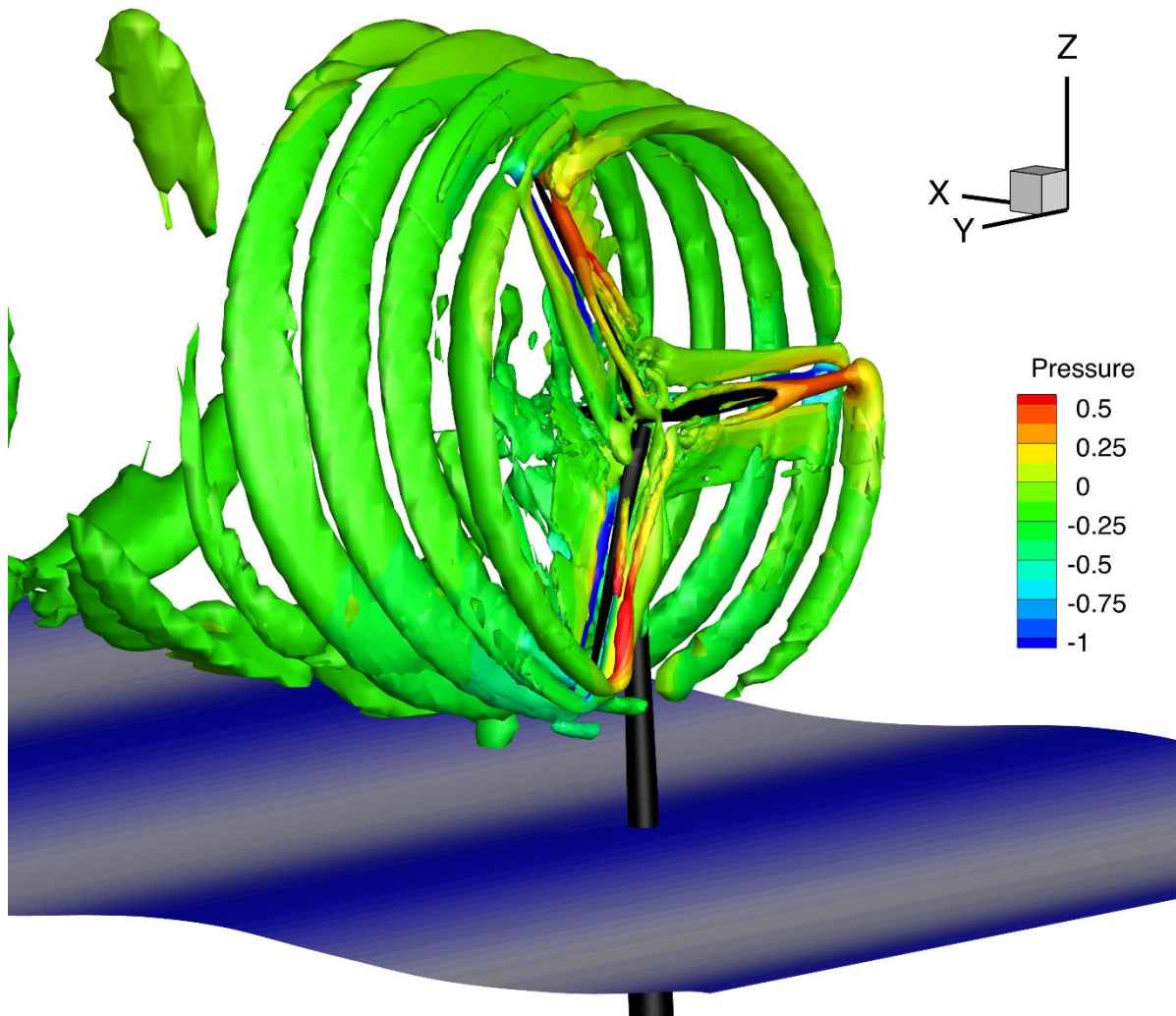


Figure 31 Predicted vortical structures (iso-surfaces of $Q=0.5$ colored by pressure). Free-surface is maximum (3 m) in light gray and minimum (-3 m) in dark gray.

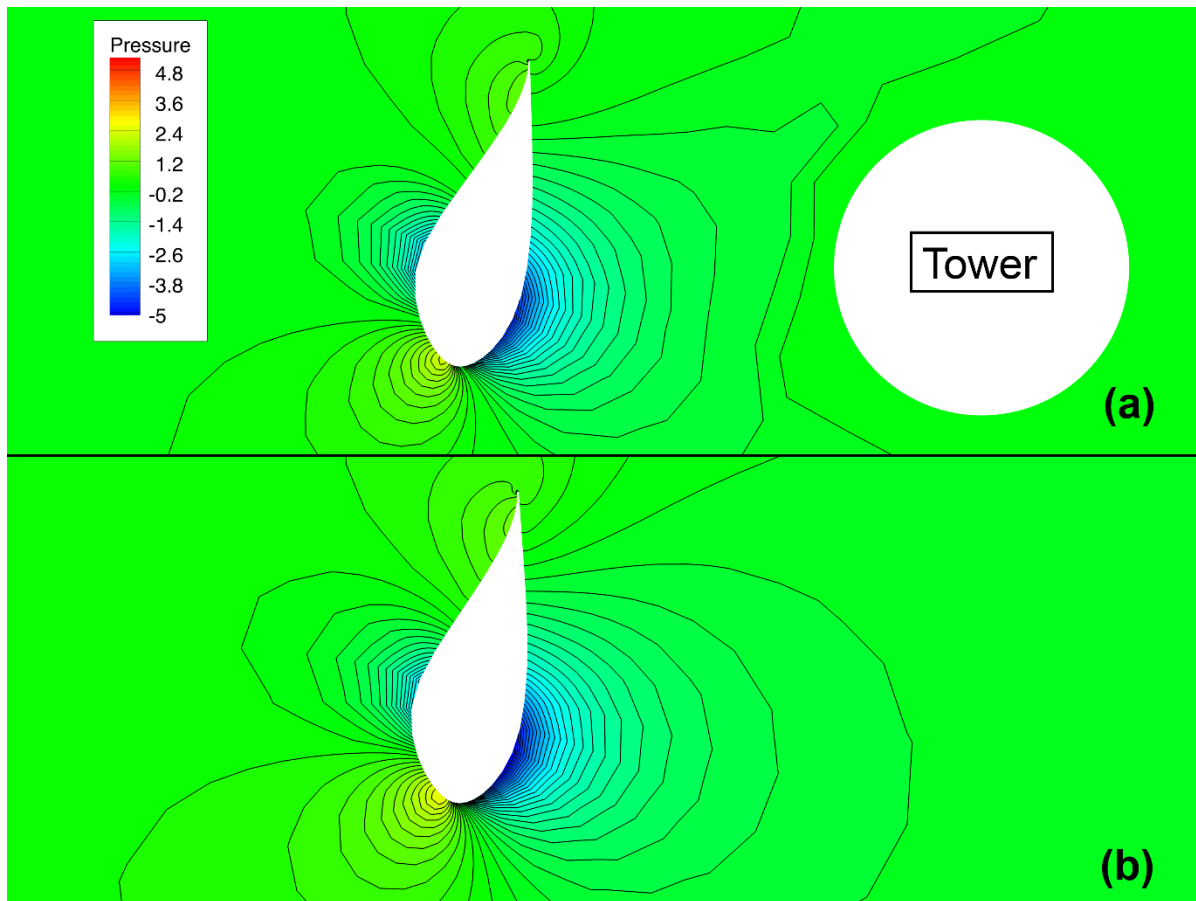


Figure 32 Aerodynamic effects of tower on pressure contours at $r/R=0.2$ along the blade length: (a) Blade passing in front of tower, (b) Blade 180° from tower

4.8 Tables

Table 4 Mooring model properties

Line Model	Unstretched Lengths [m]	Line Weight in Water [N/m]	Extensional Stiffness [N]	Tower Mass [kg]
2-Point & AYS	902.2	698.1	3.84E8	8.054E6
Crowfoot	JA: 811.98 JB: 90.22 JC: 90.22	698.1	3.84E8	8.025E6

Table 5. Simulation matrix.

Case	Wind Conditions	Wave Conditions	Mooring Model	Rotor RPM	Analysis
1.4b	Air Density = 0	Still water	AYS	N/A	Free-Decay Time-series (Each DOF individually)
1.4c	Air Density = 0	Still water	Crowfoot	N/A	Free-Decay Time-series (Each DOF individually)
5.1	Steady wind 8 m/s	Regular: H=6 m; T=10 s	Crowfoot	9.4	Time-series

CHAPTER 5: AN INVESTIGATION OF THE BLADE TOWER INTERACTION OF A FLOATING OFFSHORE WIND TURBINE[‡]

5.1 Abstract

This chapter investigates the effect of blade tower interaction (BTI) on power generation of a floating offshore wind turbine (FOWT) with platform pitching and surging motion. The fine grid set is used in three simulations: a rotor-only simulation, a full-system simulation including the tower, nacelle, and platform (TNP), and a third simulation in which the TNP is included and but a larger rotor overhang is used. The results of these simulations are compared for analysis of the aerodynamic disruption that occurs when the blade passes in front of the tower (BTI). The results show that the pitching motion of the platform has little effect on shaft thrust but has a significant effect on the pressures developed near the blade and tower. These results can potentially be used to understand the nature of the FOWT BTI for future design of turbine blade aerodynamics and structure, to help establish an empirical BTI correction model applicable to FOWT, or to aid in design of a control scheme to help mitigate power losses due to BTI.

5.2 Introduction

Horizontal axis wind turbines (HAWT) predominantly come in an upwind rotor configuration, which is the configuration of interest in this dissertation. Upwind HAWTs must utilize a passive tower to locate the rotor above the ground for blade clearance and to take advantage of the reduction of wind shear found at distances sufficiently far from the surface. The HAWT tower, however, is detrimental to the aerodynamics of the individual rotor blades when the blades pass directly in front of it. This effect, called BTI herein, can cause a reduction in shaft thrust and modify bending moments along the blade and at the blade root where the blade connects to the rotor hub. The BTI effect has been well established and known for years yet relatively few studies exist on it. Graham *et al.* utilized

[‡]Results presented at The Twenty-fifth International Offshore and Polar Engineering Conference (ISOPE-2015). Kona, Big Island, Hawaii, USA, June 21-26, 2015. Paper 2015-TPC-0991.

Panel 64. REES WIND TURBINE VII: Floating Turbines 3

KEYWORDS: Blade-tower interaction; floating offshore wind turbine; spar-buoy; CFD; OC3; Hywind

both upwind and downwind configurations in experiments examining different tower fairings (shrouds to change the effective aerodynamic shape of the tower) to help lessen BTI effects (Graham et al., 2001). The authors concluded that different tower fairings produced no significant change in disruption for upwind rotors and that BTI is “small for upwind rotors provided the rotor-tower gap is at least one [tower] diameter.” Bak *et al.* (Bak et al., 2001) developed an upwind rotor model by modifying the cylinder potential flow solution from (Parkinson et al., 1970) with a term accounting for tower drag. This model is currently the model used by FAST (Jonkman et al., 2005) for upwind rotor wind turbine simulations. Some simulations investigating BTI of upwind HAWT have been performed in recent years. All studies listed here utilized the onshore NREL Phase VI experimental turbine (upwind configuration) developed by Hand *et al.* (Hand et al., 2001). Kim *et al.* developed a vortex lattice correction method (Kim et al., 2010) which was then utilized in (Kim et al., 2011). The authors showed that the thrust loss due to BTI is inversely proportional to incoming wind speed and that a decrease in tower radius was more effective in reducing BTI effects than an increase in rotor overhang. Wang *et al.* used CFD to study BTI but with quite coarse grids (Wang et al., 2012). They also showed an inverse proportionality between incoming wind speed and thrust loss and that the BTI effect has dissipated at 180° rotor azimuth (where 0° azimuth is located directly in front of the tower). This study was unique in that it also discussed the effect of BTI on the tower, not just on the blades and shaft.

The objective of this chapter is to analyze the effect of BTI on a FOWT experiencing pitching and surge motions using CFD and advanced turbulence modeling on a high-resolution grid set containing 20 million points. These pitch and surge motions are prescribed as sinusoidal inputs and are perfectly in phase using the wave period of 10 s. The inputs are divided into four distinct regions (R1-R4), corresponding with the 4 quadrants of the wave phase space, for comparison: R1 (wave crest) is at maximum downstream velocity and mean positions, R2 (mean wave height, decreasing) is at zero streamwise velocity and maximum downstream platform positions, R3 (wave trough) is at maximum upstream velocity and mean position, and R4 (mean wave height, increasing) is at zero streamwise velocity and maximum upstream position. Time histories of thrust, measured in degrees of rotor azimuth, and blade section pressure (Carrica et al., 2007a) contours are analyzed.

5.3 Mathematical Modeling and Methods

The OC3-Hywind (Jonkman, 2010, Statoil, 2012) is shown in Figure 33 along with the three coordinate systems used in this study. The earth-fixed system (X, Y, Z) is located at the still water line (SWL) and the moving turbine frame (x_T, y_T, z_T) is located at the center of gravity of the overall system, identical to the frames used in chapter 4. In the initial position seen in Figure 33 (before pitching and surging displacement) the turbine system is oriented to the earth system and is located at the center of gravity of the overall system at $[-0.018 \text{ m}, 0, -78 \text{ m}]$ in the earth frame. This chapter introduces a 2-dimensional system (x_B, y_B), seen in the inset of Figure 33, for analyzing blade section pressure contours. This system originates at the pitch axis of the particular blade section.

5.3.1 Numerical Methods and Solution Strategy

The fine grid set, detailed in chapter 3, is utilized for all simulations in this chapter. Delayed detached eddy simulation (DDES) (Xing et al., 2010a) is utilized in these simulations for its ability to predict massively separated flows expected around the blades and tower.

A second-order upwind finite-difference is used to discretize the momentum terms and a fourth-order hybrid scheme for level-set convection terms, which switches between first order close to solid surfaces and fourth-order beyond. The level-set convection term accuracy is increased from the second-order accuracy used in chapter 4 to help reduce wave height dissipation, observed in the results of chapter 4. A second-order backward differencing scheme is used for discretizing temporal terms.

5.4 Simulation Conditions and Design

Three simulations are performed in this chapter, each using a configuration displayed in Figure 34. A theoretical maximum configuration (BTI 2) utilizes only the rotor, removing the TNP, and is referred to as the “no TNP” simulation in plots and discussion to follow. The other two simulations use the full system including the TNP. The first of these latter two simulations (BTI 1) has the rotor set at the 1.912 m overhang defined in (Jonkman et al., 2009), referred to as the “1x Overhang” simulation. The final simulation (BTI 3) doubles

this overhang (3.824 m) to determine the effect of moving the rotor farther from the tower. This simulation is referred to as the “2x Overhang” simulation.

Sinusoidal pitch and surge motions are prescribed, in the fixed earth frame, for the system. Identical motions are prescribed for all three simulations. The motions are derived based on average motions predicted by the National Renewable Energy Laboratory’s (NREL) in their Offshore Code Collaboration Comparison (OC3) load case (LC) 5.1 results (Jonkman et al., 2010). Both the pitch and surge DOFs are seen in NREL’s results to be predominantly excited by incoming waves. This is the frequency used for both inputs. The motion inputs, in the earth coordinate frame, are described by

$$S = -3.635 + 0.45 \sin(0.2\pi t) \text{ [m]} \quad (5.1)$$

$$P = 0.048 + 0.0141 \sin(0.2\pi t) \text{ [rad]} \quad (5.2)$$

where S is the surge in meters, P is the pitch in radians, and t is the simulation time. All motions and velocities are considered positive when the system is moving downstream and negative as the system moves upstream. At $t = 0$ s the system is at its mean position but at maximum velocity, which defines R1. The maximum downstream position and zero velocity occurs at $t = 2.5$ s, which defines R2. The system then begins moving upstream reaching its mean position but with minimum velocity at $t = 5$ s, which defines R3. The final quadrant of the cycle, defined as R4, is reached at $t = 7.5$ s when the system has reached its minimum position and a zero velocity. The cycle begins again at $t = 10$ s and continues on through the duration of the simulation. These region descriptions and their corresponding pitch and surge motions are presented in Table 6. Rotor angular motions are fixed at 9.4 RPM in the present study corresponding to the average rotor velocity from NREL’s OC3 LC 5.1 predictions. The period of the rotor is 6.38 s, which is not an even multiple of the 10 s motion period. Although there are three blades, examination shows that the BTI effect observed for one blade in R1-R4 is also observed for the other two blades for R1-R4 at different times. The wind velocity is fixed at a steady 8 m/s and regular Airy waves ($H = 6$ m, $T = 10$ s), the same conditions used in the OC3 LC 5.1, are used for all simulations. The present simulations were allowed to run sufficiently long to develop the rotor wake far downstream and to capture a blade at 0° azimuth in each of the four motion regions.

5.5 Results and Discussion

Azimuth vs. shaft thrust results are presented in Figure 35 through Figure 38, one for each motion region, showing thrust over a rotor azimuth range from 60° ahead of the tower to 60° beyond the tower. The pitch velocity curve is also shown for timing reference. The surge velocity curve is perfectly in phase with the pitch velocity curve and is not shown for clarity. The thrust plots all show similar trends in both amplitude and azimuthal range of thrust loss. Figure 39 shows the BTI effect in R1, as the system is moving downstream at its maximum velocity, the 1x simulation shows a thrust loss of 5.9 kN, which is 4.6% relative to the no TNP simulation. The 2x simulation shows a thrust loss of 3.6 kN, a relative difference of -2.8%. The BTI effects begin at approximately -30° rotor azimuth and dissipate at approximately 40° rotor azimuth. This agrees with previous studies (Zahle et al., 2009, Wang et al., 2012) which all show effects in approximately this same 70° range on different, onshore turbine models. Excellent visuals showing the onshore, fixed tower BTI effect vs. rotor azimuth are seen in (Zahle et al., 2009), which are similar to what the OC3-Hywind would produce in the absence of platform motions. This suggests that this range is independent of model size, rotation velocity, and relative motion of the platform. This is a significant feature in BTI studies and provides a general azimuthal range of concern for potential blade pitch controller schemes looking to mitigate BTI losses and bending. Figure 36 presents the BTI effect in R2, where the system has stopped moving and is at maximum downstream displacement (maximum surge and pitch), the 1x simulation shows a 6.7 kN thrust loss (-4.4% relative) compared to the no TNP simulation while the 2x simulation shows a 4.8 kN loss (-3.2% relative). The azimuth range of BTI effect is similar to that of R1. Figure 37 shows the BTI effect in R3, where the system is moving upstream at its minimum velocity, the 1x simulation shows a thrust loss of 7.2 kN (-3.7% relative) compared to the no TNP simulation and the 2x simulation shows a 4.1 kN (-2.2% relative) loss. Figure 38 shows the BTI effect in R4, where the system has stopped moving and is at its minimum downstream displacement, the 1x simulation shows a 7.2 kN (-4.1% relative) thrust loss compared to the no TNP simulation while the 2x simulation shows only a 5.2 kN (-2.9% relative) thrust loss. These results are presented for ease of comparison in Table 7. The absolute thrust losses are similar in R2 and R4, where the system is experiencing no

relative motion. The small differences are likely due to the difference in projected rotor plane between the R2 and R4 regions. R2 is pitched at 3.56° (maximum pitch) while R4 is pitched at 1.94° (mean pitch), keeping more of the rotor plane perpendicular to the incoming wind. The largest relative thrust loss occurs in R1. This is due to the pressure developed around the tower as the system moves downstream. As the system moves downstream, and the tower experiences a lower relative incoming wind velocity, the high pressure on the upwind side of the tower decreases and the lower pressure on the downwind side of the tower increases as expected by a potential-flow solution. The blade's suction side, which faces the tower, runs into a relatively lower pressure than in any of the other 3 regions causing less of a BTI effect. It would be interesting to see what a higher pitching velocity would cause in R1, although a higher pitching velocity would probably be correlated with a higher incoming wind velocity and previous studies (Kim et al., 2011, Wang et al., 2012) have suggested that this higher incoming wind velocity would itself decrease the BTI effect.

CP difference plots in the blade coordinate system at 0° azimuth are presented in Figure 39 through Figure 42, one for each region. The plots show the difference between predicted CP for the 1x simulation and the no TNP simulation in the top plots and the difference between the 2x simulation and the no TNP simulation in the bottom plots, where the gap between the blade and tower has visibly increased. These differences are calculated by subtracting the results of the no TNP simulation from each of the 1x and 2x simulations. Included with each pressure contour plot is an inset zoomed into the blade section for a closer look at the contours right at the blade surface. Due to overlapping grid interpolation the contour plots have some extra short lines at points where grids meet and are cut, notably between the tower and blade grids. R1 is shown in Figure 39. Minimal differences are seen at the tower in both the 1x and 2x simulations. This is due to the relative motion of the tower (moving downstream) helping to decrease the incoming wind velocity experienced by the system. The lower pressure developed in front of the tower in R1 produces a lower pressure increase on the leading edge (LE) of the suction side of the blade and in the gap between the blade and the tower than is seen in other regions. These pressures have little effect on the location of the stagnation point of the LE. A similar effect is seen in the 2x difference plot, but with less difference than the no TNP simulation. The pressures of the rear half of the blade

section show little difference for both simulations. The contours of R2 are shown in Figure 40. Here the system is not moving and a more traditional circular cylinder pressure distribution is seen along the circumference of the tower. The pressure of the upwind side of the tower is higher than experienced in R1. Propagation of this higher pressure to the blade produces a larger difference on the suction side LE. This pushes the LE stagnation point toward the pressure side of the blade promoting separation by both increasing streamline curvature as well as increasing the effective Reynolds number on the suction side of the blade. The latter point can be seen on the rear half of the suction side toward the trailing edge (TE) in both the 1x and 2x simulation differences in Figure 40. The higher LE pressure accelerates the flow toward the TE due to Bernoulli's principle and both the 1x and 2x simulations show lower pressures due to the presence of the tower. This suggests that the center of pressure of the blade will move due to BTI and will produce a moment about the blade pitch axis. Figure 41 shows differences for R3, where the platform velocity produces the highest relative wind velocity seen by the system. The pressure upwind of the tower has increased and, accordingly, so has the pressure on the LE of the suction side. The stagnation point in R3 has been pushed even farther onto the pressure side of the blade than in either of R1 or R2 and the pressure on the rear half of the suction side of the blades has decreased substantially. The Kutta condition requires the pressure of both sides of the blade to be equal at the TE. This effect is much more significant in R3, pushing a higher pressure onto the rear half of the pressure side of the blade and producing a steep pressure gradient close to the TE of the suction side. This could potentially cause vibration and fatigue at the thin TE blade section as the pressure differences due to BTI disappear after the $\sim 40^\circ$ azimuth range discussed earlier. Similar to both R1 and R2 these effects exist to a lesser magnitude in the 2x simulation when compared to the 1x simulation. R4 is presented in Figure 42. The 1x simulation contour plot shows a notably lower freestream pressure than that of both the no TNP and 2x simulations (evidenced by the lighter blue contours upstream of the blade) making comparison difficult. However, comparing the 2x simulation differences between R4 and R2, where the system is at zero relative velocity, shows similar magnitudes and locations of differences. The differences between R2 and R4 could potentially be attributed to several possibilities, including the phase difference in tower shedding between

simulations as, at the times chosen to represent R2 and R4, a vortex is being shed from the opposite lateral side of the tower evidenced by the low pressure contours just downstream of the tower in Figure 40 and Figure 42. The vortex shedding frequency of the tower, which is unsteady due to platform motion, may have a significant effect on the magnitude and positions of the BTI effect on the blade but is beyond the scope of the current study.

Iso-surface plots colored by C_P of the 1x simulation and the no TNP simulation are presented in Figure 43 and Figure 44, respectively. Vortical structures are visualized using the Q-criterion (Hunt et al., 1988) to show the effect of the tower's presence on tip vortices and the rotor wake. Figure 43 shows vortical structures behind the tower blending with the vortices being shed from the blade roots. Destruction of tip vortices can be clearly seen in Figure 43 as a tip vortex has convected downstream and collided with the tower at the instant presented. Also visible is the numeric dissipation of the vortices as they convect out of the wake refinement grid. Figure 44 shows the theoretical limit of the helical wake as the tower is non-existent. Wake skewing due to pitching and wave motion are also clearly visible in Figure 44. The wave and pitch frequency are identical in the present study making it difficult to identify the isolated effect of each motion, but the wake is clearly more skewed closer to the free-surface indicating that the wave undulation has a significant effect on wake skewing.

5.6 Conclusions

Simulations of the OC3-Hywind, one in the documented configuration, one with a doubled rotor overhang, and one without the TNP, are performed to determine the effect of platform streamwise motions, a unique feature of FOWT, on blade tower interaction (BTI). Streamwise motions are prescribed using a sinusoidal analytic function. These motions are divided into four regions corresponding to minimum, maximum, and zero platform velocities. Results are compared to determine differences between the three geometric configurations in shaft thrust and pressure at the blade, tower, and surrounding regions. The results show that upstream platform pitching and surging motion produces a more significant BTI effect on shaft thrust when compared to downstream platform pitching and surging motion. The BTI effect is observed to begin at approximately 30° of azimuth before

the tower and extends to approximately 40° of rotor azimuth after passing the tower for all motion regions. This azimuthal range could potentially be used as the first approximation in the development of an individual blade pitch control scheme attempting to mitigate BTI effects. The detrimental effects of BTI are shown to have more of an effect on the suction side than on the pressure side of the blade, increasing the Reynolds number of the back half of the suction side decreasing the pressure at the blade surface. These pressure differences potentially cause a moment about the individual blade's pitch axis. A higher pressure gradient forms on the rear half of the blade's suction side as the Kutta condition takes hold potentially causing vibrations at the thin TE. The results show that, due to platform motions in regions R2-R4, the BTI effect causes a larger pressure on the suction side at the LE forcing the stagnation point farther onto the pressure side, which could help promote separation and stall. The negative effects caused by these pressure variations could potentially be aided by blade profiles specifically designed to alleviate BTI, necessitating a more complete understanding of the physical BTI effects.

5.7 Future Work

The bending moments seen at the blade root are the largest moments on the blade and the effect of BTI on the magnitude of these moments, as well as the direction change of principal bending axes at the root need to be determined. Only one set of pitch and surge magnitudes and frequency were investigated. In the future multiple magnitudes and frequencies should be studied to find trends and further points for study. Further developments could include a pitch control scheme to help minimize displacement of the stagnation point on the LE of the blade. Asymmetric tower fairings could also be investigated to help mitigate the effects of BTI. Existing solution verification methods developed for RANS (Xing et al., 2010b) are not applicable to DDES where the LES region has coupled numerical and modeling errors. A new framework for verification for LES (Xing, 2015) may be evaluated and implemented.

5.8 Figures

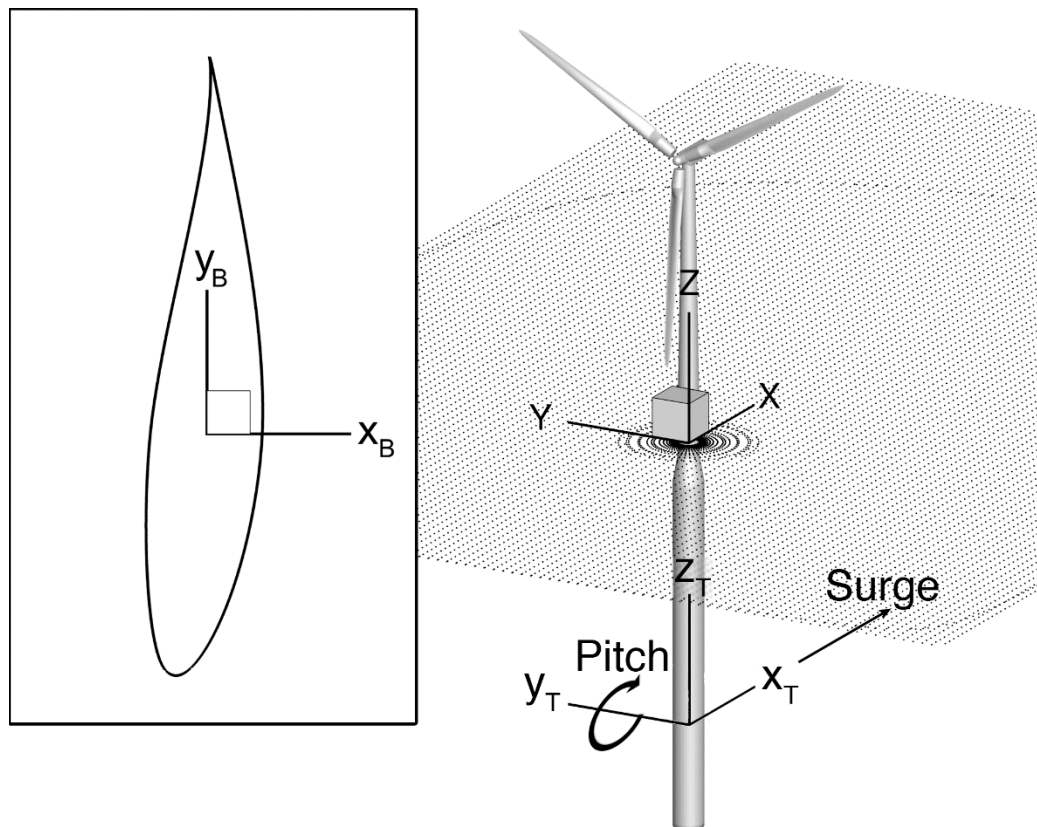


Figure 33 Three coordinate frames: earth-fixed frame (X, Y, Z), turbine system frame (x_T, y_T, z_T), and 2-D blade section system

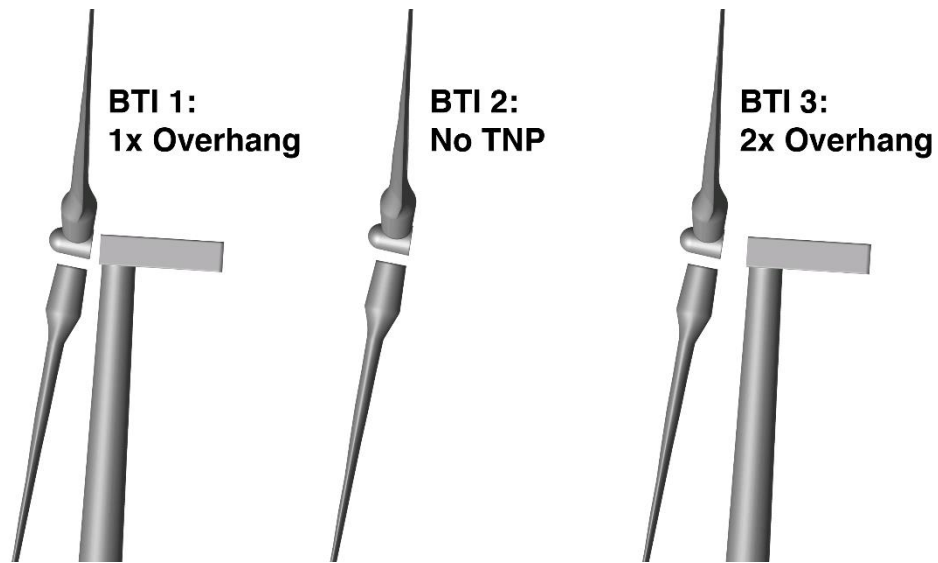


Figure 34 Three different configurations used

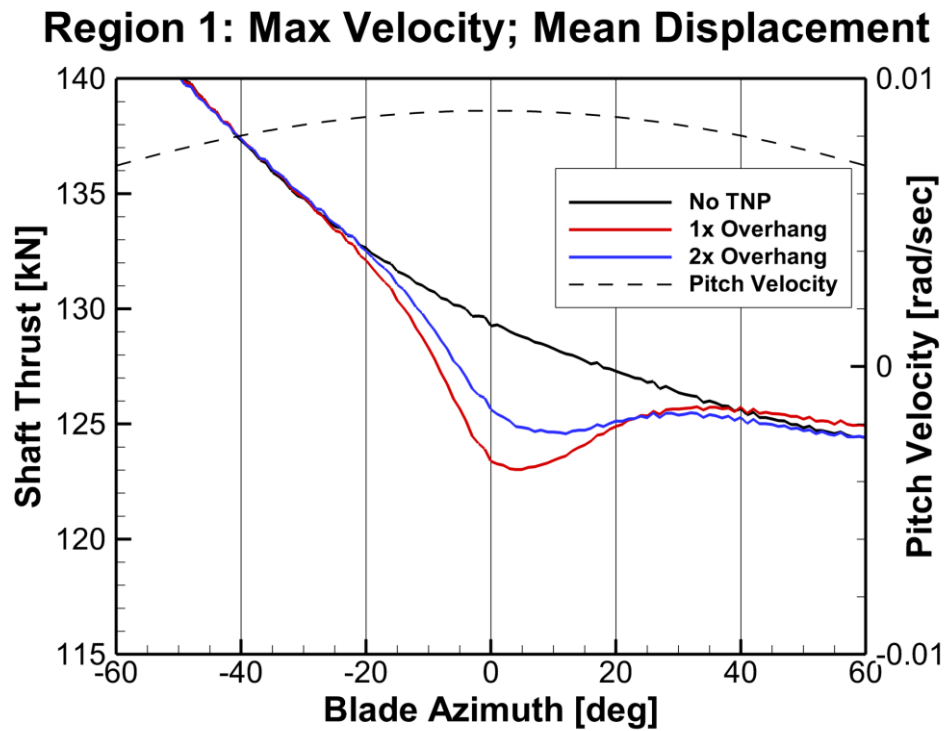


Figure 35 Azimuth vs. shaft thrust for R1

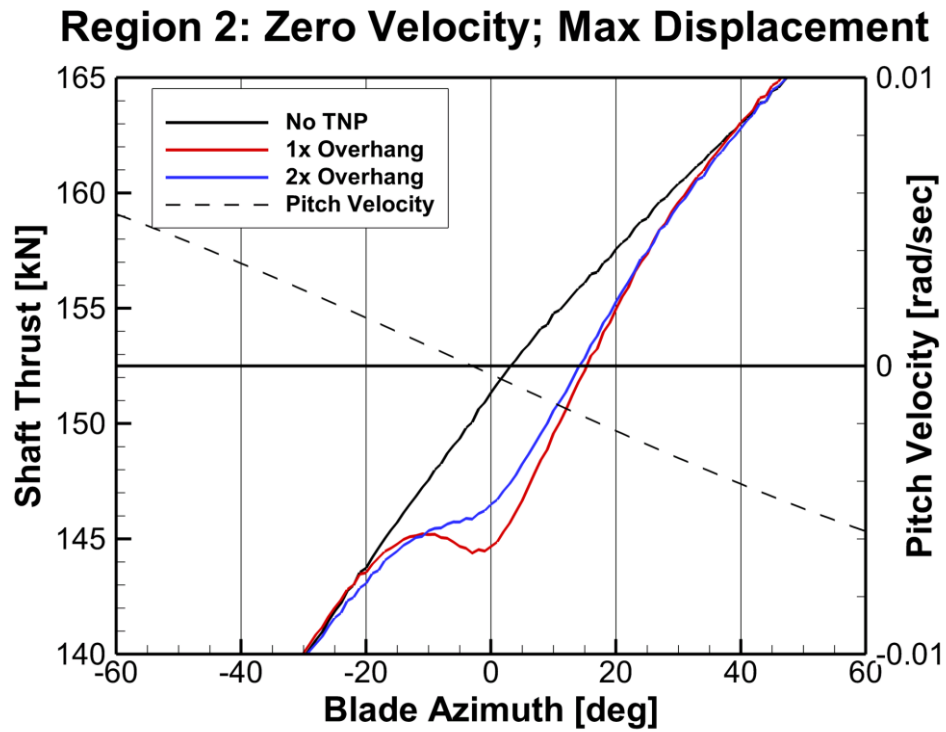


Figure 36 Azimuth vs. shaft thrust for R2

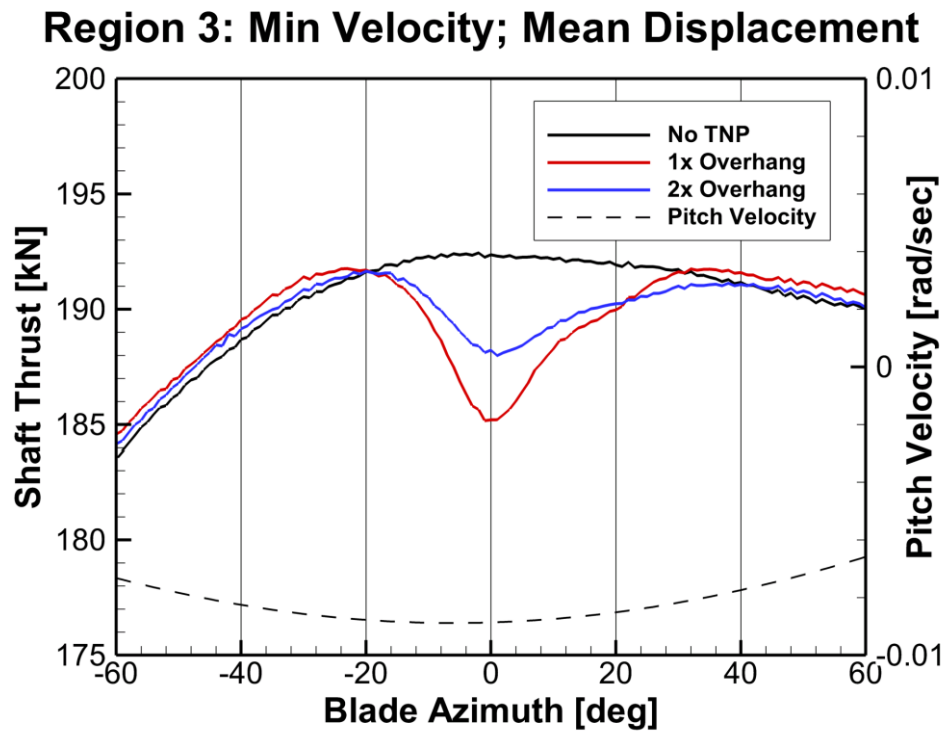


Figure 37 Azimuth vs. shaft thrust for R3

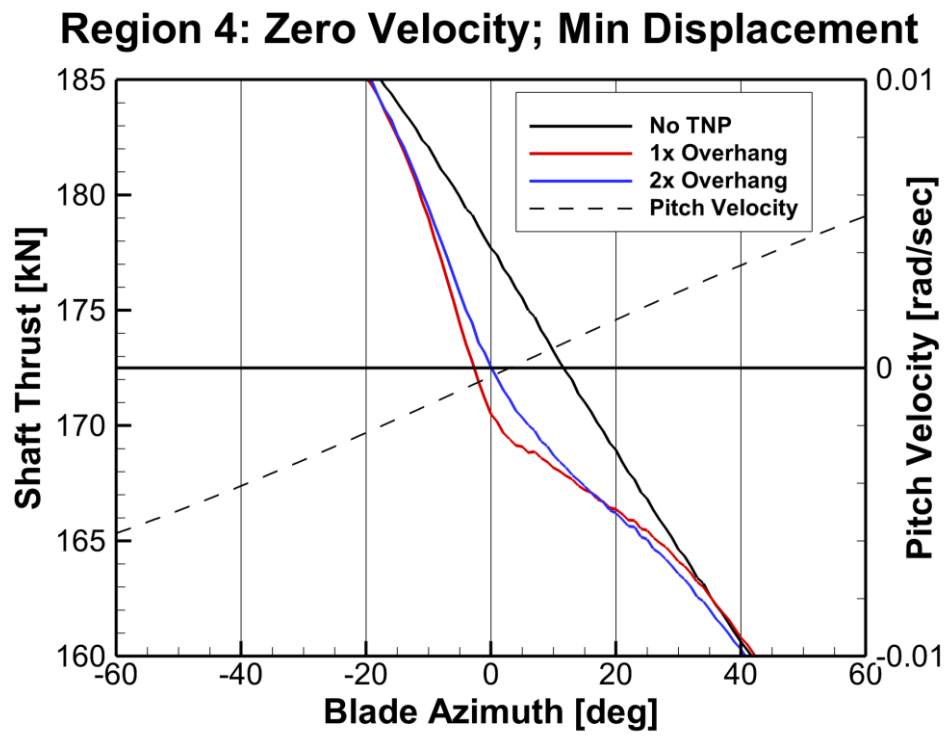


Figure 38 Azimuth vs. shaft thrust for R4

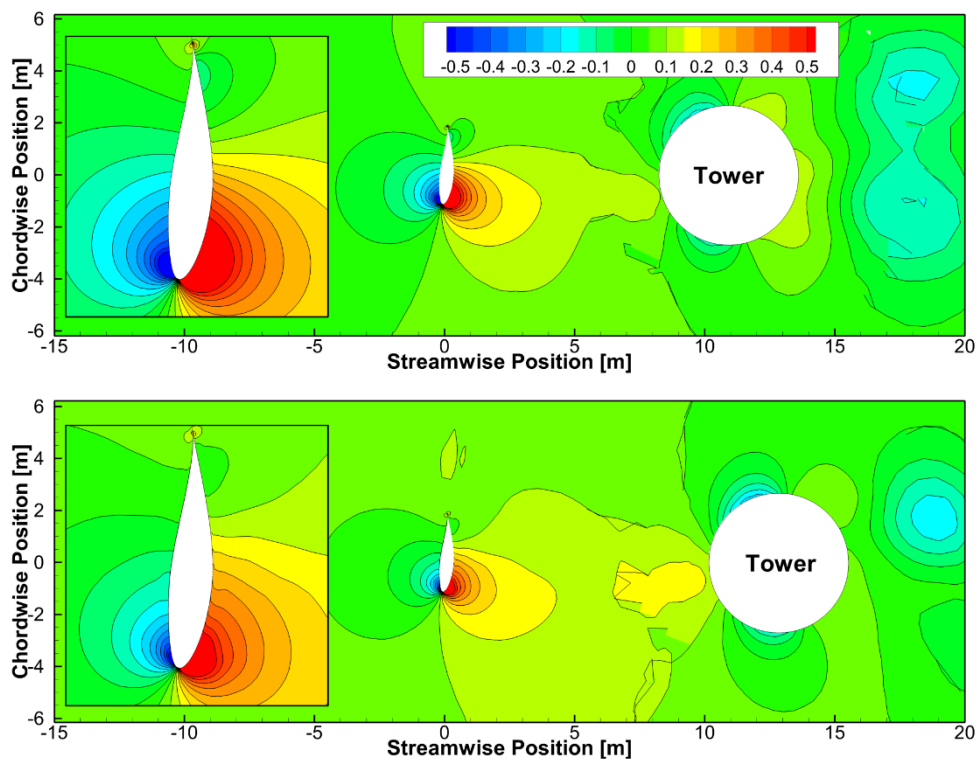
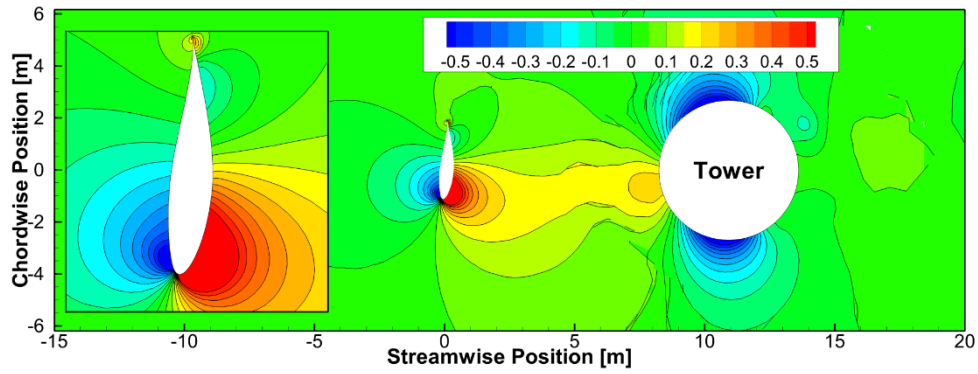
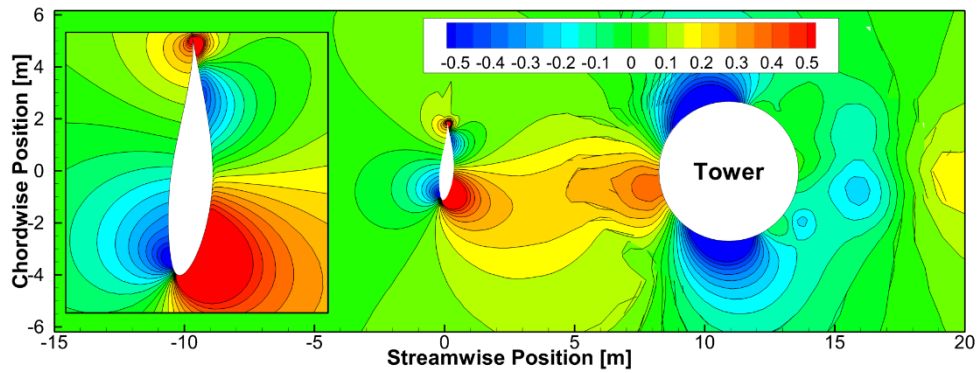
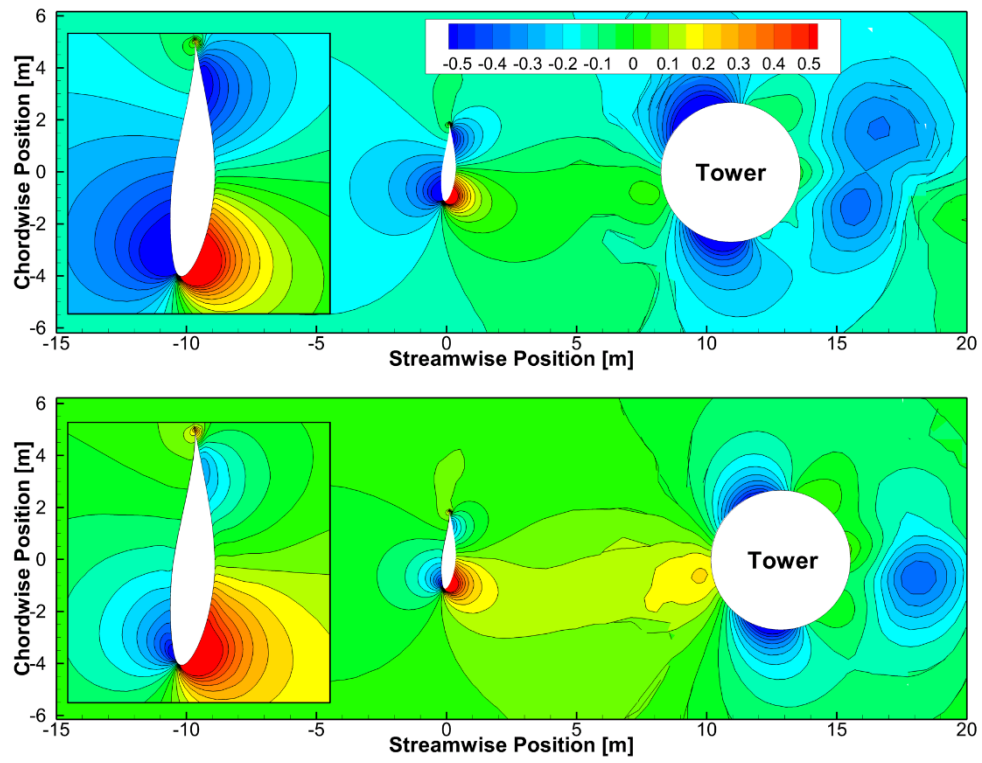


Figure 39 C_p differences for R1

Figure 40 C_p differences for R2Figure 41 C_p differences for R3

Figure 42 C_p differences for R4

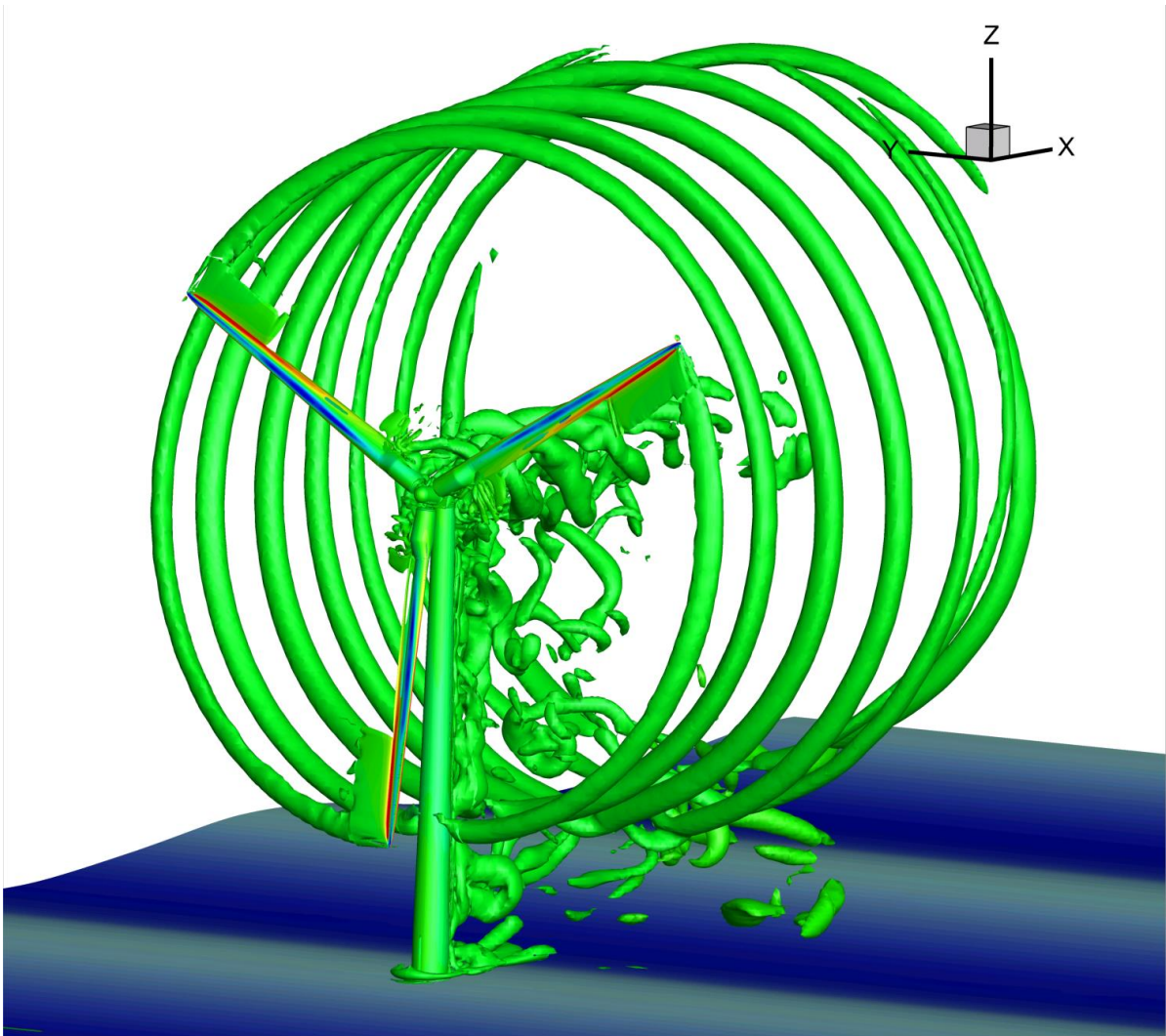


Figure 43 Q-isosurface of 1x simulation in R1 colored by C_p

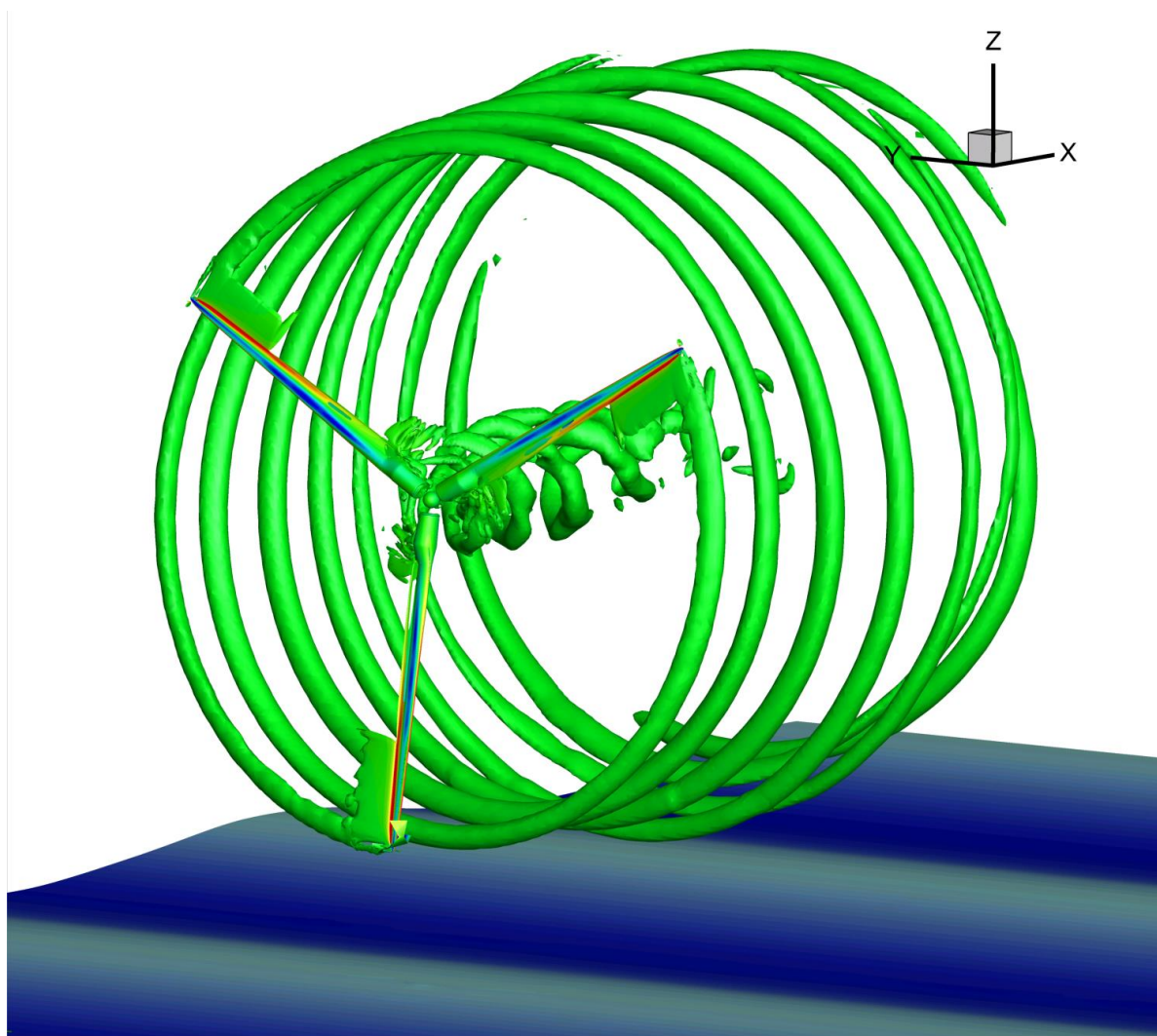


Figure 44 Q-isosurface of no TNP simulation in R1 colored by C_p

5.9 Tables

Table 6 Descriptions of motion regions R1-R4

	R1	R2	R3	R4
Time in wave period [s]	0	2.5	5	7.5
Pitch [deg]	2.75	3.56	2.75	1.94
Surge [m]	-3.635	-3.185	-3.635	-4.085

Table 7 Thrust loss of 1x & 2x simulations compared to No TNP in kN

Case	R1	R2	R3	R4
1x	5.9 (4.6%)	6.7 (4.4%)	7.2 (3.7%)	7.2 (4.1%)
2x	3.6 (2.8%)	4.8 (3.2%)	4.1 (2.2%)	5.2 (2.9%)

CHAPTER 6: CFD SIMULATION OF A FLOATING OFFSHORE WIND TURBINE SYSTEM USING A VARIABLE-SPEED GENERATOR-TORQUE CONTROLLER[§]

6.1 Abstract

Prediction and control of rotor rotational velocity is critical for accurate aerodynamic loading and generator power predictions. In this chapter a variable-speed generator-torque controller (VS) is combined with the code developed in previous chapters. The developed code is utilized in simulations of the OC3-Hywind. Prescribed motion simulations are first performed to determine baseline rotor velocity and developed torque. The OC3's load case 5.1, with regular wave and steady wind excitation, is performed and results are compared to NREL's OC3 results. The developed code is shown to functionally control generator speed and torque but requires controller calibration for maximum power extraction. Generator speed variance is observed to be a function of unsteady streamwise platform motions. The increased mooring forces of the crowfoot model, relative to the AYS model utilized by NREL, are shown to keep the turbine in a more favorable variable-speed control region. The simulations in this chapter predict less overall platform velocities and less aerodynamic torque corresponding to lower rotor rotational velocities and reductions in generated power.

6.2 Introduction

The developed tool is applied to the OC3-Hywind. Simulations of increasing complexity are performed and results are compared with results produced by NREL during the OC3 LC 5.1 results (Jonkman et al., 2010) using FAST. Time histories of predicted platform and rotor motions are analyzed along with predictions of developed and generated power. The effects of platform pitching velocity on blade pressure is examined in pressure coefficient plots.

[§] Submitted to *Renewable Energy*, July 2015

6.3 Mathematical Modeling and Methods

6.3.1 Geometry

Figure 45 shows the three coordinate systems used in this chapter. The earth-fixed system (X, Y, Z) originates at the still water line (SWL). The turbine frame (x_T, y_T, z_T), which translates and rotates with the moving system, originates 120 m vertically upward from the draft of the platform along the centerline of the turbine with the z_T axis pointing upward along the centerline of the platform, the x_T axis pointing from front to back in the circular cross-section of the platform, and the y_T axis pointing to the left when the system is viewed from the front, forming a right-handed orthogonal frame. Note the turbine frame is relocated from chapters 4 and 5 where it corresponded with CG of the system. This frame position is more consistent with the setup used by NREL and provides more direct comparisons. The rotor system (x_R, y_R, z_R) originates at the center of the hub, rotates with the rotor, and includes the blade's cone angle such that the $-z_R$ axis points, at all times, along the pitch axis of blade 1—initially at 0° azimuth and shown directly in front of the tower in Figure 45. The y_R axis points from the leading edge to the trailing edge of blade 1 at 0° blade twist, and the x_R axis forms a right-handed orthogonal coordinate system with the y_R and z_R axes.

6.3.2 Drivetrain Modeling

The drivetrain is modeled as described in the OC3-Hywind reference turbine specification (Jonkman et al., 2009). It is a rigid-structure allowing only for rotation about the rotor central axis. It consists of the rotor, low-speed shaft (LSS), gearbox, high-speed shaft (HSS) and generator as shown in the schematic in Figure 46. The rotor, consisting of the hub and blades, is given a rotational moment of inertia about the low-speed shaft (LSS) of $38,759,232 \text{ kg}\cdot\text{m}^2$. This inertia is calculated with FAST and was verified, through private conversation with Jason Jonkman of NREL, to agree with the figure used by the participants of the OC3. The generator is modeled as having a moment of inertia about the LSS of $5,025,500 \text{ kg}\cdot\text{m}^2$ giving a total moment of inertia about the LSS of $43,784,732 \text{ kg}\cdot\text{m}^2$. The gearbox is given a 97:1 ratio with no modeled internal losses. The inertia and torsional losses of both the LSS and HSS are neglected. The generator of the present study is modeled with the same characteristics as the variable-speed generator used by participants of the

OC3. The generator is rated at 5 MW of electrical power and a speed of 1173.7 RPM, corresponding to a rated rotor velocity of 12.1 RPM. The generator's efficiency is given as 94.4%, such that the rated mechanical power is 5.297 MW and the rated torque is 43,093.55 N-m. The drivetrain properties relevant to the present study are presented in Table 8 and more information about the development of these parameters is available in (Jonkman et al., 2009).

The generator torque transmits to the HSS and couples with the aerodynamic torque developed by the rotor to accelerate or decelerate the rotor according to a rotational equation of motion applied to the LSS:

$$T_{Aero} = N_{Gear}T_{Gen} + I_{Dr}\dot{\Omega} \quad (6.1)$$

where T_{Aero} is the aerodynamic torque developed by the rotor and transmitted to the LSS, N_{Gear} is the gearbox ratio between the HSS and the LSS, T_{Gen} is the generator torque transmitted to the HSS, I_{Dr} is the mass moment of inertia of the drivetrain about the LSS, and $\dot{\Omega}$ is the time rate of change of the rotor velocity, Ω . The present study uses a first-order forward difference approximation of $\dot{\Omega}$ in (6.1) to solve for the rotor velocity:

$$\dot{\Omega} \approx \frac{\Omega^{n+1} - \Omega^n}{\Delta t} \quad (6.2)$$

where Ω^{n+1} is the rotor velocity of the next time step, Ω^n is the current rotor velocity, and Δt is the elapsed time between calculations—represented by the global time step used for simulations in this study. Introducing (6.2) into (6.1) and rearranging provides:

$$\Omega^{n+1} = \frac{\Delta t (T_{Aero}^n - N_{Gear}T_{Gen}^n)}{I_{Dr}} + \Omega^n \quad (6.3)$$

Equation (6.3) is an explicit expression for Ω^{n+1} requiring the instantaneous aerodynamic and generator torques, T_{Aero}^n and T_{Gen}^n , respectively. CFDSHIP-IOWA integrates pressure and shear stress over the blades and hub to calculate T_{Aero}^n about the LSS. The VS controller module is called to determine T_{Gen}^n , described in the following section. After T_{Gen}^n is

determined, equation (6.3) is solved and the new rotor azimuth angle is linearly extrapolated:

$$\theta^{n+1} = \Omega\Delta t + \theta^n \quad (6.4)$$

6.3.3 Variable-Speed Generator-Torque Controller

The variable-speed generator-torque controller works to maximize generated power below rated rotational velocity. Note that, while traditionally referred to as a variable-speed (VS) controller, the controller actually varies the generator-torque. Details about the internal workings of variable-speed generators can be found in (Burton, 2011). The VS controller for the OC3-Hywind is developed in (Jonkman et al., 2009, Jonkman, 2010), with the relevant details described here. The generator speed is first filtered, using a single-pole low-pass filter with exponential smoothing (Smith, 1997) to avoid high-frequency excitation of the control systems. The filter coefficient, α , is defined as:

$$\alpha = e^{-2\pi f_c \Delta t} \quad (6.5)$$

where f_c is the corner frequency of the filter and Δt is the time step. The filtering equation is then:

$$\omega_F^n = (1 - \alpha)\omega^n + \alpha\omega_F^{n-1} \quad (6.6)$$

where ω_F^n is the current filtered generator speed, ω^n is the current, unfiltered generator speed, and ω_F^{n-1} is the filtered generator speed of the previous time step. For each time step equation (6.6) is solved and the current filtered generator speed is then used as the exclusive input for the torque controller. The torque provided by the generator is calculated from a piecewise function of RPM based on 5 speed control regions: 1, 1-1/2, 2, 2-1/2, and 3, visualized in Figure 47 and tabulated in Table 9. The optimal line in Figure 47 represents the optimum constant tip-speed ratio, defined as blade tip speed divided by incoming wind velocity, that the VS controller is attempting to maintain while in operation below rated rotor rotational velocity. In region 1 the rotational velocity of the rotor is below the cut-in velocity, the generator torque is set to zero (i.e. no power is extracted), and the aerodynamic torque developed by the rotor blades is used to accelerate the rotor toward cut-in. In region

1-1/2 the generator torque ramps linearly with generator speed. This region serves as a transition between the optimal generator torque curve and the cut-in generator speed to provide a lower limit for operational range. In region 2 the VS controller sets the generator torque for optimal power generation. Region 2-1/2 is another linear ramp used to limit tip speed at rated power for noise concerns. In region 3, above rated generator speed, the torque is held constant at rated.

6.3.4 Numerical Methods and Solution Strategy

In the simulations in this chapter the momentum convection terms are discretized using a fourth-order upwind differencing scheme, an upgrade from the second-order accuracy scheme used in previous chapters thanks to upgraded computational resources obtained later during this dissertation's development. The level-set convection terms are discretized using the same fourth-order hybrid scheme described in section 5.3.1. A second-order backward differencing scheme is used for temporal discretization in the momentum equation. The overall solution strategy, with the VS controller module included, is shown in Figure 48.

6.4 Simulation Conditions and Design

Three simulations (cases 1-3) are performed for the present study, all of which utilize the conditions from the OC3's load case (LC) 5.1 (Jonkman et al., 2010). LC 5.1 features regular (Airy) incident waves and steady, unidirectional incoming wind at ~70% rated wind velocity. An incremental approach in motion predictions is used for increasing complexity from case 1 to case 3. The exact platform and rotor motions from NREL's OC3 LC 5.1 results are prescribed in case 1. The results of case 1 are compared to those of NREL as a baseline case, examining the developed aerodynamic torque by CFDShip-Iowa given identical motions. The platform motions are similarly prescribed in case 2, however the rotor is released and the VS controller engaged to predict rotor rotational velocity and the corresponding aerodynamic and generator power. In case 3 the system is released and both platform motions and rotor rotational velocity are predicted. The platform is allowed to move downstream and find an equilibrium point where all transient natural frequency driven motions, notably in surge, have decayed to within 2% relative to the mean. A full

comparison of the results of the present method and the motion and power predictions of NREL's FAST is presented. A summary of simulated cases is presented in Table 10.

6.5 Results and Discussion

6.5.1 Overview of Flow Field

Several features key to FOWT wake modelling and simulation are observed in the flow field of the near and far wake, which is visually depicted in Figure 49 a through d. Here a, b, and c present 3-dimensional views of the turbine and Figure 49d shows contours of streamwise velocity at the central vertical cross section of the system. Tip vortices are the dominant feature in Figure 49 a, b, and c, visualized with isosurfaces of the Q-criterion (Hunt et al., 1988). These vortices generate a helical structure as they convect downstream and provide a visual boundary of the rotor wake. Secondary to the tip vortices is the turbulent activity downstream of the tower which combines with vortices shed from the roots of each blade. An abrupt discontinuity in resolution of both Q-isosurfaces and u-velocity contours is seen at the streamwise end of the wake refinement grid. Vertical wake skewing due to platform pitching, platform heaving, and wave height can be seen in the tip vortices of Figure 49 b and c. This corresponds with horizontal stretching and compressing seen in the varying streamwise distance between individual tip vortices. This wake stretching is further compounded in the lower half of the wake as the free-surface, here modeled as a no-slip condition for the wind, is moving 96% faster in the present conditions than the incoming wind with a varying height. This causes oscillating local wind velocities closer to the wave surface, seen in the velocity gradients in Figure 49 d. These variations in velocities produce variations of pressure on the order of those seen in the wake, developing a secondary source of rotation. This secondary rotation will cause the wake to interact with itself, blending tip vortices and producing a situation similar to the vortex ring state described in (Sebastian et al., 2010). This stresses the importance of proper wake modeling for FOWT, which requires calibrated empirical models to account for yawed inflow and unsteadiness in BEM but is intrinsic to CFD solutions. Wake counter-rotation can also be seen in the tower and root vortices of Figure 49 a and b, a result of the chord-wise acceleration of the incoming wind. The substantial drop in streamwise velocity in the wake due to kinetic energy extraction is shown in Figure 49 d. Also visible is the faster moving core wake region, immediately

behind the hub and cylindrical blade roots, where very little energy is extracted from the freestream, and the impinging of the free-surface induced pressure gradients on the lower half of the wake.

6.5.2 Cases 1 and 2

Time-series results of predicted aerodynamic torque, generator power, generator speed, and generator torque in cases 1 and 2 are shown in Figure 50 a and b along with the OC3 LC 5.1 results from NREL. The torque and power details for case 2 are also shown in Table 11. In Figure 50, and in all subsequent time-series plots, any flow and motion transient periods have been removed from results and only the final 30 seconds, corresponding to 3 wave periods, of each result is displayed. The instantaneous wave elevation at the platform centerline is at its maximum at 0, 10, 20, and 30 seconds for all simulations, both present and from NREL.

Aerodynamic torque developed by the rotor was not directly presented in NREL's 5.1 results and was solved for via rearranging equation (6.1):

$$T_{Aero} = I_{Dr} \dot{\Omega} + N_{Gear} T_{Gen} \quad (6.7)$$

The rotor acceleration term of equation (6.7), $\dot{\Omega}$, was also not presented in NREL's results and is approximated with a fourth-order central difference equation given NREL's discrete rotor velocity time history:

$$\dot{\Omega}^n \approx \frac{\Omega^{n-2} - 8\Omega^{n-1} + 8\Omega^{n+1} - \Omega^{n+2}}{12\Delta t} \quad (6.8)$$

The resulting aerodynamic torque plot for NREL in Figure 50a is, accordingly, noisy but clearly displays the mean over time. The pitch velocity, common for all three simulations, is also shown for reference purposes in Figure 50a exhibiting the strong correlation between pitch velocity and aerodynamic torque. A negative pitch velocity, as defined in the earth-fixed frame, is an upwind velocity. The surge velocity is in phase with the pitch velocity and a negative surge velocity also refers to upwind. Thus the developed torque peaks at the maximum upwind velocity and is at a minimum at the maximum downwind velocity. Both cases 1 and 2 are observed to agree strongly with FAST in frequency and phase of all

predictions of torque, generator speed, and power. The minimum aerodynamic torque of cases 1 and 2 agree well with the minimum predicted by NREL, showing only a 4.2% relative difference, likely inflated by the noise in the approximated NREL torque plot. However both cases 1 and 2 predict 10.7% less maximum aerodynamic torque, likely due to more separation being predicted by DDES during upwind pitching in the present study (see, for example, Figure 53 and Figure 54). The noise present in the calculation of NREL's aerodynamic torque is assumed to average out over time giving a mean of 2.07 MN-m. Both cases 1 and 2 give a mean of 1.98 MN-m, 4.3% less than NREL.

In Figure 50b time-series predictions of the generator torque and generator speed of case 2 are presented. The line between VS control regions 1-1/2 and 2 is also drawn. A similar phase shift between generator speed and generator torque, a product of filtering the generator speed in the VS controller, is observed in the present study and NREL's predictions. In Case 2 peak generator torque predicted is 6% less than that of NREL as a result of decreased peak aerodynamic torque discussed previously. The minimum generator torque is predicted in case 2 to be 8% less than that of NREL's results as an effect of excursions of the VS controller into different control region strategies. In region 1-1/2 the generator ramps down to shutoff, linearly dropping torque with RPM. The predicted generator speed of case 2 spends ~33% of each wave period in region 1-1/2 while the predictions of NREL spend ~16% of each wave period producing more substantial torque losses in case 2. Analysis of the generator speed of case 2 shows little effect of the excursion into region 1-1/2 on the generator speed, however. Also observed is the mere 2% less predicted minimum generator speed of case 2 compared to NREL in Figure 50b, corresponding to practically no difference in minimum aerodynamic torque in Figure 50a. These two points suggest that lowering the RPM cutoff line between regions 1-1/2 and 2, mitigating the oscillations between the two regions, could potentially deliver more generator torque with minimal deceleration of the rotor, thereby delivering more generator power for the given conditions. A difference in mean generator torque is thus observed with NREL predicting a mean of 21.3 kN-m and the present study predicting 20.4 kN-m, a relative decrease of 4.2%. The resultant generator power for case 2 is compared to NREL's predictions in Figure 50a. NREL's predicted rotor velocity was prescribed in case 1 such that

the generator power developed is identical between the two simulations. The maximum generator power predicted in case 2 is 2.04 MW, an 8.5% decrease relative to NREL's maximum of 2.23 MW. The minimum generated power in case 2 is 1.48 MW while NREL predicts a minimum of 1.55 MW, representing a 4.5% relative decrease in case 2. These losses in generated power are functions of the reduced generator speed and aerodynamic torque in the present study. The mean power generated in case 2 is 1.76 MW, an 8.8% decrease relative to NREL's mean of 1.93 MW.

6.5.3 Case 3

In case 3 the platform is released and allowed to move freely under wind and wave excitation as described in Table 10. Time-series plots of the predicted platform motions and velocities in surge, pitch, heave, and yaw from case 3 are compared to the predictions of NREL in Figure 51 a through d, respectively, and a summary of minimum, maximum and mean results from both NREL and case 3 is presented in Table 11. In case 3 the maximum predicted platform surge is 13.1 m and the minimum is 10.6 m. These are 13.8% less and 10.9% less than NREL, respectively, and produce a 12.5% reduction in mean surge relative to NREL. These lower predictions are likely due to the increased surge and restoration forces and moments provided by the crowfoot mooring lines compare to the AYS lines used by NREL (see Figure 27 **Error! Reference source not found.**). A relative difference of 13.2% in maximum pitch is seen in case 3 while producing almost identical minimum pitch prediction for an 8% reduction in mean pitch. While the crowfoot mooring model of case 3 also features increased restoration in pitch, the most likely factor for reduced mean pitch is the reduction in rotor thrust associated with the increased drag of separation—assumed to be more readily predicted by DDES in the present study. The aerodynamic drag of the tower is included in the present results and can be seen to be significant in Figure 49d. A minimal phase difference is seen between the heave results of case 3 compared to those of NREL, potentially due to viscous effects in heave being predicted in the present study as well as differences in heave restoration between the different mooring models of the two studies. Large percentage differences are seen in the maximum (225%) and minimum (-10.4%) heave predictions, although these differences, in absolute terms, are a negligible 0.09 m and 0.05 m, respectively. The platform yaw of the present study is seen to be 90° different in

phase relative to NREL while displaying the same frequency. Significant reduction in system yaw is seen in case 3 with the maximum yaw 75.7% less and minimum yaw -65.5% less than the maximum and minimums predicted by NREL. Similar to heave, however, these correspond to negligible absolute values, with a maximum yaw displacement in either study of 0.37° .

The mean velocities of all DOFs are observed to be zero as the system as all transient motions have sufficiently decayed. Large decreases of -35.3% and -30.4% (averaged) are seen in both the upwind and downwind magnitudes of surge and pitch velocity, respectively, relative to NREL's results. These lower velocity magnitudes are attributed to the increased mooring restoration in the present study as well as non-linearities in drag calculations present in the URANS equations solved in case 3. A minimal difference of 0.01 m/s in mean heave velocity is observed and the maximum and minimum yaw velocity differences, 66.7% and 71.4% lower, respectively, are negligible in absolute magnitude.

The time-series predictions of torque and power from case 3 along with NREL's results, identical to those from Figure 50 but repeated for comparison are shown in Figure 52 a and b. Compared with cases 1 and 2, which use NREL's exact OC3 LC 5.1 motions and agree very strongly with NREL in minimum developed torque, the platform motions of case 3 are controlled by the crowfoot mooring model and are subjected to lesser positive (downwind) velocities (see Figure 51a and b and Table 11), which are shown to correspond with minimum aerodynamic torque in Figure 50a. The minimum aerodynamic torque in case 3 is predicted to be 0.37 MN-m more than that of NREL. However the minimum aerodynamic torque is observed to deviate 0.87 MN-m from a mean 1.95 MN-m, 45% relative, compared to a deviation in NREL's results of 1.36 MN-m from a mean 2.07 MN-m, 66% relative. The reader is reminded that the difference equation used to calculate NREL's aerodynamic torque for the present study produces numeric noise, especially at minimum and maximum values where gradients are highest, and that the maximum and minimum values used are subject to this noise. The effect is evident, nonetheless, in Figure 52a where case 3 clearly shows less deviation from the mean in both maximum and minimum aerodynamic torque. The maximum aerodynamic torque developed in case 3 is predicted to deviate 0.90 MN-m, 46% relative, from the mean. NREL predicts a maximum deviation of 1.48 MN-m, 71%

relative, from the mean. The absolute magnitude difference in maximum aerodynamic torque developed in case 3 and the predictions of NREL is a sizable 0.7 MN-m. This difference is attributed to the decreased upwind velocities of case 3 relative to NREL as well as separation caused by the increased effective angle of attack (AoA) experienced during the upwind velocity phase of platform motion. Upwind relative velocity of the platform increases the effective AoA seen by the blade by increasing the magnitude of the incoming wind velocity component, nominally perpendicular to the rotor plane. This in turn generates high magnitude pressure coefficients at the leading edge of the blade but develops strong adverse pressure gradients at the rear, promoting separation. The full span of the suction side of the blade during both maximum downstream and maximum upstream velocities is shown in Figure 53 a and b, respectively, contoured by local C_P . The developed suction pressure is shown to be significantly lower in magnitude during maximum downstream velocity (Figure 53a) than during maximum upstream velocity (Figure 53b) along the entire blade span beyond the root transition region. In both situations a large separation region exists at the trailing edge of the cylindrical root and the transition region between cylinder and blade, as well as similar separation regions at the blade tip. The maximum downstream situation remains attached over the remainder of the span of the blade. In the maximum upstream situation, however, the root separation region spans 7% more of the blade and trailing edge (TE) separation occurs on the outboard 1/3 of the blade, including a large-scale separation bubble at 80% span. In Figure 54 a and b the outboard 20% of blade 1 is shown during maximum downstream velocity and during maximum upstream velocity, respectively. The TE separation of the upstream velocity situation is more clearly visualized in Figure 54b, along with the separation bubble detailed in the inset. The increased AoA during maximum upstream velocity can be seen in the plane-section streamlines of Figure 54b compare to those of Figure 54a, as well as the increased C_P magnitudes on both the suction and pressure sides of the blade. While producing similar mean values, the smaller deviations of aerodynamic torque produce smaller bending moments, notably edge-wise, on the blades and less torsion in the shafts, reducing overall fatigue. This adds to the importance of the mooring system to limit streamwise velocity fluctuations. The mean aerodynamic torque developed in case 3 agrees well with that of NREL's prediction, showing only a -0.12 MN-m decrease (5.8%). The generator speed predicted in case 3 is shown in Figure 50b. The

diminished platform velocities in case 3 are observed to reduce deviations from the mean generator speed compared to that of case 2, and the generator spends only 28% of the wave period in VS control region 1-1/2 instead of the 33% observed in case 2. The maximum generator torque of case 3, also shown in Figure 50b, deviates 1.4 kN-m from a mean of 20.1 kN-m (7.0% relative) and the minimum generator torque deviates 1.8 kN-m from the mean (9.0% relative). These same generator torque deviations are observed in case 2, perhaps more directly comparable to case 3 than NREL's results due to hydrodynamic and aerodynamic solution modeling differences between the present study and NREL's FAST software. In case 2 is predicted a 1.7 kN-m deviation from the mean in maximum generator torque (8.4% relative) and a substantial 2.9 kN-m deviation in minimum generator torque (14.2% relative). The lesser deviations of generator torque in case 3 compared to case 2 help to reduce fatigue along the entire drivetrain. The resultant generator power developed in case 3 is shown in Figure 50a. The maximum power generated in case 3 is 1.95 MW, which is 12.6% less than the maximum of 2.23 MW generated by NREL and 4.4% less than the 2.04 MW maximum generated in case 2. The minimum power generated in case 3 is 1.55 MW, which is 5.5% less than the minimum 1.64 MW predicted by NREL and 4.5% greater than the 1.48 MW minimum predicted in case 2. The difference between the minimum generator powers in case 3 and case 2 is largely a function of the smaller amount of time spent in VS control region 1-1/2 in case 3 compared to case 2. The mean power generated in case 3 is 1.77 MW, which is 8.3% less than the predicted mean power by NREL. The mean generated power of case 3 is 0.01 MW higher than that of case 2. While this difference is relatively negligible it suggests that minimizing platform velocities, thereby reducing generator speed deviation, can help with more precise controller design.

6.6 Conclusions

An inertial rotor model with a VS generator-torque controller is coupled with high resolution CFD and a mooring force model to predict motion and generated power of FOWT. The developed code is utilized in three simulations of the OC3-Hywind FOWT using the OC3's LC 5.1 wind and wave conditions and results compared to the publically available OC3 LC 5.1 results of NREL. Simulations utilize an incremental approach for verification of the method. The predicted platform motions and rotor rotational velocity of NREL's results are

first prescribed in a simulation (case 1) to determine a baseline expected aerodynamic torque considering the different aerodynamic solution differences between CFD and NREL's FAST. The results agree well with NREL's predictions in both phase and minimum aerodynamic torque but show an 11% reduction in maximum aerodynamic torque attributed to separation being predicted by DDES in the present study.

NREL's OC3 LC 5.1 predicted motions are again prescribed in a second simulation (case 2) where the inertial rotor model and VS controller are activated and rotor rotational velocity is predicted. The results of case 2 serve to identify the effect of the aerodynamic solution differences between CFD and FAST on generator torque and power predictions. The generator speed results of case 2 agree within to 3% of NREL's generator speed predictions, corresponding to very similar aerodynamic torque predictions between case 1 and case 2. The generator speed of case 2 is observed to spend 17% more time per wave period in a lower VS control region than NREL, and minimum generator torque predictions of case 2 are observed to be 8.3% lower than those of NREL as a result. Mean generated power is predicted 8.8% below the mean of NREL's predicted power due to the decreases in both maximum aerodynamic torque and minimum generator torque. The results of case 2 suggest a recalibration of the VS control region cutoffs to help keep generator speed up and increase overall generator power developed.

A final simulation (case 3) is performed where the platform motions and rotor rotational velocity are predicted. The inertial rotor model and VS controller are active and both aerodynamic and hydrodynamic loading is considered. Reductions in mean surge translation and mean pitch relative to NREL's predictions are observed due to increased mooring forces. A 32.7% reduction in maximum platform surging velocity and a 31.4% reduction in maximum platform pitching velocity are also observed. These correspond to reduced upstream and downstream velocities and are shown to keep the generator speed in a more favorable VS control region, and generated power is slightly increased (0.01 MW) from case 2 despite a 1.5% reduction in mean aerodynamic torque. Separation over the outboard 1/3 of the blade is predicted during maximum upstream pitching velocity, verifying the importance of stabilization of the platform.

6.7 Figures

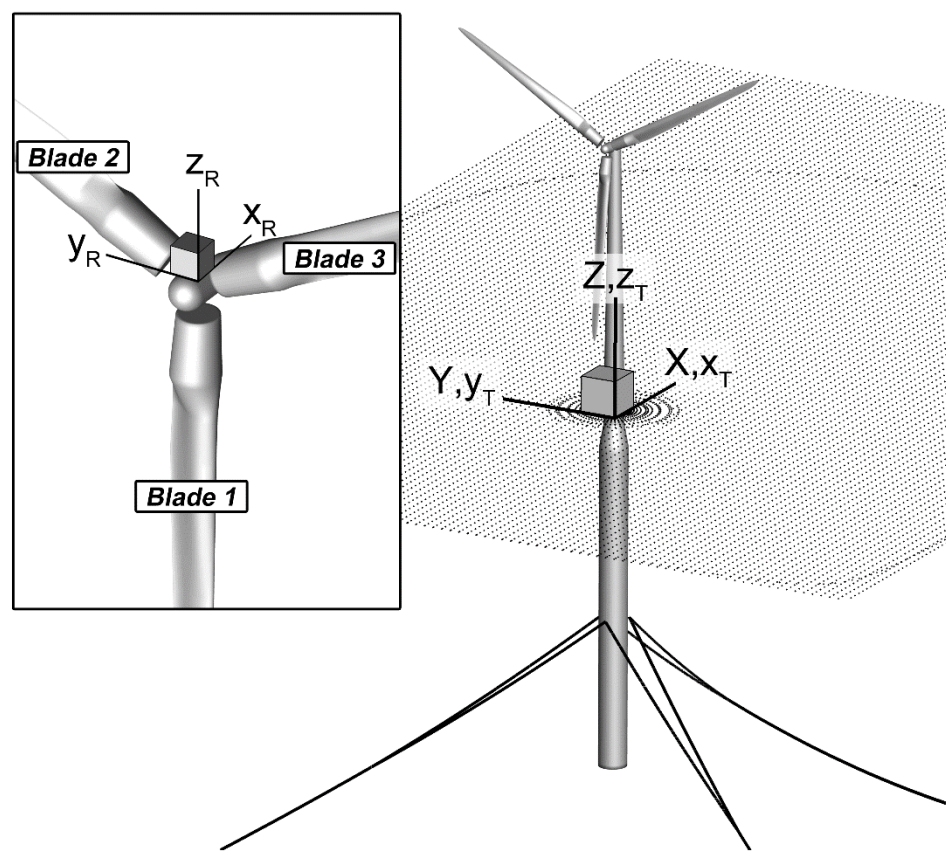


Figure 45 Three coordinate systems: earth-fixed frame (X, Y, Z), turbine system frame (x_T, y_T, z_T), and rotor system (x_R, y_R, z_R)

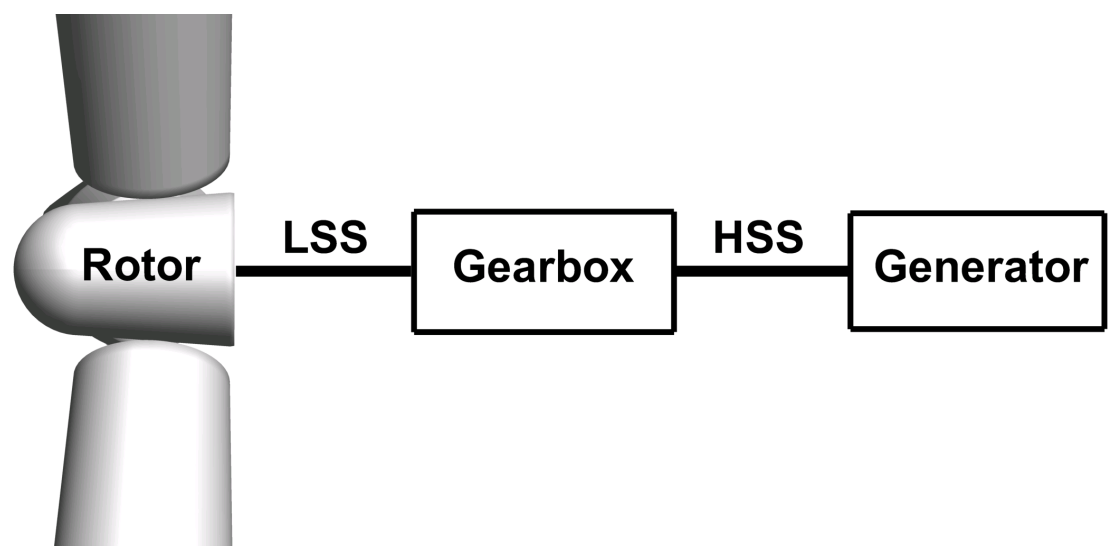


Figure 46 Drivetrain schematic

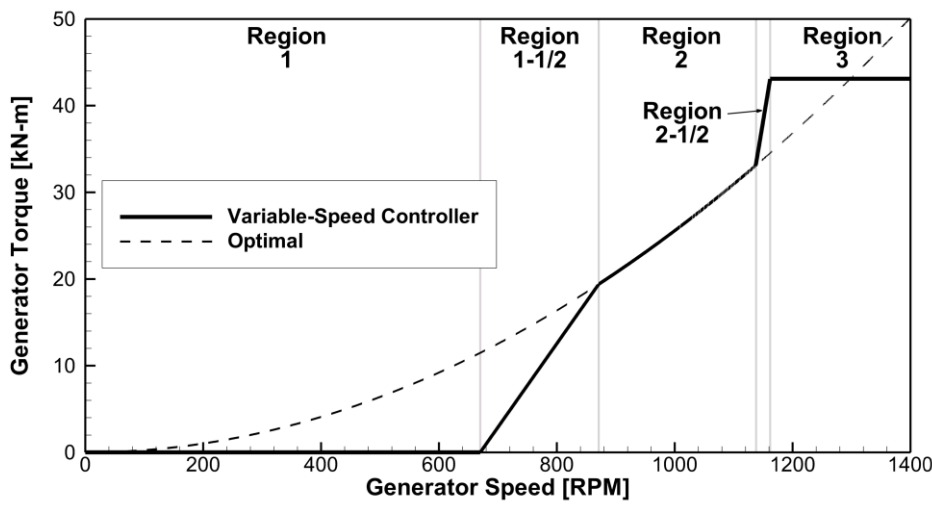


Figure 47 Generator torque vs. generator speed response of the variable-speed controller (Reproduced from (Jonkman, 2009) with edits from (Jonkman, 2010))

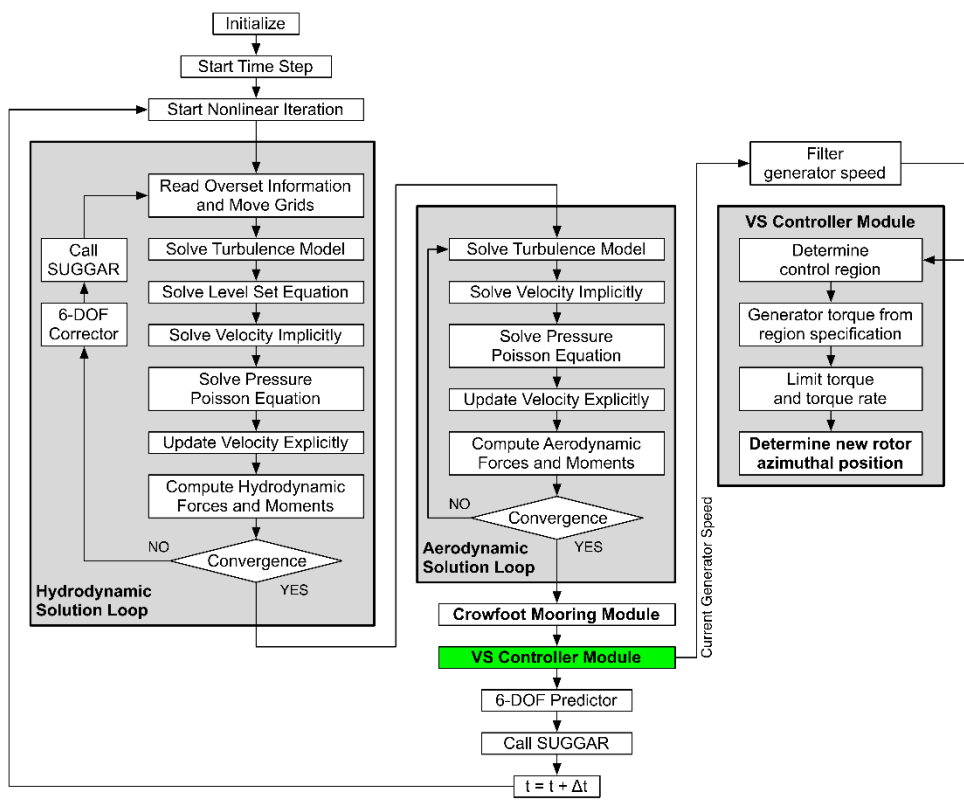


Figure 48 Solution strategy including VS controller module

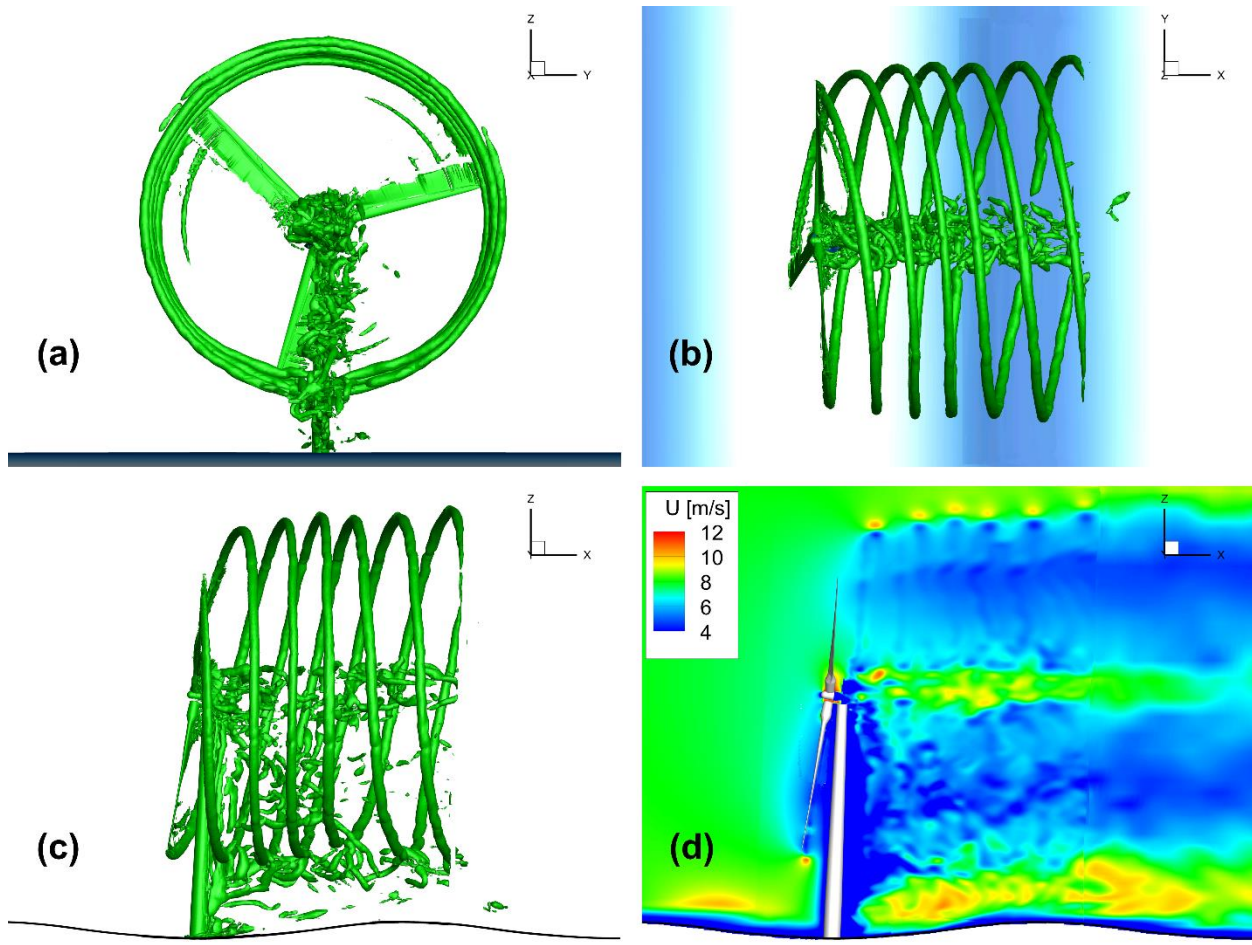


Figure 49 3D views of turbine and $Q=1$ isosurfaces in (a), (b), (c)
(d) Streamwise velocity contours

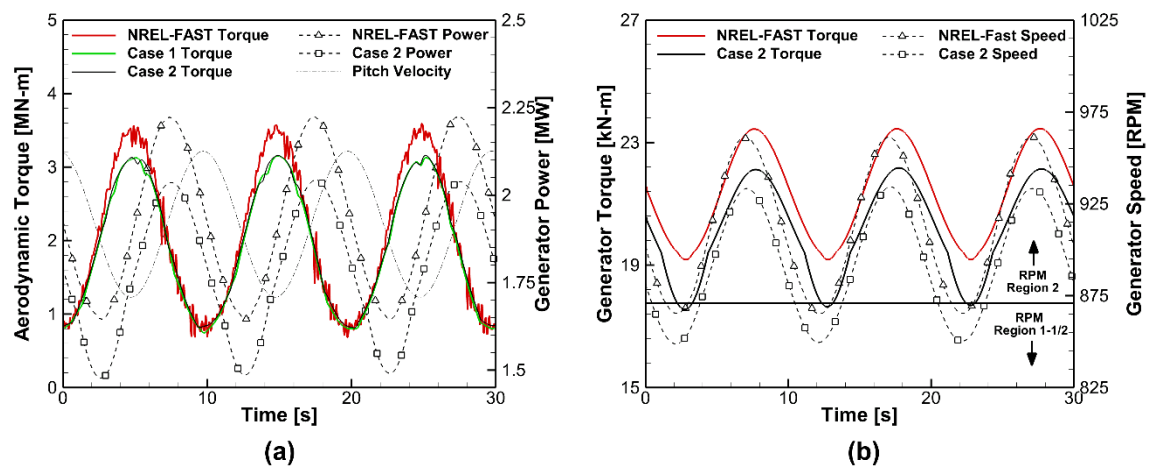


Figure 50 Comparison of torque and speed predictions of case 1, case 2, and NREL-FAST

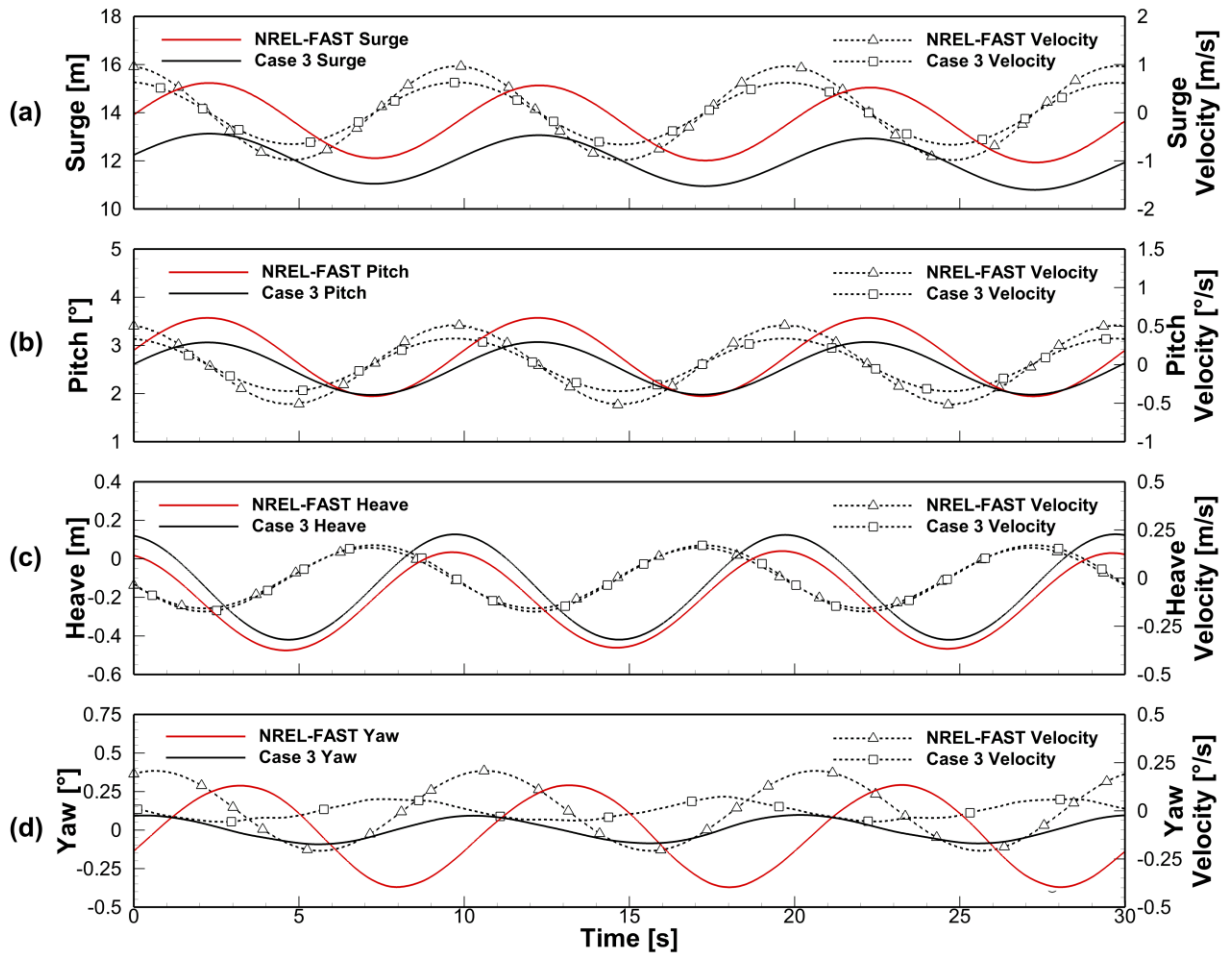


Figure 51 Comparison of platform motions between case 3 and NREL-FAST

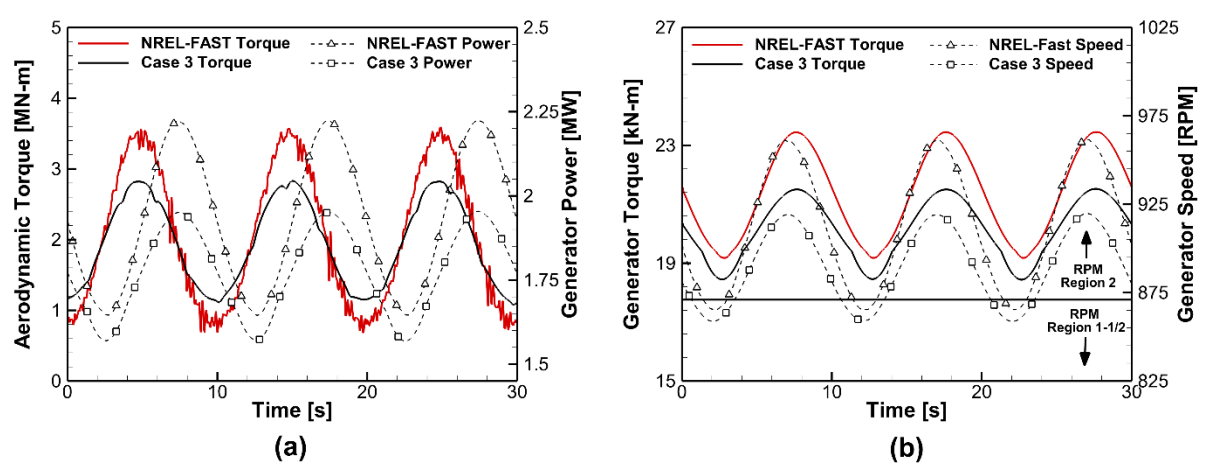


Figure 52 Comparisons of aerodynamic torque and generator predictions between case 3 and NREL-FAST

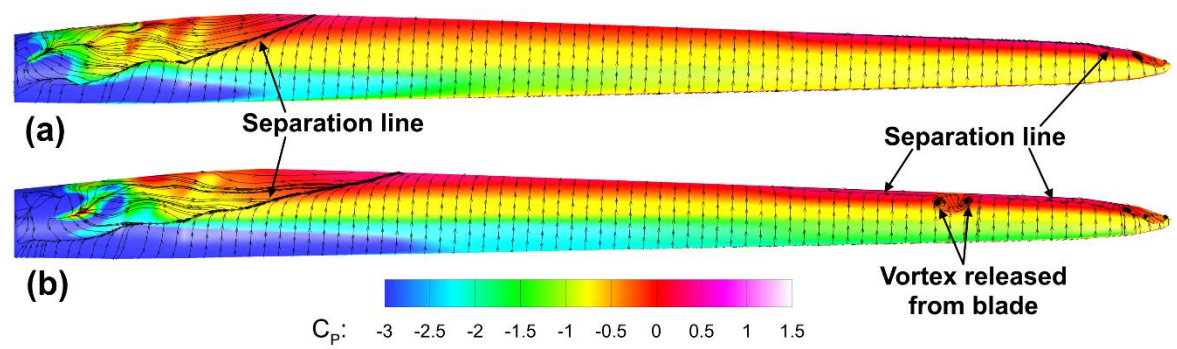


Figure 53 Limiting streamlines on suction side of blade, colored by C_p . (a) Maximum downstream platform velocity; (b) Maximum upstream velocity

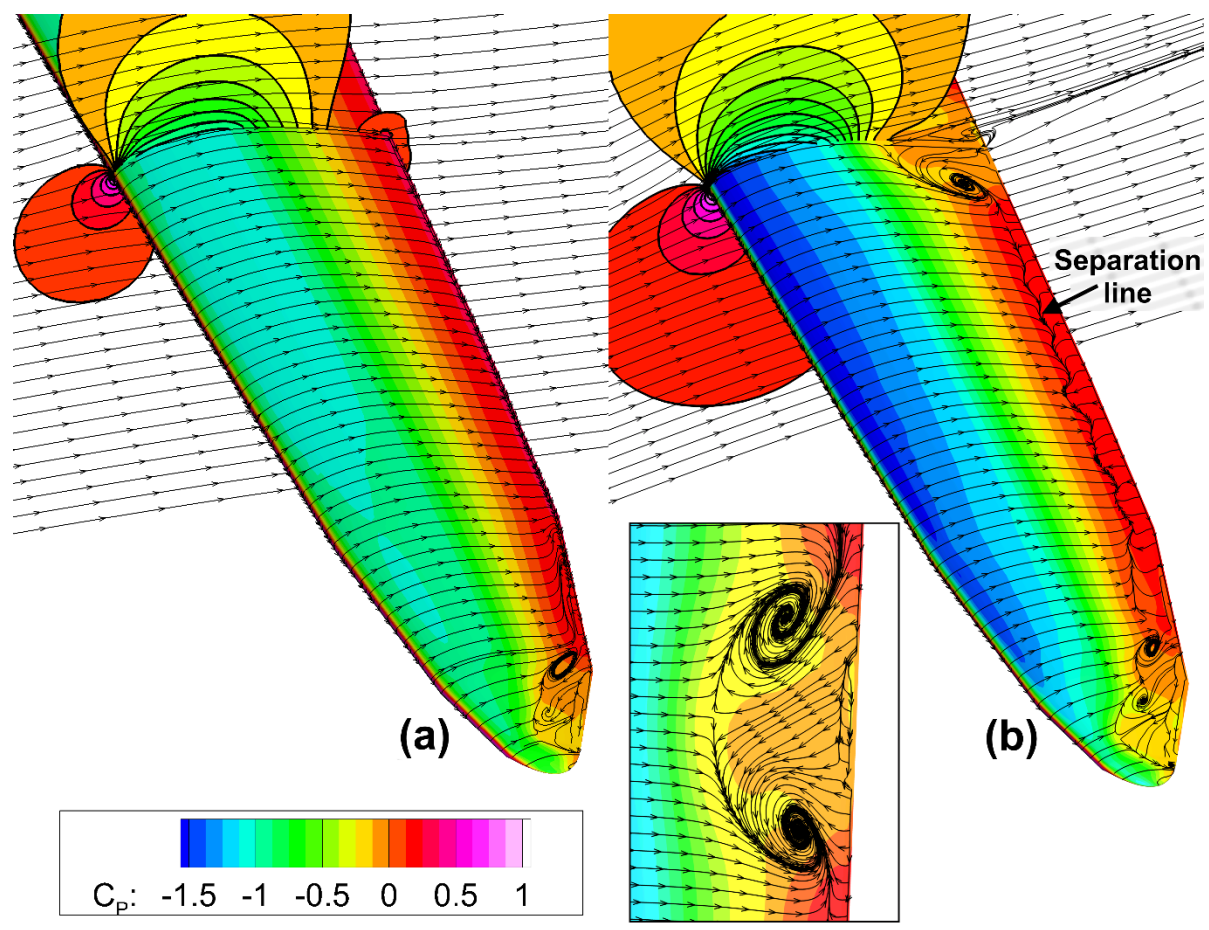


Figure 54 Outboard 20% of blade showing limiting streamlines and colored by C_p . (a) Maximum downstream platform velocity; (b) Maximum upstream velocity. Inset shows detail of separation zone at 82% blade span.

6.8 Tables

Table 8. Drivetrain Properties

Rotational inertia about LSS	43,784,732 kg-m ²
Gearbox ratio	97:1
Rated rotor velocity	12.1 RPM
Rated generator velocity	1173.7 RPM
Generator efficiency	94.4%
Rated generator power	5 MW
Rated generator torque	43,093.55 N-m

Table 9. VS controller control regions with corresponding generator and rotor speeds

Control Region	Generator Speed [RPM]	Rotor Speed [RPM]
1	<670	<6.9
1-1/2	670 - 871	6.9 – 9.0
2	871 - 1138	9.0 – 11.7
2-1/2	1138 - 1173	11.7 – 12.1
3	>1173	>12.1

Table 10. Simulation case matrix

Case	Platform Motions	Rotor Rotation	Simulation Length [s]	Wind Conditions	Wave Conditions
1	Prescribed	Prescribed	120 s	Steady, unidirectional	Regular (Airy) waves:
2	Prescribed	Predicted	120 s		H = 6 m
3	Predicted	Predicted	887 s	8 m/s	T = 10 s

Table 11 Comparison of motions and power characteristics between case 2, case 3, and NREL

	Aerodynamic Torque [MN-m]			Generator Speed [RPM]			Generator Torque [kN-m]			Generator Power [MW]		
	Min	Max	Mean	Min	Max	Mean	Min	Max	Mean	Min	Max	Mean
NREL	0.71	3.55	2.07	865	962	913	19.2	23.5	21.3	1.64	2.23	1.93
Case 2	0.74	3.17	1.98	849	934	893	17.6	22.2	20.5	1.48	2.04	1.76
Difference	0.03	-0.38	-0.09	-16	-28	-20	-1.6	-1.3	-0.8	-0.16	-0.19	-0.17
Relative %	4.2%	-10.7%	-4.3%	-1.8%	-2.9%	-2.2%	-8.3%	-5.5%	-3.8%	-9.8%	-8.5%	-8.8%
	Surge [m]			Pitch [°]			Heave [m]			Yaw [°]		
	Min	Max	Mean	Min	Max	Mean	Min	Max	Mean	Min	Max	Mean
NREL	11.9	15.2	13.6	1.93	3.57	2.75	-0.48	0.04	-0.22	-0.37	0.29	-0.03
Case 3	10.6	13.1	11.9	1.95	3.10	2.53	-0.43	0.13	-0.15	-0.09	0.10	0.01
Difference	-1.3	-2.1	-1.7	0.02	-0.47	-0.22	0.05	0.09	0.07	0.28	-0.19	0.04
Relative %	-10.9%	-13.8%	-12.5%	1.0%	-13.2%	-8.0%	-10.4%	225.0%	-31.8%	-75.7%	-65.5%	-133.3%
	Surge Velocity [m/s]			Pitch Velocity [°/s]			Heave Velocity [m/s]			Yaw Velocity [°/s]		
	Min	Max	Mean	Min	Max	Mean	Min	Max	Mean	Min	Max	Mean
NREL	-0.98	0.98	0.00	-0.51	0.51	0.00	-0.16	0.16	0.00	-0.21	0.21	0.00
Case 3	-0.66	0.66	0.00	-0.36	0.35	0.00	-0.17	0.17	0.00	-0.06	0.07	0.00
Difference	0.32	-0.32	0.00	0.15	-0.16	0.00	-0.01	0.01	0.00	0.15	-0.14	0.00
Relative %	-32.7%	-32.7%	0.0%	-29.4%	-31.4%	0.0%	6.3%	6.3%	0.0%	-71.4%	-66.7%	0.0%
	Aerodynamic Torque [MN-m]			Generator Speed [RPM]			Generator Torque [kN-m]			Generator Power [MW]		
	Min	Max	Mean	Min	Max	Mean	Min	Max	Mean	Min	Max	Mean
NREL	0.71	3.55	2.07	865	962	913	19.2	23.5	21.3	1.64	2.23	1.93
Case 3	1.08	2.85	1.95	857	919	888	18.3	21.5	20.1	1.55	1.95	1.77
Difference	0.37	-0.7	-0.12	-8	-43	-25	-0.9	-2.0	-1.2	-0.09	-0.28	-0.16
Relative %	52.1%	-19.7%	-5.8%	-0.9%	-4.5%	-2.7%	-4.7%	-8.5%	-5.6%	-5.5%	-12.6%	-8.3%

CHAPTER 7: CFD SIMULATION OF A FLOATING OFFSHORE WIND TURBINE SYSTEM EXPERIENCING IRREGULAR WAVES AND INCOMING WIND TURBULENCE**

7.1 Abstract

Blade-pitch control is widely used for onshore wind turbine applications to avoid generator overload during high incoming wind velocities. Floating offshore wind turbines, however, experience platform motions due to wave excitation that lead to unsteady inflow conditions at the rotor that must also be accounted for by the blade-pitch controller. Accurate prediction of coupled aerodynamic and hydrodynamic loading is critical for floating offshore wind turbine controller design and analysis. In this chapter a collective blade-pitch controller is combined with two-phase overset CFD, a variable-speed generator-torque controller, a mooring model, and a wind turbulence model into a comprehensive simulation code for coupled platform motion and generator performance predictions. Three cases from the OC3 are simulated and results compared to those of NREL. A hydrodynamics loading only case is first presented followed by an aerodynamics only case to examine each fluid phase individually. The code is then used to simulate OC3 load case 5.2, which features JONSWAP irregular waves and the Mann wind turbulence model. Results are shown to agree well with NREL in predicted generator torque and power. The results predict significant reductions in platform motion deviations and blade-pitch actuation due to increased mooring forces and diminished incoming wind fluctuations. Further developments based on the present results are also discussed.

7.2 Introduction

Design for FOWT presents significant challenges, however. Aerodynamic and hydrodynamic loading predictions must be coupled with motion predictions and mooring and control models for reliable results. The importance of mooring and VS control models are discussed in sections 4.2 and 6.2, respectively. Mooring lines are required for any FOWT simulation and VS control allows for optimal power extraction during rotor

**Development and results to be submitted to Renewable Energy Journal

rotational speeds between the minimum cut-in speed and the rated rotor speed. For conditions at or beyond rated conditions requires control to prevent generator overload and blade structural protection. Multiple protection control schemes are in service today—for an exposition see (Burton, 2011). One of the most common methods of overload control in utility-scale turbines is collective blade-pitch (BP) control, where the blades are each pitched a "collective" angle, decreasing the effective angle of attack to reduce aerodynamic torque delivered to the LSS. BP control has been successfully employed in onshore applications but has an inherent frequency compromise, and its usage requires a balance of desired optimization and protection characteristics. A BP controller frequency set too low is ineffective at reducing torque and poses risks of generator overload. A controller frequency set too high, however, poses a structural risk to the tower by presenting a "negative damping" situation (Skaare et al., 2007). In this scenario an increase in wind velocity, corresponding with an increase in rotor thrust, produces fore-aft tower bending along its instantaneous side-side axis. This velocity increase also actuates the BP controller and increases the blade pitch angle, which reduces the rotor thrust. During the upwind stroke of the tower vibration, however, the BP controller reduces the blade pitch angle and thereby increases thrust. This high-frequency controller excitation can intensify tower bending and produce structural failure. The negative damping problem is mitigated in onshore controllers by setting the controller response frequency to a value lower than that of the first tower bending frequency, the lowest structural frequency of concern on a fixed-base turbine and typically ~ 0.5 Hz (Larsen et al., 2007b). The controller frequency is then set to ~ 0.1 Hz, slow enough to avoid resonant excitation but fast enough to provide acceptable aerodynamic and generator performance. Floating platforms, on the other hand, are designed with low-frequency oceanic wave excitation in mind and have rigid-body motion frequencies lower than the expected wave frequency range to avoid wave-induced structural vibrations. The surge rigid-body translation natural frequency of the model in the present study, as an example is, 0.00939 Hz (see section 4.5.1). This problem is compounded by the fact that the wind contains more energy around the low surge and pitch (0.034 Hz) frequencies than around the first bending mode of a fixed-base turbine. (Skaare et al., 2007). This makes the aforementioned controller frequency compromise much more important, and this compromise is at the heart of current FOWT BP controller design. The negative-damping

problem associated with high-frequency BP control was first discussed in (Skaare et al., 2007) where the authors combined BEM and a BP control scheme that hid the unsteady platform motions from the controller and estimated the incoming wind velocity based on load monitoring. The result was a reduction of the negative damping effect which significantly increased fatigue life of both tower and rotor components. This was coupled, however, with a reduction of mean generated power and an increase of deviation in both rotor rotational speed and power output. The same team tested several controller frequencies in (Larsen et al., 2007b) to observe responses at each and optimize the compromise required. They observed a similar increase in rotor speed deviations with lower controller frequencies. They also observed that a constant-power generator scheme in VS controller region 3 can add to the negative-damping problem and suggested a change in region 3 from constant power to constant torque to help limit them. A blade pitch-to-stall scheme (trailing edge pitched toward upstream), produced by accident in their study rather than their desired pitch-to-feather scheme (trailing edge pitched toward downstream) during a simulation, was also discussed for potential BP control. The results of this accidental simulation portrayed a pitch-to-stall scheme as quite effective in reducing both power and platform motion fluctuations from mean values. In (Jonkman et al., 2008) the authors applied a gain-scheduled proportional-integral (GSPI) controller to a barge platform, which has a lower pitch moment-of-inertia relative to the spar-buoy platform studied here. They found that neither accounting for tower-top acceleration nor switching from a pitch-to-feather scheme to a pitch-to-stall scheme as suggested by (Larsen et al., 2007b) was effective in reducing the negative-damping in the barge platform and suggested a multiple-input multiple-output state-space (MIMOSS) controller. This GSPI pitch-to-feather controller was tuned and applied to the OC3-Hywind in (Jonkman et al., 2009), and is the controller used herein.

The present controller and turbine/platform combinations have been studied in several works since the conclusion of the OC3. The authors of (Namik et al., 2010) followed the suggestion of Jonkman and compared the use of individual BP control using a MIMOSS controller to that of the GSPI controller applied to the barge platform of (Jonkman et al., 2008). The state-space controller was shown reduce each of power fluctuations and platform

pitching rate by 43% but at a cost of a dramatically increased (~400%) blade pitching rate, which produces stress on actuators and hub mounts, as well as being susceptible to dynamic stall (Larsen et al., 2007a). This controller scheme was then simplified (in terms of inputs) in (Christiansen et al., 2011) and applied it to the OC3-Hywind with a spar-buoy platform for comparison with the baseline control module used herein. The results also showed, similar to (Namik et al., 2010), decreases of 24% in deviations of generator power and speed as well as a 19% decrease in platform pitching. However this was also coupled with a 392% increase in blade pitch rate. This same team studied a new method of control in (Christiansen et al., 2012). They point out that multiple combinations tip speed ratio and blade-pitch angle can combine to produce an optimum power coefficient. They suggest an increasing generator torque combined with additional blade-pitch beyond rated speed to simultaneously slow the rotor and reduce rotor thrust, both reducing structural loading on key drivetrain components. They again found mixed results as platform pitching and power fluctuations were well mitigated but significant increases in platform roll and drivetrain torsion were observed as the blade pitch required in their scheme was 53% higher, producing a larger out-of-plane projection of the blades. Important points regarding BP control are presented in (Lackner, 2013) where the author developed a model which varied the BP controller set-point generator speed based on platform pitch velocity rather than the fixed set-point used in previous controllers. Lackner argues that the compromise faced by FOWT controller designers should be weighted toward mitigation of platform motions and the corresponding structural loading. He points out that offshore components need to be light, requiring reduced loading, and that floating wind turbines will not be standalone machines—the power variability of an individual turbine would be less significant than that of the overall farm variability.

It is clear that FOWT controller design is an active area of research and that future investigations will require proper loading predictions to determine the effectiveness of designs under various environmental conditions. In this chapter a BP controller is combined with the CFD based simulation code utilized in chapters 4 through 6, to allow for simulations above rated wind speeds and investigation into the FOWT BP controller compromise. OC3 load cases 2.2 (wind only; "case 1"), 4.2 (waves only; "case 2"), and 5.2

(combined wind and wave excitation; "case 3") are chosen for an increasing complexity approach. Time-domain results are transformed to the frequency domain and power spectral densities (PSD) and statistics compared to those of NREL's OC3 results. To the author's knowledge a CFD-based model of this complexity has not previously been used.

7.3 Mathematical Modeling

7.3.1 Blade-Pitch Controller

The BP controller implemented into the present code is a GSPI controller developed for the NREL offshore reference turbine in (Jonkman et al., 2009) and modified to help avoid negative damping in (Jonkman, 2010). In a PI controller the desired output, here blade pitch, is determined as a function of two components: a term based on current error (proportional) and a term based on accumulated error (integral). The reader is referred to (Sung et al., 2009) for an excellent overview of PI controller schemes and to (Hansen et al., 2005) for the details regarding derivation of the individual gain coefficients calculated in (Jonkman et al., 2009), which are used in the present study. The relevant details of implantation and solution are presented here. The modified overall solution strategy including the BP controller module is shown in Figure 55. The overall purpose of the BP controller module is to determine the new blade pitch angle for the next time step. During each time step the current filtered generator speed, ω_F^n , and blade pitch, ϕ^n , values (user inputs for the initial time step) are provided to the BP controller. The filtered generator speed ω_F^n , calculated in equation (6.6), is first used to calculate the generator speed error, ω_E :

$$\omega_E = \omega_F^n - \omega_0 \quad (7.1)$$

where ω_0 is the rated generator speed, 122.9 rad/s in the present study. The current blade pitch value is then used to determine a gain-scheduled correction factor:

$$GK = \frac{1}{1 + \frac{\phi^n}{\phi_K}} \quad (7.2)$$

where $\phi_k = 0.1099965$ rad. The speed error and correction factor are then combined to determine the proportional gain term, ϕ_p :

$$\phi_p = K_p \cdot \omega_E \cdot GK \quad (7.3)$$

where $K_p = 0.006275604$ s. The current study uses the proportional gain coefficient from (Jonkman, 2010), where the VS and BP controllers were modified from the original OC3-Hywind controllers in (Jonkman et al., 2009) to slow controller response and mitigate negative damping. The speed error is then integrated (linearly) over the elapsed time since the previous time step, Δt , and added to the integrated speed error, $\bar{\omega}_E^n$, which is logged over the duration of the simulation by the controller module:

$$\bar{\omega}_E^n = \bar{\omega}_E^{n-1} + \omega_E \Delta t \quad (7.4)$$

The integrated speed error is saturated against the blade pitch angle limits, which are converted to integral speed error limits:

$$\bar{\omega}_E^n = \text{MIN} \left(\text{MAX}(\bar{\omega}_E^n, 0), \frac{\phi_{\max}}{K_p GK} \right) \quad (7.5)$$

where $\phi_{\max} = \pi/2$ rad is the maximum blade pitch allowed in the present study. With the integral speed error determined the integral gain term, ϕ_i , can be calculated:

$$\phi_i = K_i \cdot \bar{\omega}_E^n \cdot GK \quad (7.6)$$

The proportional and integral terms are summed for the desired blade pitch angle, ϕ' :

$$\phi' = \phi_p + \phi_i \quad (7.7)$$

The desired blade pitch angle must again be saturated against the maximum blade pitch angle:

$$\phi'' = \text{MIN}(\text{MAX}(\phi', 0), \phi_{\max}) \quad (7.8)$$

This saturated desired blade pitch angle is then used to determine the desired pitching rate to get to this angle from the current point:

$$V'_\phi = \frac{\phi'' - \phi^n}{\Delta t} \quad (7.9)$$

The desired pitching rate is saturated against the maximum pitch actuator speed, $V_{\phi_{max}}$, set to $8^\circ/\text{s}$ in the present:

$$V_\phi = \text{MIN}\left(\text{MAX}\left(V'_\phi, -V_{\phi_{max}}\right), V_{\phi_{max}}\right) \quad (7.10)$$

Note the algorithm in equation (7.10) saturates the pitch rate against both a positive or negative maximum rate, hence the negative term in the inner function. The saturated pitch rate is finally used with the time step to determine the new blade-pitch angle, ϕ^{n+1} :

$$\phi^{n+1} = \phi^n + V_\phi \Delta t \quad (7.11)$$

The blade-pitch angle is then returned to the solver for processing.

7.3.2 JONSWAP Irregular Waves

Irregular wave models provide more genuine calculations of wave characteristics by employing empirical spectral models. The JONSWAP wave model (Hasselmann, 1973) is employed during the present study to provide stochastic irregular wave height predictions. It is an empirically determined spectral model developed using data collected during the Joint North Sea Wave Project in 1969. The JONSWAP model accounts for seas not fully developed (McCormick, 2010) making it ideal for simulation of FOWT, as sea states can take hundreds of miles to develop and FOWT are expected to be installed only ~10-30 miles offshore. This model is available as a boundary-condition (BC) input, with initialization, in CFDSHIP-IOWA v4.5. Two user input parameters, significant wave height, H_s , and the probable wavelength, λ_s , are required for initialization. With these parameters, and empirical coefficients (see McCormick, 2010), the size and shape of the wave energy spectrum are determined. This frequency spectrum is then discretized into a user-defined number of waves, each with amplitudes determined from the corresponding power in the spectrum. These individual waves comprise the overall waveform. They are each randomly phased relative to each other and summed to produce a wave elevation function of time. The wave throughout the domain is calculated and prescribed for the first time step. During each

subsequent time step, however, the wave elevation at the inlet BC only is determined and this height is prescribed to the free-surface. From that point the waves propagate into the simulation domain and are subjected to solution conditions.

All simulations in this chapter considering irregular waves (cases 1 and 3, to be discussed in section 7.4.1 and described in Table 12) used the input parameters prescribed for OC3 load cases in (Jonkman et al., 2010). The significant height is prescribed at $H_s = 6$ m and the peak spectral period, T_p , is 10 s. The wave module of CFDShip-Iowa requires the probable wavelength, and this is determined from the peak spectral period using the wave dispersion equation (McCormick, 2010):

$$\lambda_s = \frac{gT_p^2}{2\pi} \tanh\left(\frac{2\pi h}{\lambda_s}\right) \quad (7.12)$$

Where h is the water depth, prescribed in the OC3 at 320 m. Solving this implicit equation gives a probable wave length of $\lambda_s = 156.08$ m .

7.3.3 Mann Turbulence Model

Atmospheric turbulence is modeled with the Mann wind turbulence model (Mann, 1998), recommended for turbine design by the IEC in their certification load cases (IEC, 2005). The Mann model is a 3-dimensional wind turbulence model built, with wind technology in mind, upon the atmospheric sheared spectral tensor model that Mann previously developed in (Mann, 1994). It provides stochastic turbulent fluctuations in all 3 dimensions and accounts for wind shear based on elevation. Mann applied an isotropy parameter to his spectral tensor model (Mann, 1994) to account for the shearing effect on eddy deformation over time, This parameter, referred to as the shear distortion parameter, γ , is set to $\gamma = 3.9$ as per (IEC, 2005). As a result of the application of γ the velocity fluctuations are observed to be statistically different in all 3 principal directions, streamwise, transverse, and vertical, with the largest velocity deviations observed in the streamwise direction, the next largest deviation in the transverse direction, and finally the smallest velocity fluctuations in the vertical direction. The streamwise standard deviation, σ_1 , is calculated as a function of turbulent intensity, I_{ref} , and mean hub-height velocity, U_{hub} :

$$\sigma_1 = I_{ref} (0.75U_{hub} + b) \quad (7.13)$$

where $b = 5.6$ m/s is a constant recommended in (IEC, 2005). The transverse and vertical standard deviations, σ_2 and σ_3 , respectively, are calculated as constant fractions of σ_1 :

$$\sigma_2 = 0.7\sigma_1 \quad (7.14)$$

$$\sigma_3 = 0.5\sigma_1 \quad (7.15)$$

Using these parameters the module develops a 3-dimensional power spectrum in the frequency domain. An inverse FFT scheme is used to transform this power spectrum into the spatial domain to calculate a turbulent velocity vector as a function of space at each point, $\tilde{\mathbf{u}} = \tilde{\mathbf{u}}(X, Y, Z)$. After the spatial turbulent function is determined the local mean streamwise velocity as a function of height is determined using a logarithmic velocity profile:

$$u(Z) = U_{hub} \frac{\ln(Z/z_0)}{\ln(Z_{hub}/z_0)} \quad (7.16)$$

where Z is the local height from the SWL in the fixed-earth system, z_0 is a roughness length dependent upon surface type, and Z_{hub} is the nominal hub height from the SWL. The mean velocity profile, $u(Z)$, is superimposed onto the 3-dimensional fluctuations and a vector function of space describing the velocity field is developed:

$$\mathbf{u} = \mathbf{u} \begin{bmatrix} \tilde{u}_x(X, Y, Z) + u(Z) \\ \tilde{u}_y(X, Y, Z) \\ \tilde{u}_z(X, Y, Z) \end{bmatrix} \quad (7.17)$$

To apply the wind field the Mann module develops a 3-dimensional rectangular sub-grid based on user defined uniform grid spacing, ΔL , and grid dimensions N_1 , N_2 , and N_3 along the fixed-earth frame dimensions, X, Y, and Z, respectively. The grid dimensions may be different but, as a requirement of the FFT process, must each be a power of 2. The physical dimensions of this sub-grid are then:

$$L_i = N_i \Delta L \quad (7.18)$$

where i refers to each X, Y, and Z in the fixed-earth frame. This sub-grid is designed to be spatially larger than the simulation domain in the Y-Z plane (i.e the "streamwise" plane nominally perpendicular to the rotor plane) to ensure coverage of the entire simulation domain. The X-dimension of the sub-grid is also designed to be longer than the streamwise extent of the simulation domain, but in a different fashion, discussed in the next paragraph. During initialization this sub-grid is populated with the vector velocity function \mathbf{u} based on the X, Y, and Z positions of each individual point inside the grid volume. The developed field is interpolated into the simulation domain and passed to the solver as the wind field for the first time step.

For subsequent time steps the Mann model invokes Taylor's frozen turbulence hypothesis (Panofsky et al., 1984). Taylor's hypothesis states that the evolving turbulent field is essentially isotropic with respect to time. Accordingly there is no difference, from a statistical perspective, between the true, changing turbulent field and that of a single 'frozen' turbulent field simply advected with the mean, bulk motion of the fluid. The Mann sub-grid with the original frozen field is transported an incremental distance at the hub velocity at the end of every time step:

$$\Delta L_1 = U_{hub} \Delta t \quad (7.19)$$

After this transport the Y-Z slice of the sub-grid aligned with the inlet BC of the solution domain is interpolated onto the BC and presented to the solver as the inlet conditions for the next time step. This process continues until the streamwise extent of the sub-grid is reached. The velocity field was developed from a 3-dimensional power spectrum and is, accordingly, periodic in all 3-dimensions. In the Mann model the streamwise length of the sub-grid, L_1 , also defines the temporal extent of the sub-grid:

$$L_1 = N_1 \Delta L = U_{hub} T_M \quad (7.20)$$

where T_M is the streamwise period of the 3-dimensional Mann sub-grid. At simulation time $t = T_m$ the physical extent of the sub-grid is reached. For the next time step the sub-grid is repeated from the beginning and the process continues. To avoid any low frequency problems with this field periodicity Mann recommends keeping T_M greater than the

expected simulation time (Mann, 1994). Only a brief overview with the details relevant to the present study is presented here. The reader is referred to (Li et al., 2015) for a more thorough discussion of the implementation and validation of the Mann model in CFDShip-Iowa.

In the cases using wind turbulence in this chapter (cases 2 and 3, to be discussed in section 7.4.1 and described in Table 12) the turbulent intensity factor, I_{ref} , U_{hub} , and Z_{hub} are set at constant values of 0.14, 11.4 m/s, and 90 m, respectively, as per OC3 LC 2.2 (Passon et al., 2007) and OC3 LC 5.2 (Jonkman et al., 2010), which used identical values and are both investigated in this study. The surface roughness length, λ , is not explicitly stated in the OC3 documentation and is chosen to be 0.001 m, a typical roughness length for rough seas (Burton, 2011 pg. 17). The Mann model, as implemented into CFDShip-Iowa, utilizes a constant grid spacing in all 3 dimensions. However dimensions of Δx , Δy , and Δz were utilized for the turbulent wind field sub-grid utilized by the OC3 (Passon et al., 2007), which prove too coarse in the Y-Z dimensions for the present study. As these dimensions were intended to cover the rotor-diameter of 125 m in the Y-Z plane this gives a Y and Z spacing of Δx , which was rounded to 4 m and chosen for the constant grid spacing of the current study. The simulation domain in the present study is 315 m in the Y-direction and 315 m in the Z-direction above the SWL. This provides a dimension of Δx . The grid dimension numbers are required to be powers of 2 so the dimension is rounded up and Δx . The simulation domain in the present study is 480 m long, approximately 3 wave periods of a 10 second Airy wave at the domain depth. This length would require a minimum dimension of Δx , rounded again to 128. However it is desired for the Δx dimension, combined with the 4m grid spacing, to produce a sub-grid with a period larger than the simulation time, as mentioned previously. The maximum simulation time of the simulations in the present study is 630 s. Using equation (7.20) this provides a desired streamwise dimension of:

$$(7.21)$$

which represents the minimum desired dimension (i.e. if the sub-grid began repeating right at 630 s). Rounding this up to the next power of 2 gives a dimension of 2048. However using Δx was observed to introduce a ~40% increase in computational time per time step. An increase in initialization is expected, and observed, with this dimension over smaller

dimensions used in testing. The time step solution time increase is not completely understood, though, as the slices interpolated into the solution domain per time step are in the Y-Z plane, and an increase in Δt shouldn't affect the time required to cut that slice during each time step, and this is assumed to be due to memory or stack limitations. Nevertheless the next lowest power of 2, 1024, was seen to perform acceptably during testing and was chosen for the dimension of Δx . This means, however, that the sub-grid ends and starts over at some point during the simulations in this study—an unfortunate compromise. With equation (7.20) the dimension of 1024 gives a Mann period of:

$$(7.22)$$

This period gives a Mann sub-grid frequency of f_M . This frequency is only 30% of the lowest frequency expected in the present study, 0.00939 Hz in the surge rigid-body translational mode as noted in section 2.5.1, and only 8.2% of the pitch natural frequency of 0.034 Hz, both of which need to be avoided. The box is also repeated only once before the simulation ends. It is assumed, therefore, that this very low Mann frequency will not cause significant excitation in the present study.

7.4 Simulation Conditions and Design

Three simulations (cases 1-3) are performed in this chapter, as detailed in Table 12, using the fine grid set described in chapter 3. Load cases from the OC3 are chosen to demonstrate the described models individually for analysis. In case 1 the JONSWAP model is utilized in a simulation using the conditions from OC3 LC 4.2 (Jonkman et al., 2010), a hydrodynamic only simulation. Time-series statistics and PSD estimates are compared to those of NREL's OC3 4.2 results. The results of case 1 are used to identify likely frequencies of excitation from the JONSWAP model in CFDShip-Iowa as well as differences produced by different hydrodynamic solution methods (CFD vs. Morison's equation). In case 2 the waves are turned off and the platform is fixed in the initial, upright position with the platform/tower centerline parallel to the vertical, the hub height at 90 m above the SWL, and the rotor plane facing the upstream direction. The rotor is engaged with VS and BP controls and the Mann wind model is utilized using conditions from the OC3 LC 2.2 (Passon et al., 2007), an aerodynamic only simulation. Results are also transformed into the frequency domain for

comparison to NREL. Case 2 is intended to distinguish the flow characteristics provided by the Mann model and the expected response of the generator. In case 3 the conditions of the OC3 LC 5.2 are simulated utilizing all the models and controllers developed and implemented into the code throughout this dissertation. Results are compared to those of NREL and differences discussed.

7.5 Results and Discussion

7.5.1 Case 1

A single-phase hydrodynamic simulation using conditions from OC3 LC 4.2 and employing the crowfoot mooring lines is performed for case 1. The platform is released from the initial position and subjected to irregular wave excitation provided by the JONSWAP model. The simulation is allowed to run for 630 s and the first 30 s of transient development removed—the same method used by NREL in their LC 4.1 results. The tabulated time-series statistics of case are presented in Table 13 and PSD plots of the instantaneous wave elevation and platform motions are presented in Figure 56 and Figure 57, respectively. The wave elevation is measured at the origin of the fixed-earth system, which is 157 m (1 wavelength) downstream of the inlet, at the transverse center, and vertically located at the SWL. The wave elevation standard deviation of case 1, 1.49 m, is identical to that of NREL's waves and the mean elevation, while showing a 500% relative difference from NREL, is only -0.04 m from the expected 0.00. This difference in mean elevation could potentially be due to the simulation length. At 600 s of simulation time any wave frequency less than produced by the JONSWAP spectral model will not have seen a full period, producing a non-zero mean at that frequency. In Figure 56 the waveform produced in case 1 clearly has energy at this frequency and below. The minimum and maximum wave elevations are also both seen to be decreased in magnitude from those of NREL, with the maximum down 41.1% and the minimum down 23.2%. To produce irregularity in the JONSWAP spectrum the individual component waves are randomly phased relative to each other. This phasing produces a large uncertainty in the minimums and maximums here, for both the present study and in NREL's results, and the waveform would need to be simulated several times for phase-averaging. This was not an option in the present study considering high computational costs. The minimum and maximum amplitudes are considered, however, within acceptable tolerances

for the present study. It is also suspected that the phasing of the wave form is not as significant as grid induced dissipation. The spatial resolution of the simulation domain, seen in Figure 18 to be much coarser in the streamwise direction than in the vertical direction near the SWL, causes a loss of high-frequency content of the irregular wave form. Investigations of the effects of these two aspects is relegated to future work. The wave elevation PSD in Figure 56 shows very similar peak energy content relative to that of NREL. However, a shift of -0.015 Hz from the expected peak spectral frequency of 0.1 Hz is observed. A significant amount of time was spent investigating and testing to determine a cause and eliminate this shift but the cause was never found. The JONSWAP spectrum, as described in section 5.3.2, accounts for undeveloped, or fetch-limited, seas. The peak spectral frequency is a function of fetch, or length of sea over which wind has blown, and is seen to grow lower as the sea becomes more fully developed (McCormick, 2010). The peak spectral period, and inversely the peak spectral frequency, was prescribed as an input in NREL's results but is calculated inside the JONSWAP module in CFDShip-Iowa, suggesting that perhaps a larger fetch is considered by CFDShip-Iowa than that corresponding to a peak frequency of 0.1 Hz. The present study shows significantly more energy in lower frequencies than that of NREL as discussed previously. The wave form energy slope of case 1 is also seen to drop faster than that of NREL in frequencies above 0.1 Hz, even after considering the 0.015 Hz shift, likely due to grid dissipation. NREL's energy content shows a substantial drop-off in energy content at ~0.3 Hz, which isn't produced in the present study, also perhaps due to differing sea-development criteria between the two models.

The rigid-body motion PSD plots of surge, pitch, heave, and yaw in case 1 are compared to those of NREL in Figure 57. The NREL's predictions of yaw were too low to report, as Morison's equation has no mechanism of producing it through viscosity, and they are not presented in Figure 57. The present study is seen to agree with NREL in both mean pitch and mean heave. A 275% larger mean surge is predicted in case 1 relative to NREL, along with a 73.4% increase in standard deviation. The minimum and maximum values of surge are also seen to have increased 38.1% and 35.3%, respectively. The increases in surge magnitudes seem counter-intuitive given the losses in wave height magnitudes, however these are likely explained by the increase in low-frequency wave energy relative to NREL's

results seen in Figure 56. At the surge frequency of 0.00939 Hz the present study is seen to have at least 2 orders of magnitude more power than NREL, whose power results were saturated at 10^{-4} . The surge PSD in Figure 57 shows slight increases in power at the surge frequency in case 1, with a larger increase in power at the pitch frequency. These increases in surge and pitch frequency content are attributed to increased energy content in the waves at their respective frequencies. Surge power at the wave frequency is seen to have a small increase in peak energy with a secondary peak at 0.064 Hz not seen in NREL's results. This secondary peak is visible in the case 1 results in the wave PSD of Figure 56, and its presence is seen in each of the motion PSD plots of Figure 57. Hydrodynamic loading differences between CFD in the present study and Morison's equation used by NREL are most likely the reason for the extra wave power in case 3. Overall the surge frequency predictions of case 1 agree well with those of NREL.

A similar increase in wave power relative to NREL is seen in Figure 56 at the pitch and heave frequencies, very similar at 0.034 Hz and 0.032 Hz, respectively. Accordingly, an increase in pitch standard deviation, 60.5% relative, is observed with increases in minimum and maximum values, at 13.2% and 6.6%, respectively. More pronounced increases are seen in heave, with case 2 predicting a 93.8% increase in standard deviation and increases of 28.8% and 57.1% in minimum and maximum, relative to NREL. The pitch PSD of Figure 57 shows similar increases of energy at each of the surge, pitch, and wave frequencies as seen in the surge PSD for the same reasons. The heave PSD, however, shows less energy at the heave frequency than NREL with a significant increase at the secondary peak wave frequency observed in case 1, 0.064 Hz. The reduced heave frequency power is a factor of increased heave restoration provided by the crowfoot lines used in case 1 (see Figure 27 for comparison). The secondary peak wave frequency power increase is potentially from a harmonic resonance, as 0.064 Hz is twice the heave natural frequency of 0.032 Hz, or could be related to viscous heave forces not accounted for in NREL's results during wave motion. The yaw PSD is also presented although NREL's results are too low to present. The yaw PSD shows most of the yaw energy in the peak wave frequencies, with a spike at the yaw natural frequency, seen to be 0.131 Hz. The crowfoot mooring lines are seen to provide similar, if not greater, yaw restoration so it would be expected to see less yaw and, therefore,

less yaw energy than NREL. This is assumed to be a result of modeling error between the two models and the level of tower discretization in the present and points at a need for structural damping in the crowfoot model. It is noted, however, that the maximum yaw seen in the simulation was 0.02° and might not be worth the complexity of adding to the model. Overall the results of case 1 agree with NREL enough to justify the usage of the JONSWAP model in CFDShip-Iowa for comparison in case 3 of this chapter.

7.5.2 Case 2

In case 2 a single-phase aerodynamic simulation using conditions from OC3 LC 2.2 using the BP controller. Case 2 requires a modification to the gain coefficients in the BP controller, as OC3 LC 2.2 was run by NREL before the controller gain update to help mitigate negative damping. A change is also made to the VS controller, changing the VS control region scheme from a constant-torque scheme to a constant-power scheme, which reduces torque in VS region 3 at the expense of higher generator speed fluctuations, which will require more blade-pitch actuation. To prevent generator overload during these fluctuations the maximum generator is set to 10% above the rated generator torque to 47,402.91 N-m. These points are discussed in section 5.2 and (Jonkman et al., 2009, Jonkman, 2010). The platform is fixed in this simulation in the upright position and the rotor is subjected to a turbulent wind field produced by the Mann wind model. The simulation is allowed to run for 630s and the first 30 s of transience removed. The Mann model in CFDShip-Iowa accepts a user-defined random number seed for generation, such that the same wind field was produced for both cases 2 and 3 for consistency. The streamwise velocity at hub height, measured both at the inlet and at the initial hub point 1 wavelength into the simulation domain, is shown in Figure 58 with statistics tabulated in Table 14. Note that NREL's FAST simulation software does not use a discretized solution domain and therefore has no inlet to directly compare to—the velocity is calculated at each blade section individually—and that the inlet section of results is compared to NREL's hub results. The mean velocities at the inlet of case 2 are seen to be in agreement with the expected means, and . NREL is also seen to produce these means with insignificant differences. However the standard deviations of all 3 velocities in case 2 are reduced from their expected values, which are the values predicted by NREL's Mann model. The relative differences of standard

deviation in case 2 are observed to grow from streamwise (-12.8%), to transverse (-32.9%), to vertical (-54.1%). This growth trend is also seen in all relative differences of maximums and minimums and suggests an input or model error. The source of this difference was investigated but not discovered, and the errors considered a compromise of the study. The Mann model is input at the inlet BC and is susceptible to grid dissipation in the same fashion as the JONSWAP wave model. The mean velocities seen at the hub again agree with the expected values in surge and, with a slight 0.05 m/s error, in the transverse direction. The mean velocity in the vertical direction is seen to increase to 0.09 m/s. It is likely the imposed-pressure BC used at the top of the solution domain, combined with the continuity constraint in the domain is the cause for this small mean difference. The standard deviation in the streamwise direction has deteriorated to 41.4% less than the desired, with a similar decrease in deviation of 39.5% in the transverse direction. The standard deviation in the vertical direction actually improves 13.2%, growing to 0.58 m/s from 0.45 m/s at the inlet (remember the desired is 0.98 m/s). This reduction in deviation is visible in Figure 58. The streamwise velocity shows a marked decrease in fluctuation amplitude at the hub compared to the inlet. Also visible in Figure 58 is the periodicity of the Mann model, with the inlet velocity signal showing obvious repetition at 359 s.

Another view of the decay of the turbulent fluctuation is shown in Figure 59, where streamwise velocity contours show the spatial breakdown of smaller scale turbulent structures as they travel through the solution domain. A closer inspection of Figure 58 reveals a reduction in the higher turbulent frequencies, associated with the small-scale structure breakdown. This is verified in PSD plots of all 3 velocity components at both the inlet and at the hub, shown in Figure 60. In the region between the inlet and the hub the energy content is seen to decrease rapidly for frequencies greater than ~ 0.2 Hz in the streamwise direction. This same power decrease occurs for both of the transverse and vertical directions but at higher cut-off frequencies, ~ 0.4 Hz in the transverse direction and ~ 0.8 Hz in the vertical, the differences being functions of the slower velocities in these directions combined with anisotropic grid spacing in the three dimensions of the simulation domain. A deficiency in low-frequency fluctuations exists at the inlet for all 3 dimensions with the smallest deficiency in the streamwise direction and, following the growth trend

discussed previously to the transverse and vertical directions—the largest deficiency being about 3 orders-of-magnitude in power occurring in the vertical direction at ~ 0.002 Hz. These low-frequency deficiencies are unfortunate, as the rigid-body modes of the turbine in these dimensions, surge (0.00939 Hz), pitch (0.034 Hz), and heave (0.032 Hz), are inside this window of power loss, and thus it is suspected that case 3 will see diminished platform excitation from the wind in these critical frequencies. The inlet velocities also have a different PSD shape than that of NREL, with a gentler slope in the frequency range 0.001 Hz to about 0.6 Hz, where the energy content decreases rapidly relative to NREL. It is unlikely that this higher frequency (>0.6 Hz) deficiency will have a significant effect on platform motions as their modes are all well lower than 0.6 Hz. However, considering the change in controller gains to effectively increase the frequency of the BP controller in case 2, less blade-pitch actuation is expected in response to this high-frequency deficiency.

The generator predictions of case 2 are presented in Table 15 with PSD plots of these predictions shown in Figure 61. The mean generator statistics—torque, speed, and generated power—agree very strongly with those of NREL verifying the effectiveness of the BP/VS controllers working in tandem. The maximum torque in case 2 is a function of both the generator speed and blade pitch, as the controllers attempt to keep the aerodynamic torque at its optimum value in VS region 3 (see section 4.3.4) to prevent overloading the generator while not overshooting the rotor deceleration. As such these values, for both NREL and the present study, are very close to the rated torque of the generator, 43.1 kN-m, and only a 1.1% difference is seen between case 2 and NREL in maximum torque. A significant increase in minimum torque is seen in case 2, 22.6% relative, however. This is explained in the minimum generator speed statistics, which, despite only a 3.9% relative difference, show an important difference in absolute value. The minimum generator speed in case 2 is 1152 RPM, about halfway into VS control region 2-1/2, where the priority is limiting tip-speed by rapidly increasing generator torque. However the minimum generator speed predicted by NREL is 1109 RPM, which is well into VS region 2 where a lower generator-torque is used to keep the tip-speed ratio at its optimum. This causes wider variance of both speed and torque, potentially decreasing fatigue life, with case 2 showing a 69.1% decrease in generator torque deviation and a 52.5% decrease in generator speed deviation compared to

NREL. These trends are also seen in the generator power results, which is directly proportional to both speed and torque. The mean generator power in case 2 is only 2.8% above that of NREL, and the maximum power increase seen in case 2 is a mere 0.3%. However the minimum generated power is predicted 30.8% higher than that of NREL, leading to a 66.3% decrease in power fluctuations which can help to smooth electrical grid penetration. A substantial 92.6% decrease in mean blade pitch is predicted in case 2 as well as 72.0% and 82.7% decreases in standard deviation and maximum, respectively, compared to NREL. These decreases are attributed to the substantially lower wind fluctuations seen in case 2 relative to NREL. The function of the BP controller is to maintain constant aerodynamic power beyond rated generator speed, reducing the amount of aerodynamic torque transmitted to the LSS when loading grows too large. It is assumed that the lower deviations of the wind field of case 2, especially in the transverse and vertical directions as these component are in the rotor plane, produce lesser aerodynamic torque deviations, and the BP controller is called on less frequently than predicted by NREL. The aerodynamic torque developed at the LSS, just as in OC3 LC 5.1 (see section 4.3.4), was not available in NREL's results. However, without a phase diagram, the aerodynamic torque was not able to be back-calculated as in section 4.3.4. The lesser aerodynamic torque of NREL, therefore, remains an assumption and is considered for future work.

Generator prediction PSD plots for case 2 are shown in Figure 61. Exemplary agreement is shown in expected energy content at the rotor frequency in each of torque, speed, and power while the blade pitch PSD shows a definite decrease in content, a result of decreased high-frequency fluctuations in case 3 and, perhaps, an over-prediction by NREL of the BTI effect (see chapter 3) on aerodynamic torque loss. All results show decreases in predicted low-frequency energy content with the blade-pitch PSD showing a more significant decrease as a result of the decrease in low-frequency wind fluctuations. Note the second and third blade frequencies, P2 and P3, respectively, marked in Figure 61. These are not harmonics of the rotor, but are instead the 3 frequencies produced the 3 blades passing the tower. All plots also show a decrease in low-frequency content, with the blade pitch PSD showing a larger decrease relative to NREL compared to the other PSD plots. This is also a direct result of the diminished low-frequency wind fluctuations seen in Figure 60.

The results of case 2 and the results of NREL show definite differences in terms of expected wind power and frequency. However, these differences are explainable and consistent with expected responses. It is therefore concluded from the results of case 2 that the Mann wind model of CFDSHIP-Iowa is producing a wind field acceptable for comparison to NREL and that the BP controller, in coordination with the VS controller, is functioning as desired. As such it is concluded to proceed with utilization of these models in a comprehensive simulation.

7.5.3 Case 3

In case 3 all of the described models—the crowfoot mooring model, the VS/BP controller modules, JONSWAP irregular waves, and the Mann turbulence model—are engaged as the platform is released and all platform and rotor motions are predicted. The BP controller gains are modified to correspond with the tuned gains for the floating spar-buoy platform, which reduce the effective controller response frequency below that of the pitch natural frequency and the VS controller region 3 scheme is set to constant-torque rather than constant power to avoid negative damping from the VS controller (see Larsen et al., 2007b). More details on these controller changes can be found in (Jonkman, 2010). The turbine is subjected to wind, wave, and mooring excitation for 630 s and the first 30 s of transience removed. Platform motion PSD plots are presented in Figure 62 and tabulated in Table 16. Strong agreement is seen in mean pitch and mean heave between case 3 and NREL. A 12.6% reduction in mean surge is seen in case 3, likely a result of the increased surge restoration in the crowfoot mooring lines. This additional force is also likely the reason behind the 9.5% reduction in minimum surge and 12.1% reduction in maximum surge. The maximum pitch in case 3 also agrees strongly with NREL. However an 85.9% difference in minimum pitch is seen in case 3. This may be a result of the additional energy content seen at the pitch frequency of the wave form (see Figure 56). This may also be a result of the large deviations from the initial point, where the coupling effects of the crowfoot mooring lines have not been investigated. An additional 0.6 m of travel is observed in both minimum and maximum heave in case 3 relative to NREL, a result of viscous friction forces on the tower in the vertical direction in case 3, which are not accounted for by NREL. Substantial differences are seen in yaw between case 3 and NREL's results, with the present study

predicting a 54% reduction in both minimum and maximum yaw. NREL showed no yaw in their hydrodynamic only solution suggesting that the wind is accountable for all the yaw seen in their LC 5.2 results. In case 3 is also observed a significant increase in yaw compared to the results of case 1. A large peak at the pitch frequency is seen in the yaw PSD of Figure 62 which could, potentially, simply be a component of the wind as this peak does not exist in the hydrodynamic only case 1. However it is assumed that strong pitch/yaw coupling exists due to the asymmetric fairlead placement of the upstream lines behind the pitch axis (see Figure 19). An investigation of the effect of fairlead placement, by rotating the fairleads 180° about the platform azimuth, was contemplated but left for future work. Strong agreement in predicted wave energy response, along with the characteristic shift of the peak wave frequency of case 3, is visible in the surge pitch, and heave PSD plots of Figure 62, with the content spread between two dominant frequencies of 0.064 Hz and 0.085 Hz. These wave responses are very similar to those of case 1 (see Figure 57). The surge and pitch frequencies are visible in the surge PSD, but at less power than that predicted by NREL. When compared to case 1 the pitch PSD shows an increase at the surge frequency contributed by the wind but actually shows a decrease at the pitch frequency. This is likely the effect of aerodynamic drag from the tower, neglected in NREL's results. In the heave PSD a similar content is predicted between NREL and case 3, with the present study predicting a greater increase from case 1 than NREL shows between their corresponding results. This is potentially due to the greater mean vertical velocity in the wind field of case 2 and case 3. A peak that is probably the surge frequency is visible in both the results of case 3 and those of NREL. This is suggested to be a result of mooring line tension, significantly increased at the large surge displacements seen in case 3. At these large displacements the nominally slack catenary mooring lines become taut and begin stretching. The magnitude of these forces, which have a component in the negative vertical direction, is large enough to overcome some buoyancy such that there is expected to be surge-heave coupling, especially at large surge displacements. The yaw PSD shows multiple frequencies of interest. The surge and pitch frequencies are visible as the crowfoot mooring lines provide yaw coupling with both of these directions. The wave frequency shows a significant increase from case 1, despite a similar wave form. This is also likely due to the increased mooring forces of case 3 relative to case 1 due to increased surge displacement. The yaw natural frequency. 0.12 Hz

for NREL and 0.13 Hz in the present study, is visible in both plots. A peak is seen at the rotor frequency in both plots, likely due to BTI, with similar content but probably insignificant in terms of resultant physical yaw—the maximum yaw experienced in case is 1.06° .

The generator predictions of case 3 are tabulated in Table 17 and PSD plots presented in Figure 63. The VS and BP controller team, inseparable at the rated wind velocity used in these simulations, are working to keep the aerodynamic torque at its optimum value. Thus, despite aerodynamic and hydrodynamic solution differences between the present study's usage of CFD and NREL's FAST, excellent agreement is seen in the mean predictions of generator torque, speed, and power. The generator torque deviation is predicted to be practically identical between case 3 and NREL's results, despite a 15.1% increase in minimum torque in case 3, suggesting that this difference might be due to an individual large-scale fluctuation and is statistically insignificant. A 7.4% increase in minimum generator speed is seen in case 3 as well as an 8.5% decrease in maximum generator speed, corresponding to a considerable 37.4% difference in generator speed standard deviation. This can be attributed to the decreased low-frequency content seen in case 3 compared to the wind field of NREL and, potentially, to shorter excursions into VS region 2 in case 3. Strong agreement in generated power mean and deviation is seen, despite a 23.5% increase in minimum power and an 8.5% decrease in maximum power observed in case 3. This indicates the effectiveness of the NREL VS and BP controllers to keep output power steady. The blade pitch controller is called on less in case 3 than in NREL's results, similar to the results of case 2, with case 3 showing a 72.9% reduction in mean blade pitch and a 68.4% reduction in deviation. This was to be expected given the reduced blade pitch actuation in case 2. However case 2, which featured a fixed platform, was likely dominated by attached flow, not having to contend with oscillating upstream and downstream velocities, and case 3 has large platform pitching motions. Shown in Figure 64 are the limiting streamlines on the suction side of a blade, sufficiently far from the tower to avoid BTI, at a (local) maximum upstream velocity. Note that this solution was randomly chosen based on availability but is assumed to be indicative of upstream velocity behavior. The root separation region is seen to extend almost halfway up the blade and the instability seen at 82% blade span in Figure 54

is again visible, but another vortex has formed next to it at the higher mean velocity of case 3. The significant loss of aerodynamic torque caused by this separation, again unable to be directly compared to that of NREL, is more than likely the dominant cause for this reduced blade pitch usage.

In the PSD plots of Figure 63 strong agreement is seen between case 3 and the results of NREL in high-frequency response in torque, power, and blade-pitch. Less energy is seen in low frequencies in case 3 in all four categories, a result of the diminished low-frequency energy content in the wind seen in case 2. Frequencies are more difficult to identify in these PSD plots as they are controlled results and generator torque, blade pitch, and, to an extent due to constant torque in VS region 3, generator power are saturated at one side. Nevertheless the dominant wave frequency is visible in each plot and case 3 is seen to agree well with NREL in content at these frequencies. The generator speed plot shows the wave shift discovered in case 1, with a secondary peak at the rotor frequency and P2 (note case 3's P3 content was very low). The generator speed is the input of the VS and BP controllers and only indirectly controlled. This makes the generator speed, via its direct connection to rotor speed, more subject to the physical excitation in the simulations. This is likely the reason the wave shift is visible in the generator speed PSD but not the more directly controlled torque, power, or blade pitch PSD plots.

A multi-perspective view of the overall solution field is shown in Figure 65. The top left and right images of Figure 65 show Q-criterion (Hunt et al., 1988) isosurfaces, indicating vortical activity, of the wake from behind (top left) and above (top right). Extensive dynamic wake skewing and stretching can be seen in both images while the wake maintains a nominally helical shape. However the variability in velocity of the wake due to Mann turbulence causes the helical structure to break down, weakening the effectiveness of the wake. The wake refinement grid used in this study was not long enough to capture this breakdown but, when compared to the very clean wake structure developed in steady air in Figure 49, it can be assumed that the breakdown of case 3 will certainly take less time than that of a steady air assumption. This breakdown length is an important to know, considering the vast majority of turbines, onshore or offshore, are built in farms. The instantaneous irregular free-surface is also visible in Figure 65 top right. A mid-plane, $Y=0$ slice, colored

by streamwise velocity, is shown in the bottom left of Figure 65. Note the streamwise direction in this frame is left to right. A number of items of interest are present in this image. The fluctuations produced by the Mann model can be seen as well as the strong wake region. The vortices being shed from the tower and the wake deficit caused by root shedding can be seen immediately behind the tower. Wake skewing and shearing nearer to the wake are visible as well. The view at bottom right of Figure 65 has the Q-criterion turned down to 0.5 to expand the isosurface content providing a qualitative view of the Mann turbulent fluctuations inside the solution domain. Noticeable is the stretching and deforming of coherent structures near the surface due to shear.

7.6 Conclusions

In this chapter a blade-pitch controller is coupled with JONSWAP irregular waves, Mann wind turbulence, VS control, crowfoot mooring lines, and high resolutions CFD to perform simulations of FOWT and predict motions, power, and loading, both aerodynamic and hydrodynamic. Three simulations are performed in a stepwise approach to identify the capability and function of the models introduced in this chapter. All time-series results are transformed to the frequency domain for analysis and are compared to those of NREL's publicly available OC3 results. A hydrodynamic only simulation (case 1), designed after the OC3 LC 4.2, is performed using the JONSWAP model and crowfoot lines. The platform is allowed to move freely and rigid-body motions are predicted. The JONSWAP model, as utilized, produces an incorrect peak spectral frequency. The model also produces more low-frequency energy content than that seen in NREL's content, providing more excitation in the rigid-body modes of concern, and all motions are seen to be increased relative to NREL. The results of case 1 provide insight to what to expect from wave excitation in the third simulation of this chapter. The wave form, as delivered, is considered acceptable for usage.

A second simulation (case 2), designed after OC3 LC 2.2, is an aerodynamic only simulation designed to test the Mann model inside CFDShip-Iowa. The platform is fixed and the motions of the inertial rotor, subjected to VS and BP controllers, are predicted based on wind excitation using the Mann model. The Mann model, as utilized, produces notably lower fluctuation magnitudes and low-energy content than those produced and used by NREL in their simulations. The turbulent fluctuations are then subjected to grid dissipation

between their development point at the inlet and the hub causing further high-frequency loss. Similar means are seen in generator torque, speed, and power, but with significant decreases in standard deviation of these three parameters, shown to be a result of the low-frequency deficiency. BP actuation is also shown to be reduced from that of NREL's results, assumed from reduced aerodynamic torque.

The complete code is used in a third simulation (case 3), designed after OC3 LC 5.2. In this simulation the JONSWAP wave model and Mann turbulent model are both active, providing two-phase irregular excitation. All motions, platform and rotor, are predicted subject to crowfoot mooring forces and VS and BP control, respectively. Good agreement is seen in platform motions, considering the diminished low-frequency energy provided by the present wind model. Aerodynamic drag of the tower is seen to be a notable factor in predicted pitch. The generator statistics show strong agreement with those of NREL, while a marked decrease in BP actuation is seen in case 3. This is suggested to be a function of separation, shown to occur during upstream relative velocity of the platform. The results provide a sense of verification for the current method and its further usage and refinement is encouraged.

The discrepancies of the input wave and wind models used in the simulations in this chapter when compared to the inputs used by NREL, combined with grid dissipation and increased mooring restoration, explain the motion and power differences between the results in the dissertation and those of NREL.

7.7 Figures

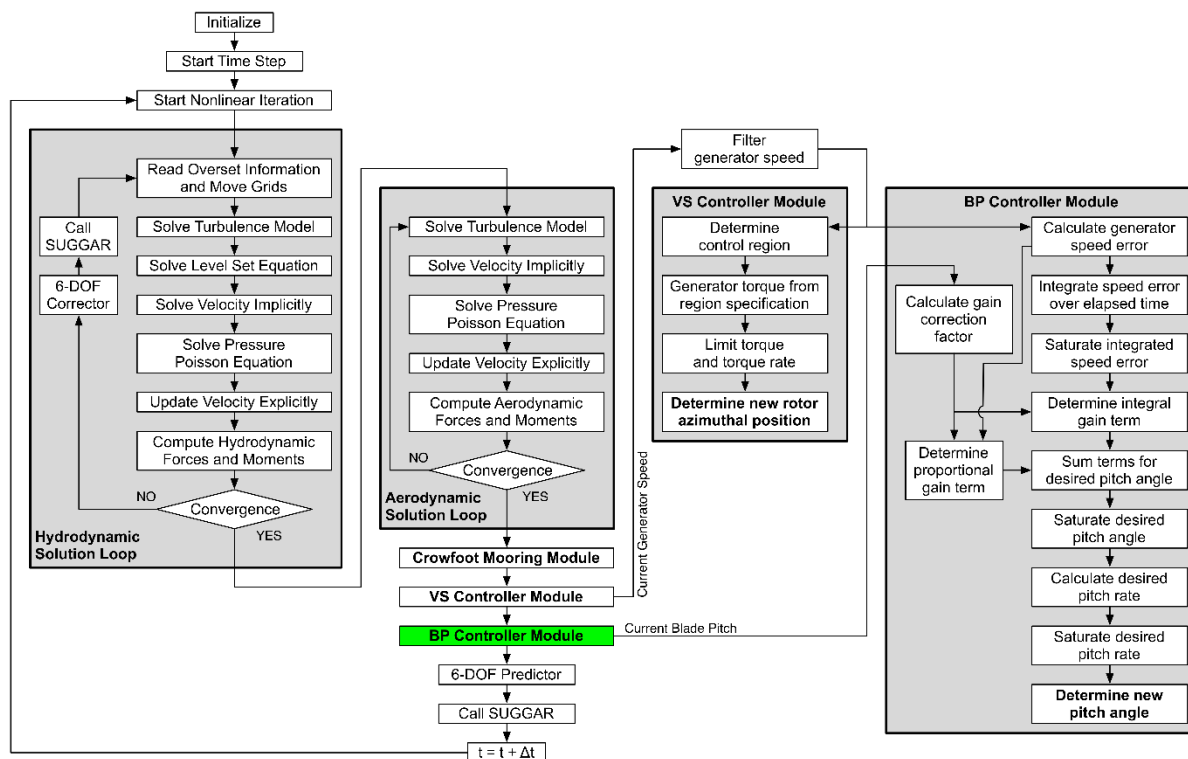


Figure 55 Solution strategy including VS and BP controller modules

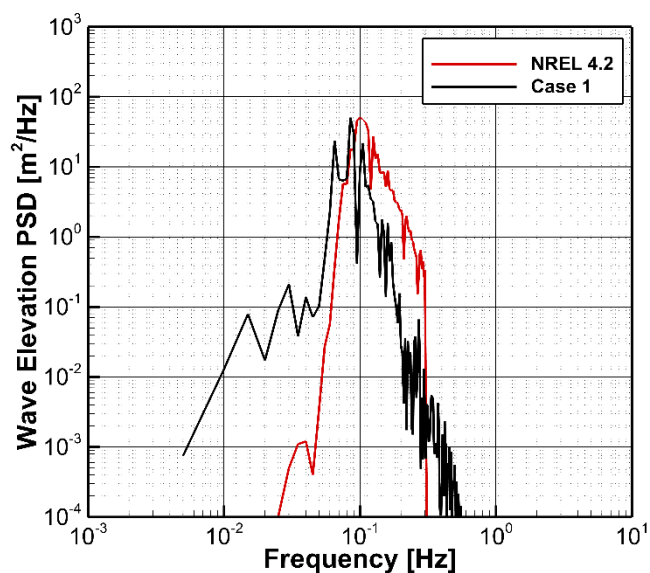


Figure 56 PSD of wave elevation in case 1 compared to that of NREL

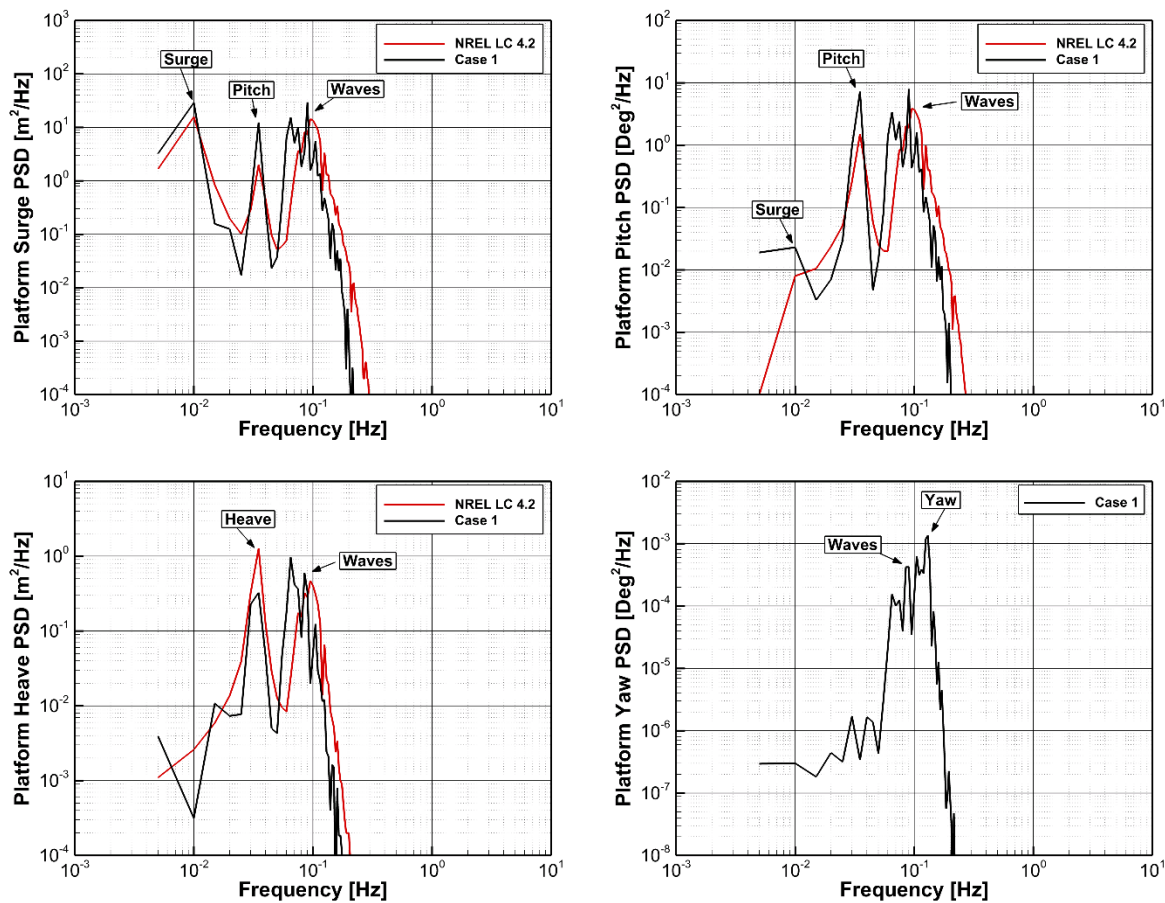


Figure 57 Platform motion PSD plots of case 1 compared to NREL

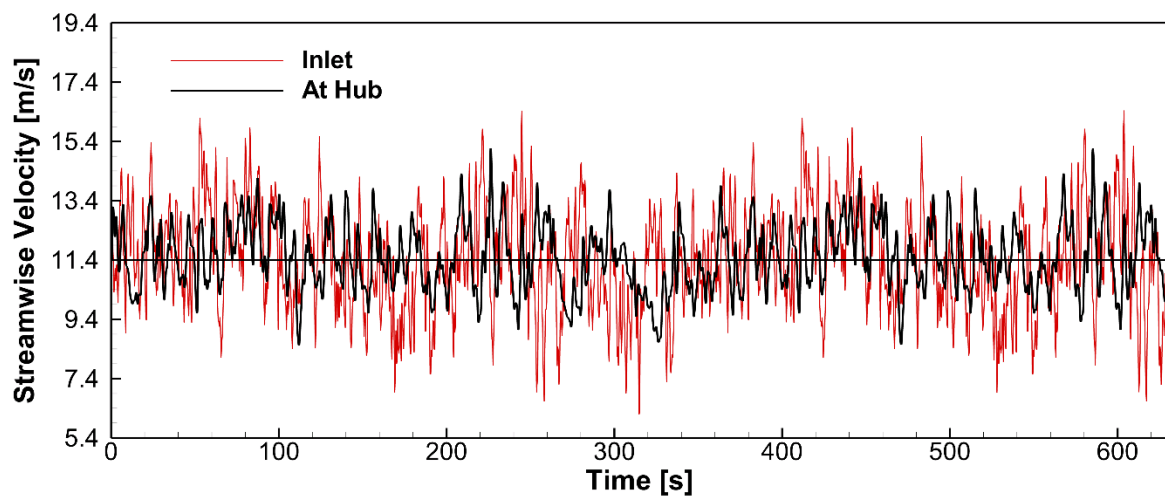


Figure 58 Time history of streamwise velocity at hub height for cases 2 and 3

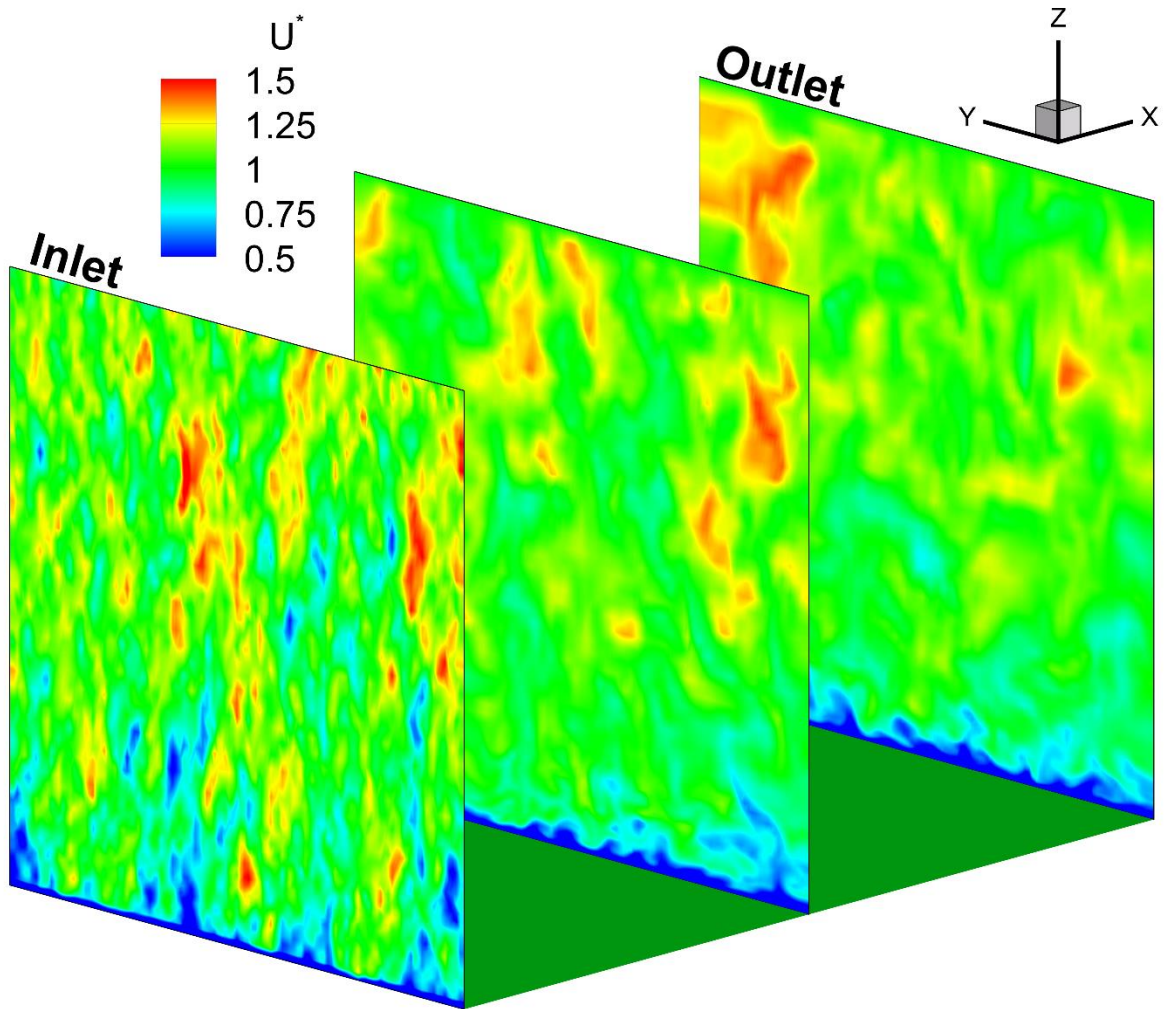


Figure 59 Contours of normalized streamwise velocity at inlet, mid-plane, and outlet

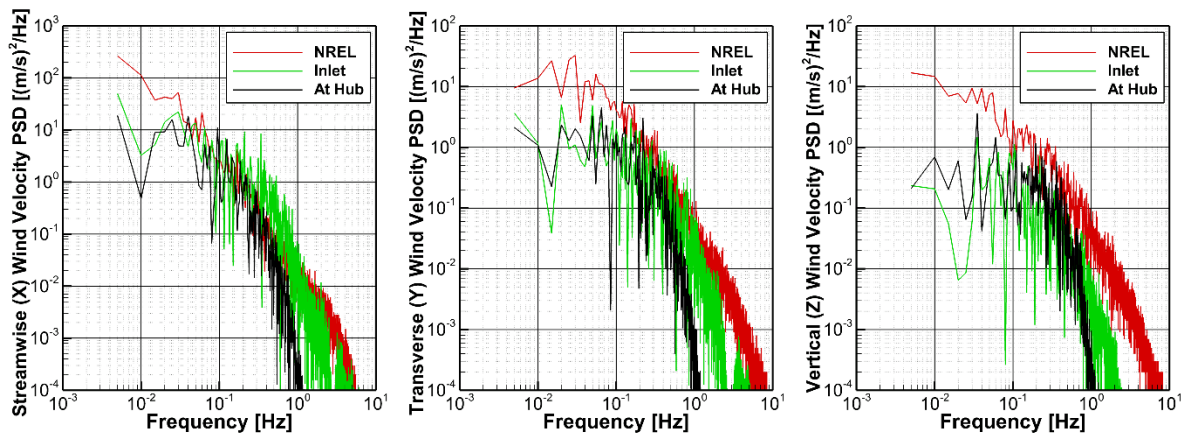


Figure 60 PSD plots of turbulent wind velocity components

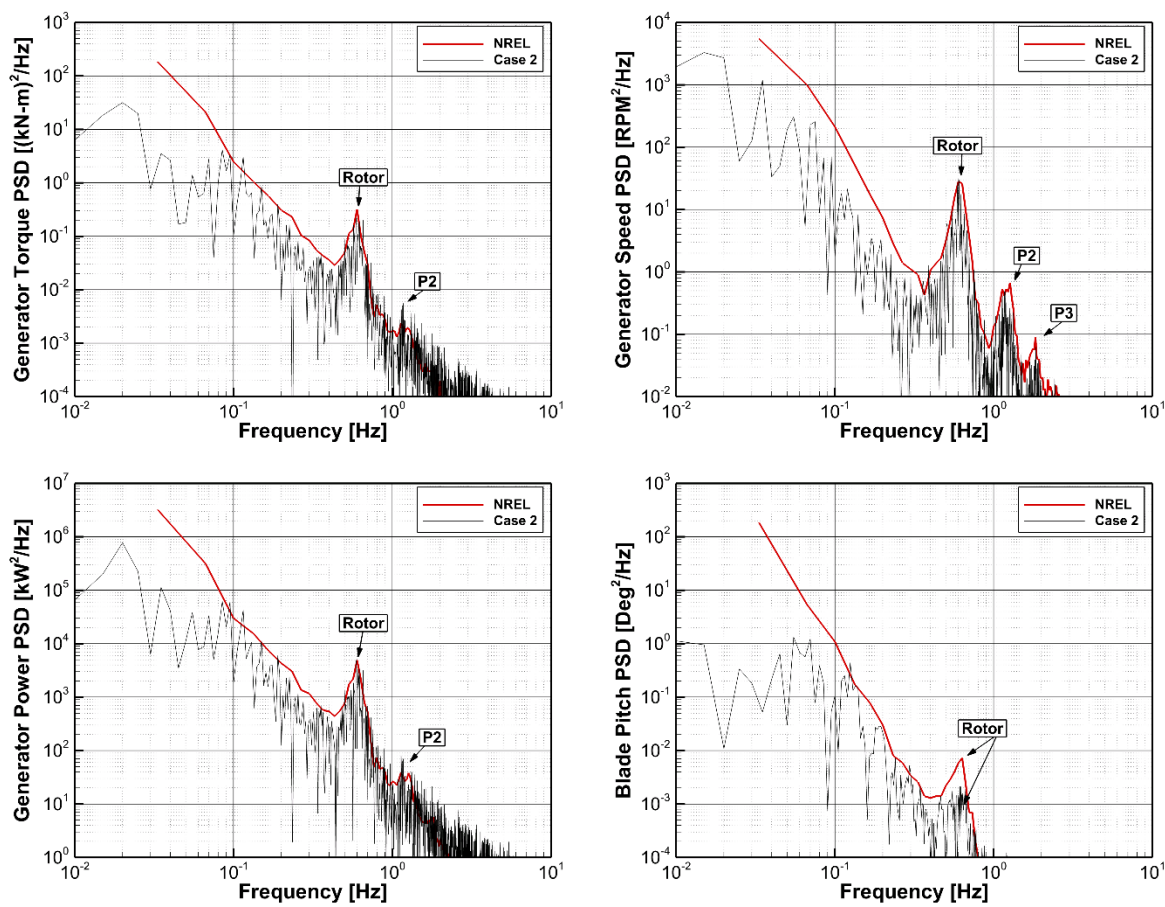


Figure 61 PSD plots of generator predictions of case 2 compared to those of NREL

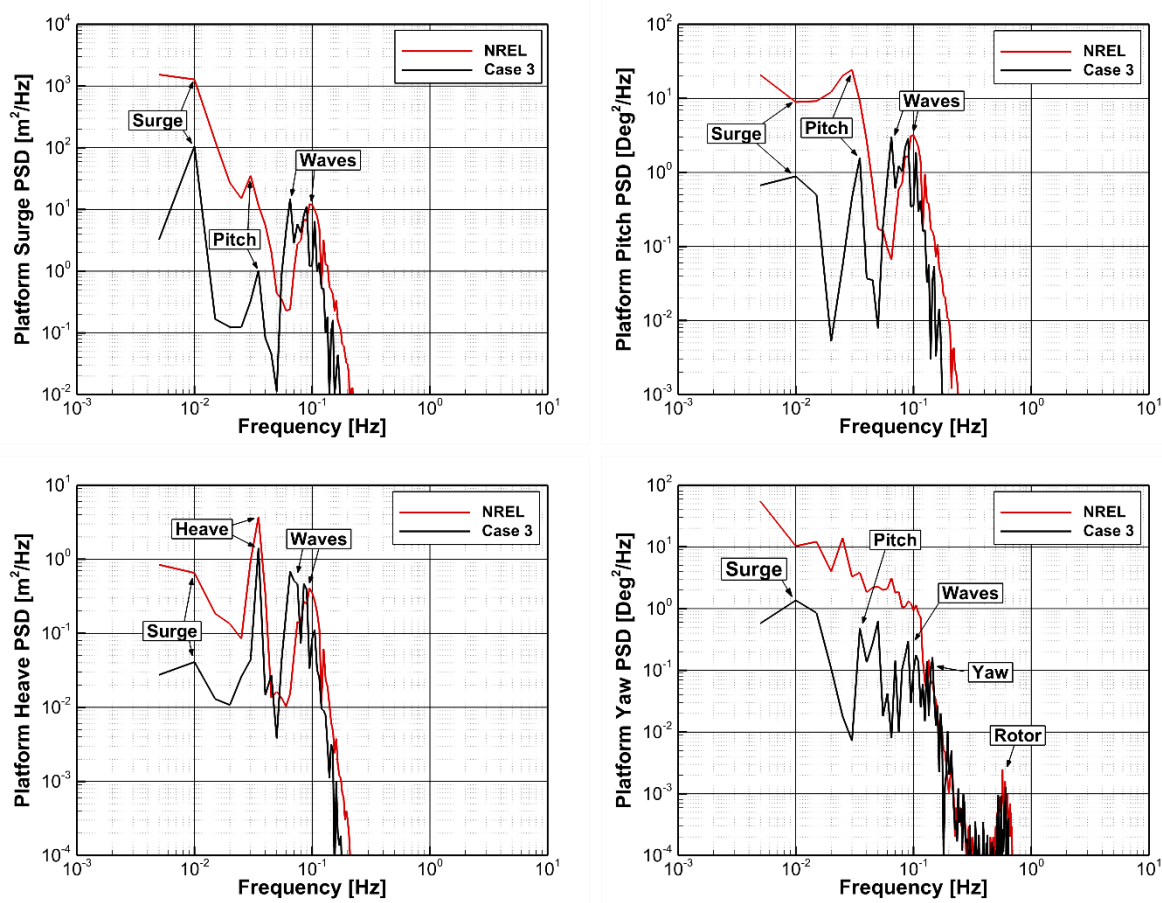


Figure 62 Platform motion PSD plots of case 3 compared to NREL

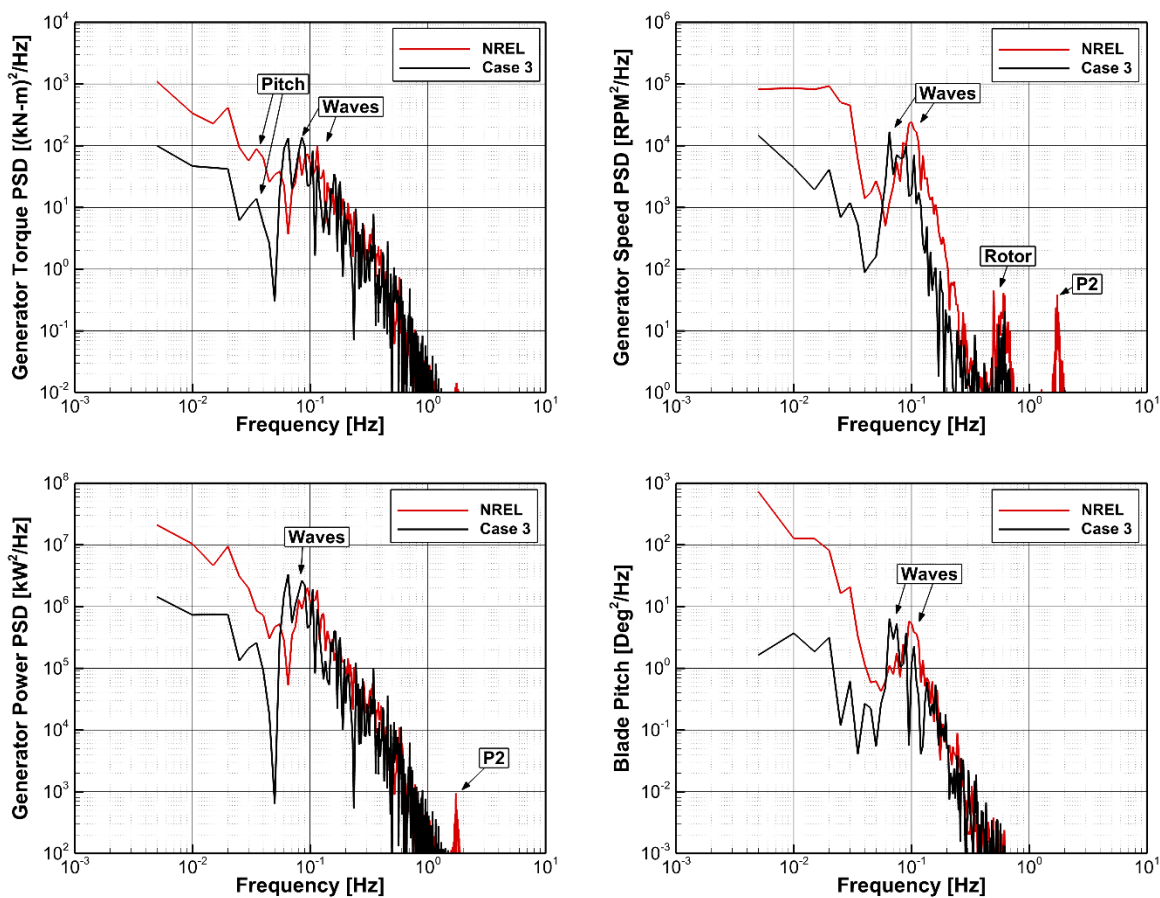


Figure 63 Generator prediction PSD plots of case 3 compared to NREL



Figure 64 Limiting streamlines on suction side of blade at maximum upstream velocity

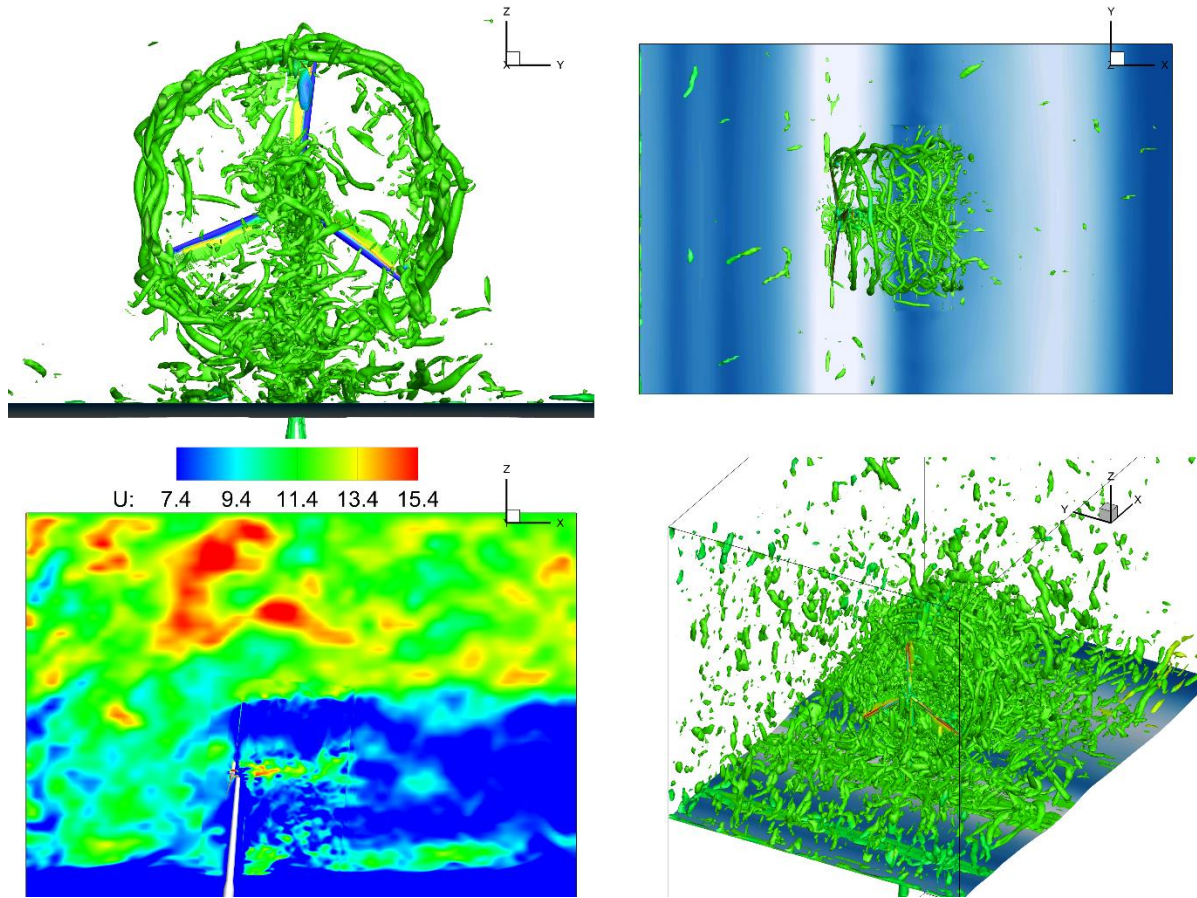


Figure 65 Clockwise from top-left: Rear view with isosurfaces of $Q=1$; Top view with $Q = 1$ and wave surface; Top-front view with $Q=0.5$; Streamwise velocity contours at $Y=0$ slice

7.8 Tables

Table 12 Simulation case matrix

Case	Platform Motions	Rotor Motions	Wind Conditions	Mann Dimensions	Wave Conditions
1	Predicted	None	N/A	N/A	JONSWAP $H_S = 6$ m; $\lambda_S = 156.08$ m
2	None	VS and BP controlled	$V_H = 11.4$ m/s $I_{ref} = 0.14$	$1024 \times 128 \times 128$ $\Delta L = 4$ m	N/A
3	Predicted	VS and BP controlled	$V_H = 11.4$ m/s $I_{ref} = 0.14$	$1024 \times 128 \times 128$ $\Delta L = 4$ m	JONSWAP $H_S = 6$ m; $\lambda_S = 10$ s

Table 13 Wave elevation and platform motions of case 1 compared to those of NREL

		Wave	Platform Motions			
		Elevation [m]	Surge [m]	Pitch [°]	Heave [m]	Yaw [°]
Case1	Min	-3.44	-3.99	-1.54	-0.94	-0.02
	Max	3.63	3.41	1.45	0.88	0.02
	Mean	-0.04	-0.30	-0.07	0.00	0.00
	Std. Dev.	1.49	1.37	0.61	0.31	0.01
NREL	Min	-5.84	-2.89	-1.36	-0.73	0.00
	Max	4.73	2.52	1.36	0.56	0.00
	Mean	0.01	-0.08	-0.07	0.00	0.00
	Std. Dev.	1.49	0.79	0.38	0.16	0.00
Relative %	Min	-41.1%	38.1%	13.2%	28.8%	-
	Max	-23.2%	35.3%	6.6%	57.1%	-
	Mean	-500.0%	275.0%	0.0%	0.0%	-
	Std. Dev.	0.0%	73.4%	60.5%	93.8%	-

Table 14 Statistics of wind field of case 2 and case 3 compared to those of NREL

	Velocity [m/s]	Inlet			At Hub		
		u	v	w	u	v	w
Case 2 and 3	Min	6.19	-3.52	-1.35	8.53	-2.55	-1.85
	Max	16.44	3.44	1.71	15.17	3.28	2.19
	Mean	11.39	0.00	0.00	11.40	0.05	0.09
	Std. Dev.	1.71	0.92	0.45	1.15	0.83	0.58
NREL	Min	-	-	-	6.60	-4.11	-2.84
	Max	-	-	-	17.37	4.87	3.37
	Mean	-	-	-	11.43	-0.03	-0.01
	Std. Dev.	-	-	-	1.96	1.37	0.98
Relative %	Min	-6.2%	-14.4%	-52.4%	29.3%	-38.0%	-34.8%
	Max	-5.4%	-29.4%	-49.2%	-12.7%	-32.7%	-34.9%
	Mean	-0.3%	-100.0%	-100.0%	-0.3%	-298.5%	-740.1%
	Std. Dev.	-12.8%	-32.9%	-54.1%	-41.4%	-39.5%	-40.9%

Table 15 Generator predictions of case 2 compared to those of NREL

		Generator			BP Controller
		Torque [kN-m]	Speed [RPM]	Power [MW]	Pitch [°]
Case1	Min	38.70	1152	4.530	0.00
	Max	43.57	1200	5.027	2.13
	Mean	42.72	1166	4.927	0.20
	Std. Dev.	0.83	7.47	0.119	0.45
NREL	Min	31.56	1109	3.463	0.00
	Max	44.07	1205	5.041	7.60
	Mean	41.56	1166	4.791	2.71
	Std. Dev.	2.69	15.64	0.353	2.60
Relative %	Min	22.6%	3.9%	30.8%	0.0%
	Max	-1.1%	-0.4%	-0.3%	-72.0%
	Mean	2.8%	0.0%	2.8%	-92.6%
	Std. Dev.	-69.1%	-52.2%	-66.3%	-82.7%

Table 16 Platform motion of case 3 compared to those of NREL

		Platform Motions			
		Surge [m]	Pitch [°]	Heave [m]	Yaw [°]
Case1	Min	10.30	2.47	-1.66	-0.83
	Max	27.36	6.14	0.69	1.06
	Mean	18.53	4.36	-0.44	-0.08
	Std. Dev.	3.14	0.64	0.34	0.30
NREL	Min	11.38	1.33	-1.07	-1.83
	Max	31.13	6.26	0.11	2.29
	Mean	21.19	4.25	-0.47	0.26
	Std. Dev.	4.10	0.84	0.22	0.83
Relative %	Min	-9.5%	85.9%	55.3%	-54.6%
	Max	-12.1%	-1.9%	546.1%	-53.6%
	Mean	-12.6%	2.7%	-5.4%	-131.3%
	Std. Dev.	-23.4%	-23.6%	52.7%	-63.7%

Table 17 Generator predictions of case 3 compared to those of NREL

		Generator			BP Controller
		Torque [kN-m]	Speed [RPM]	Power [MW]	Pitch [°]
Case1	Min	29.69	1079	3.203	0.00
	Max	43.09	1252	5.335	3.12
	Mean	39.73	1168	4.598	0.69
	Std. Dev.	4.35	34.95	0.608	0.78
NREL	Min	26.04	1004	2.593	0.00
	Max	43.09	1369	5.831	7.14
	Mean	40.42	1165	4.669	2.54
	Std. Dev.	4.36	55.83	0.627	2.48
Relative %	Min	15.1%	7.4%	23.5%	0.0%
	Max	0.0%	-8.5%	-8.5%	-56.3%
	Mean	-1.7%	0.2%	-1.5%	-72.9%
	Std. Dev.	-0.2%	-37.4%	-3.0%	-68.4%

CHAPTER 8: CONCLUSIONS AND FUTURE WORK

A high-resolution CFD-based wind turbine simulation tool capable of simulating FOWT and predicting aerodynamic and hydrodynamic loading is developed and tested in this dissertation. A CFD solution software, CFDShip-Iowa v4.5 is chosen as the solver for its ability to use high-resolution overset grids and the features built into it, including a rigid-body 6-DOF motion solver, a Mann wind turbulence model, and a JONSWAP irregular wave model, all of which are used in this work.

A mooring line model is first required for securing the turbine. A mooring model is developed and validated in chapter 4. The mooring line model, called the crowfoot, is shown to decrease overall system yaw and surge. With the mooring model functioning, and a proof-of-concept established, the resolution of the grid set utilized in the study was significantly increased to within reasonable limits considering computational and time resources.

In chapter 5 this new grid set is then tested and utilized in a parametric study of the blade-tower aerodynamic interaction considering streamwise platform motions. The results of this study show that BTI is affected by unsteady streamwise velocities and the oscillating wake of the tower. Upstream platform velocities are seen to produce a higher pressure in upstream of the tower and increase the effective angle of attack experienced by blade sections, causing a more pronounced BTI effect than downstream platform velocities. The BTI range is observed to be consistent across multiple studies, including the present, showing the BTI effects to begin at 30° of rotor azimuth prior to passing the tower and subsiding after 40° of rotor azimuth beyond the tower. This suggests an individual BP control tuned to streamwise platform velocity to help mitigate this angle of attack change.

A VS controller is implemented and used in chapter 6 to predict generator torque and speed—critical for proper prediction of aerodynamic loading below rated speed. The present study agrees well with NREL on predicted platform motions. Separation is predicted in the present study during upstream platform motion, reducing the developed aerodynamic torque. This produces an unfavorable operating speed range for the generator and mean generated power is decreased by 9%. A change to lower the minimum RPM value of VS control region 2 is suggested to increase delivered power in the present study.

In chapter 7 a BP controller is combined with JONSWAP irregular waves and Mann wind turbulence, along with the components designed and implemented in previous chapters, to provide a comprehensive system simulation at rated incoming velocity. The BP controller is vital to reducing aerodynamic torque transmitted to the LSS when winds increase, making it important for simulation purposes as well. The JONSWAP wave model is first tested and found to produce an acceptable wave form, but with an errant peak spectral period and increased low-frequency energy relative to NREL's results. The Mann model is also tested and is seen to produce excellent mean values but standard deviations that are noticeably lower than those produced by NREL. In this test the BP controller is seen to function, but less blade-pitch actuation occurs in case 3 relative to NREL, attributed to less aerodynamic torque being developed in case 3. Both the irregular wave and wind models are seen to suffer from grid dissipation in higher frequencies. A final simulation combining all of the models is performed for prediction of motions and power. This simulation represents, to the author's knowledge, the most comprehensive CFD-based FOWT simulation to date anywhere. The results show less overall platform motions than NREL as a result of increased mooring restoration in the present study as well as diminished low-frequency wave content. The results show exemplary agreement in mean generator torque, speed, and delivered power, with a large decreased in generator speed deviation as a result of the lesser platform motions seen in case 3. The BP controller is shown to function, but is used considerably less, assumed due to aerodynamic torque loss due to separation in case 3. Aerodynamic drag of the tower is noticed and its effect noted.

Multiple avenues for future development based on the present results exist. Optimization of mooring lines, or a method for design needs to be investigated, as the importance of stability of the spar-buoy FOWT is demonstrated herein. Structural damping in the mooring lines should be added as well to reduce unwanted oscillations. The addition of blade flexibility to these results would be expensive, but potentially more accurate in terms of loading predictions. The errors in both of the empirically based JONSWAP and Mann models should be cleaned up and results rerun to see the effect. A plethora of other turbine specific mathematical models—nacelle yaw, rotor brakes, gearbox, to name a few—could be implemented as well. Of course grid resolution is almost always considered helpful, and

could help mitigate the high frequency wind losses seen here as well as providing more accurate or length wake descriptions.

REFERENCES

- Airy, GB (1849). *Tides and waves*. London, J.J. Griffin.
- Bak, C, Aagaard-Madsen, H, and Johansen, J (2001). "Influence from blade-tower interaction on fatigue loads and dynamics". *Proc Wind Energy for the New Millennium Conference*, München.
- Balay, S, Buschelman, K, Eijkhout, V, Gropp, W, Kaushik, D, and Knepley, M (2010). *PETSc Users Manual: Revision 3.1*. United States.
- Bell, JB, Howell, LH, and Colella, P (1991). "An efficient second-order projection method for viscous incompressible flow". *10th AIAA Thermophysics Conference*, Honolulu, HI.
- Brommundt, M, Krause, L, Merz, K, and Muskulus, M (2012). "Mooring System Optimization for Floating Wind Turbines using Frequency Domain Analysis." *Energy Procedia*, 24(0), 289-296.
- Broyden, CG (1965). "A class of methods for solving nonlinear simultaneous equations." *Mathematics of Computation*, 19(92), 577-593.
- Burton, T (2011). *Wind energy handbook*. Chichester, West Sussex, Wiley.
- Carrica, P, Wilson, RV, Noack, R, Xing, T, Kandasamy, M, Shao, J, Sakamoto, N, and Stern, F (2006). "A Dynamic Overset, Single-Phase Level Set Approach for Viscous Ship Flows and Large Amplitude Motions and Maneuvering ". *26th Symposium on Naval Hydrodynamics* Rome, Italy.
- Carrica, PM, Wilson, RV, Noack, RW, and Stern, F (2007a). "Ship motions using single-phase level set with dynamic overset grids." *Computers and Fluids*, 36(9), 1415-1433.
- Carrica, PM, Wilson, RV, and Stern, F (2007b). "An unsteady single-phase level set method for viscous free surface flows." *International Journal for Numerical Methods in Fluids*, 53(2), 229-256.
- Chakrabarti, SK (2005). *Handbook of offshore engineering*. Amsterdam; London, Elsevier.
- Christiansen, S, Bak, T, and Knudsen, T (2012). "Minimum thrust load control for floating wind turbine". *2012 IEEE International Conference on Control Applications, CCA*

2012, October 3, 2012 - October 5, 2012, Dubrovnik, Croatia, Institute of Electrical and Electronics Engineers Inc.

- Christiansen, S, Knudsen, T, and Bak, T (2011). "Optimal control of a ballast-stabilized floating wind turbine". *1st Joint Symposium on Computer-Aided Control System Design, CACSD 2011 and Systems with Uncertainty, SU 2011, September 28, 2011 - September 30, 2011*, Denver, CO, United states, Institute of Electrical and Electronics Engineers Inc.
- De Ridder, EJ, Otto, W, Zondervan, GJ, Vaz, G, and Huijs, F (2014). "Development of a scaled-down floating wind turbine for offshore basin testing". *Asme 33rd International Conference on Ocean, Offshore Arctic Engineering, OMAE*.
- Deepwater Wind, L (2015). "Block Island Wind Farm - Deepwater Wind." from <http://dwwind.com/project/block-island-wind-farm/>.
- DOE (2015). "Wind Vision: A New Era for Wind Power in the United States".
- Fingersh, L, Hand, M, and Laxson, A (2006). "Wind Turbine Design Cost and Scaling Model".
- Graham, JMR, Brown, CJ, and Giannakidis, G (2001). "Aerodynamic Interaction between Wind-Turbine Rotor Blades and the Tower." *Proc EWEC 2001 Conference*, 359-361.
- GWEC (2015). "Global Wind Report 2014" http://www.gwec.net/wp-content/uploads/2015/03/GWEC_Global_Wind_2014_Report_LR.pdf.
- Hand, M, Simms, D, Fingersh, L, Jager, D, Cotrell, J, Schreck, S, and Larwood, S (2001). *Unsteady aerodynamics experiment Phase VI : wind tunnel test configurations and available data campaigns*. Golden, CO, National Renewable Energy Laboratory.
- Hansen, MH, Hansen, A, Larsen, TJ, and Øye, S (2005). "Control Design for a Pitch-Regulated, Variable-Speed Wind Turbine".
- Hasselmann, K (1973). *Measurements of Wind Wave Growth and Swell Decay during the Joint North Sea wave project, JONSWAP*. Hamburg, Deutsches Hydrographisches Institut.
- Huang, J, Carrica, P, and Stern, F (2008). "Semi-coupled air/water immersed boundary approach for curvilinear dynamic overset grids with application to ship hydrodynamics." *International Journal for Numerical Methods in Fluids*, 58(6), 591-624.

- Hunt, JCR, Wray, AA, and Moin, P (1988). "Eddies, Stream, and Convergence Zones in Turbulent Flows".
- IEC, IEC (2005). "Wind turbines - Part 1: Design requirements", IEC, IEC 61400-1.
- Jonkman, J (2007). "Dynamics Modeling and Loads Analysis of an Offshore Floating Wind Turbine", NREL, NREL/TP-500-41958.
- Jonkman, J (2010). "Definition of the floating system for Phase IV of OC3". Golden, CO, NREL, NREL/TP-500-47535 <http://purl.access.gpo.gov/GPO/LPS123215>.
- Jonkman, J, Butterfield, S, Musial, W, and Scott, G (2009). "Definition of a 5-MW Reference Wind Turbine for Offshore System Development", NREL, NREL/TP-500-38060.
- Jonkman, J, Larsen, T, Hansen, A, Nygaard, T, Maus, K, Karimirad, M, Gao, ZM, T., Fylling, I, Nichols, J, Kohlmeier, M, Vergara, J, Merino, D, Shi, W, and Park, H (2010). "Offshore Code Comparison Collaboration within IEA Wind Task 23: Phase IV Results Regarding Floating Wind Turbine Modeling". *European Wind Energy Conference (EWEC)*. Warsaw, Poland, NREL.
- Jonkman, JM, and Buhl, ML (2005). "FAST user's guide". Golden, CO, National Renewable Energy Laboratory, NREL/EL-500-38230 <http://www.nrel.gov/docs/fy06osti/38230.pdf>.
- Jonkman, JM, and NREL (2008). "Influence of control on the pitch damping of a floating wind turbine". Golden, CO, National Renewable Energy Laboratory <http://purl.access.gpo.gov/GPO/LPS101565>.
- Kim, H, Lee, S, and Lee, S (2010). "Numerical analysis on the aerodynamics of HAWTs using nonlinear vortex strength correction." *Current Applied Physics*, 10(2 SUPPL.), S311-S315.
- Kim, H, Lee, S, and Lee, S (2011). "Influence of blade-tower interaction in upwind-type horizontal axis wind turbines on aerodynamics." *Journal of Mechanical Science and Technology*, 25(5), 1351-1360.
- Kvittem, MI, Bachynski, EE, and Moan, T (2012). "Effects of Hydrodynamic Modelling in Fully Coupled Simulations of a Semi-submersible Wind Turbine." *EGYPRO Energy Procedia*, 24, 351-362.
- Lackner, MA (2013). "An investigation of variable power collective pitch control for load mitigation of floating offshore wind turbines." *WE Wind Energy*, 16(4), 519-528.

- Larsen, JW, Nielsen, SRK, and Krenk, S (2007a). "Dynamic stall model for wind turbine airfoils." *Journal of Fluids and Structures*, 23(7), 959-982.
- Larsen, TJ, and Hanson, TD (2007b). "A method to avoid negative damped low frequent tower vibrations for a floating, pitch controlled wind turbine." *Journal of Physics: Conference Series*, 75(1), 012073.
- Li, Y, Castro, AM, Carrica, PM, Sinokrot, T, and Prescott, W (2015). "Coupled multi-body dynamics and CFD for wind turbine simulation including explicit wind turbulence." *Renewable Energy*, 76, 338-361.
- Li, Y, Paik, KJ, Xing, T, and Carrica, PM (2012). "Dynamic overset CFD simulations of wind turbine aerodynamics." *Renewable Energy*, 37(1), 285-298.
- Mann, J (1994). "The spatial structure of neutral atmospheric surface-layer turbulence." *J. Fluid Mech. Journal of Fluid Mechanics*, 273(-1).
- Mann, J (1998). "Wind Field Simulation." *Probabilistic Engineering Mechanics*, 13(4), 269-282.
- Martin, H (2011). "Development of a Scale Model Wind Turbine for Testing of Offshore Floating Wind Turbine Systems". MSCE thesis, University of Maine
- Matha, D (2010). "Model Development and Loads Analysis of an Offshore Wind Turbine on a Tension Leg Platform, with a Comparison to Other Floating Turbine Concepts".
- Matha, D, Fischer, S-A, Hauptmann, S, Cheng, PW, Bekiropoulos, D, Lutz, T, Duarte, T, and Boorsma, K (2013). "Variations in Ultimate Load Predictions for Floating Offshore Wind Turbine Extreme Pitching Motions Applying Different Aerodynamic Methodologies". *ISOPE*. Anchorage, AK, International Society of Offshore and Polar Engineers.
- Matha, D, Schlipf, M, Cordle, A, Pereira, R, and Jonkman, J (2011). "Challenges in Simulation of Aerodynamics, Hydrodynamics, and Mooring-Line Dynamics of Floating Offshore Wind Turbines". *21st Offshore and Polar Engineering Conference*. Maui, Hawaii, NREL, 10.
- McCormick, ME (2010). *Ocean engineering mechanics : with applications*. Cambridge, Cambridge University Press.
- Menter, F (1994). "Two-Equation Eddy-Viscosity Turbulence Models for Engineering Applications." *AIAA Journal*, 32(8), 1598-1605.

- Morison, JR, Johnson, JW, and Schaaf, SA (1950). "The Force Exerted by Surface Waves on Piles." *Journal of Petroleum Technology*, 2(5), 149-154.
- Musial, W, Butterfield, S, and Boone, A (2003). "Feasibility of Floating Platform Systems for Wind Turbines".
- Musial, W, and Ram, B (2010). "Large-Scale Offshore Wind Power in the United States: Assessment of Opportunities and Barriers", NREL, NREL/TP-500-40745.
- Namik, H, and Stol, K (2010). "Individual blade pitch control of floating offshore wind turbines." *Wind Energy*, 13(1), 74-85.
- Nielsen, F, Hanson, T, and Skaare, B (2006). "Integrated Dynamic Analysis of Floating Offshore Wind Turbines". *25th International Conference on Offshore Mechanics and Arctic Engineering (OMAE2006)*, Hamburg, Germany.
- Noack, R (2005). "SUGGAR: A General Capability for Moving Body Overset Grid Assembly". *17th AIAA Computational Fluid Dynamics Conference*, Toronto, Ontario, Canada, AIAA.
- NREL (2001). "Unsteady Aerodynamics Experiment Phase VI Wind Tunnel Test Configurations and Available Data Campaigns". Washington, D.C; Oak Ridge, Tenn., U.S. Dept. of Energy, Office of Scientific and Technical Information <http://www.osti.gov/servlets/purl/15000240-1FhaHo/native/>.
- NREL (2011). "New Modeling Tool Analyzes Floating Platform Concepts for Offshore Wind Turbines (Fact Sheet)". Washington, D.C; Oak Ridge, Tenn., United States. Dept. of Energy ; Distributed by the Office of Scientific and Technical Information, U.S. Dept. of Energy <http://www.osti.gov/servlets/purl/1009297-dEDnUM/>.
- Panofsky, HA, and Dutton, JA (1984). *Atmospheric turbulence : models and methods for engineering applications*. New York, Wiley.
- Parkinson, GV, and Jandali, T (1970). "A wake source model for bluff body potential flow." *J. Fluid Mech. Journal of Fluid Mechanics*, 40(03).
- Passon, P, Kühn, M, Butterfield, S, Jonkman, J, Camp, T, and Larsen, TJ (2007). "OC3Benchmark Exercise of Aero-elastic Offshore Wind Turbine Codes." *Journal of Physics: Conference Series*, 75(1).
- Principle Power, I (2011). "Principal Power - WindFloat." from <http://www.principlepowerinc.com/products/windfloat.html>.

- Quallen, S, and Xing, T (2015). " An Investigation of the Blade Tower Interaction of a Floating Offshore Wind Turbine". *ISOPE*, Kona, Big Island, Hawaii.
- Robertson, A, Jonkman, J, Masciola, M, Molta, P, Goupee, A, Coulling, A, Prowell, I, and Browning, J (2013). "Summary of Conclusions and Recommendations Drawn from the DeepCWind Scaled Floating Offshore Wind System Test Campaign". *ASME 2013 32nd International Conference on Ocean, Offshore and Arctic Engineering*. Nantes, France, NREL.
- RWE Innogy (2014). "RWE Innogy - Gwynt Y Môr." from <http://www.rwe.com/web/cms/en/1202906/rwe-innogy/sites/wind-offshore/under-construction/gwynt-y-mr/>.
- Sánchez-Caja, A, Rautaheimo, P, and Siikonen, T (1999). "Computation of the incompressible viscous flow around a tractor thruster using a sliding-mesh technique". *Proceedings of the 7th International Conference on Numerical Ship Hydrodynamics, Nantes, France, July*.
- Schwartz, M, Heimiller, D, Haymes, S, and Musial, W (2010). "Assessment of Offshore Wind Energy Resources for the United States", NREL, NREL/TP-500-45889.
- Sebastian, T, and Lackner, M (2010). "A Comparison of First-Order Aerodynamic Analysis Methods for Floating Wind Turbines". *48th AIAA Aerospace Sciences Meeting Including the New Horizons Forum and Aerospace Exposition*, American Institute of Aeronautics and Astronautics.
- Skaare, B, Hanson, TD, and Nielsen, FG (2007). "Importance of control strategies on fatigue life of floating wind turbines". *26th International Conference on Offshore Mechanics and Arctic Engineering 2007, OMAE2007, June 10, 2007 - June 15, 2007*, San Diego, CA, United states, American Society of Mechanical Engineers.
- Skaare, B, Hanson, TD, Yttervik, R, and Nielsen, FG (2011). "Dynamic Response and Control of the Hywind Demo Floating Wind Turbine". *European Wind Energy Conference*, Warsaw, Poland.
- Skaare, B, Nielsen, FG, Hanson, TD, Yttervik, R, Havmøller, O, and Rekdal, A (2015). "Analysis of measurements and simulations from the Hywind Demo floating wind turbine." *Wind Energy*, 18(6), 1105-1122.
- Smith, SW (1997). *The scientist and engineer's guide to digital signal processing*. San Diego Calif., California Techn. Publ.

- Spalart, P, Deck, S, Shur, M, Squires, K, Strelets, M, and Travin, A (2006). "A New Version of Detached-eddy Simulation, Resistant to Ambiguous Grid Densities." *Theoretical and Computational Fluid Dynamics*, 20(3), 181-195.
- Statoil (2012). "Hywind by Statoil: The Floating Wind Turbine." from http://www.statoil.com/en/TechnologyInnovation/NewEnergy/RenewablePowerProduction/Offshore/Hywind/Downloads/Hywind_nov_2012.pdf.
- Steger, JL, and Benek, JA (1987). "On the use of composite grid schemes in computational aerodynamics." *Computer Methods in Applied Mechanics and Engineering*, 64(1-3), 301-320.
- Sung, SW, Lee, J, and Lee, I-B (2009). *Process identification and PID control*. Singapore; Hoboken, N.J., John Wiley.
- Wang, Q, Zhou, H, and Wan, D (2012). "Numerical simulation of wind turbine blade-tower interaction." *Journal of Marine Science and Technology (Japan)*, 17(3), 321-327.
- White, FM (2008). *Fluid mechanics*. Boston, McGraw-Hill Higher Education.
- Wilson, RV, Carrica, PM, and Stern, F (2006). "Unsteady RANS method for ship motions with application to roll for a surface combatant." *Computers and Fluids*, 35(5), 501-524.
- Xing, T (2015). "A General Framework for Verification and Validation of Large Eddy Simulations." *Journal of Hydrodynamics (Ser. B)*, 27(2), 163-175.
- Xing, T, Carrica, P, and Stern, F (2010a). "Large-Scale RANS and DDES Computations of KVLCC2 at Drift Angle 0 Degree". *Gothenburg 2010: A Workshop on CFD in Ship Hydrodynamics*, Gothenburg, Sweden.
- Xing, T, and Stern, F (2010b). "Factors of safety for Richardson extrapolation." *Journal of Fluids Engineering*, 132(6), 0614031-0640313.
- Zahle, F, Sørensen, NN, and Johansen, J (2009). "Wind turbine rotor-tower interaction using an incompressible overset grid method." *Wind Energy*, 12(6), 594-619.

APPENDICES

A1: Mooring Line Code (Fortran 90)

```

SUBROUTINE single_line_visual_output (Ax,Ay,Az,Fx,Fy,Fz,&
  CB_i,EA_i,W_i,L_i,file_num,N)
  !
  ! This subroutine creates x,y,z data for single lines for loading into Tecplot
  !

  use global_parameters

  IMPLICIT NONE

  REAL(kind=8)      :: Ax,Ay,Az,Fx,Fy,Fz   ! Positions
  REAL(kind=8)      :: CB_i,EA_i,W_i,L_i   ! Line properties
  INTEGER           :: file_num,N,i
  REAL(kind=8)      :: c_alpha,s_alpha     ! X-axis angles
  REAL(kind=8)      :: HF,VF,HA,VA
  REAL(kind=8)      :: Xs(N),Zs(N),Te(N),s(N)

  ! calculate forces
  do i = 1,N
    s(i) = L_i*i/N
  end do

  call catenary(dsqrt((Fx-Ax)**2+(Fy-Ay)**2),Fz-Az,L_i,EA_i,W_i,CB_i,&
    1.d-6,HF,VF,HA,VA,N,s,Xs,Zs,Te)

  c_alpha = (Fx - Ax)/dsqrt((Fx-Ax)**2 + (Fy-Ay)**2)
  s_alpha = (Fy - Ay)/dsqrt((Fx-Ax)**2 + (Fy-Ay)**2)

  if (mod(it,mooring_output) == 0) then
    if (it == its) then
      write(file_num,*)'variables=time,X,Y,Z'
    end if

    do i = 1,N
      if (i == 1) then
        write(file_num,138)time
      end if

      write(file_num,"(f12.8,f10.3,f10.3,f10.3)")time,(Xs(i)*c_alpha+Ax)/clength,&
        (Xs(i)*s_alpha+Ay)/clength,(Zs(i)+Az)/clength
    end do
  end if

138 format('ZONE, T="'',f8.4,' seconds"')
end subroutine single_line_visual_output

SUBROUTINE crowfoot_visual_output (Ax,Ay,Az,Bx,By,Bz,Cx,Cy,Cz,Jx,Jy,Jz,&
  CB_i,EA_i,W_i,L_JA,L_JB,L_JC,file_num,N)
  !
  ! This subroutine creates x,y,z data for crowfoot lines for loading into Tecplot
  !

  use global_parameters

```

```

IMPLICIT NONE

REAL(kind=8)      :: Ax,Ay,Az,Bx,By,Bz,Cx,Cy,Cz,Jx,Jy,Jz ! Positions
REAL(kind=8)      :: CB_i,EA_i,W_i,L_JA,L_JB,L_JC      ! Line properties
REAL(kind=8)      :: c_alpha,c_beta,c_gamma,s_alpha,s_beta,s_gamma ! Sines and
                                                              !cosines of x-axis angles

INTEGER           :: N ! Number of nodal positions
INTEGER           :: file_num,i ! Misc
REAL(kind=8)      :: HF_A,HA_A,VF_A,VA_A,HF_B,HA_B,VF_B,VA_B,HF_C,HA_C,VF_C,VA_C
REAL(kind=8)      :: Xs_A(N),Zs_A(N),Xs_B(N),Zs_B(N),Xs_C(N),Zs_C(N),Te(N),s(N)

! Calculate forces
do i = 1,N
  s(i) = L_JA*i/N
end do
call catenary(dsqrt((Ax-Jx)**2+(Ay-Jy)**2),Jz-Az,L_JA,&
  EA_i,W_i,CB_i,1.d-6,HF_A,VF_A,HA_A,VA_A,N,s,Xs_A,Zs_A,Te)

do i = 1,N
  s(i) = L_JB*i/N
end do
call catenary(dsqrt((Bx-Jx)**2+(By-Jy)**2),Bz-Jz,L_JB,&
  EA_i,W_i,-1.d0,1.d-6,HF_B,VF_B,HA_B,VA_B,N,s,Xs_B,Zs_B,Te)

do i = 1,N
  s(i) = L_JC*i/N
end do

call catenary(dsqrt((Cx-Jx)**2+(Cy-Jy)**2),Cz-Jz,L_JC,EA_i,W_i,-1.d0,&
  1.d-6,HF_C,VF_C,HA_C,VA_C,N,s,Xs_C,Zs_C,Te)

! Start by determining angles
c_alpha = (Ax - Jx)/dsqrt((Ax-Jx)**2 + (Ay-Jy)**2)
s_alpha = (Ay - Jy)/dsqrt((Ax-Jx)**2 + (Ay-Jy)**2)
c_beta = (Bx - Jx)/dsqrt((Bx-Jx)**2 + (By-Jy)**2)
s_beta = (By - Jy)/dsqrt((Bx-Jx)**2 + (By-Jy)**2)
c_gamma = (Cx - Jx)/dsqrt((Cx-Jx)**2 + (Cy-Jy)**2)
s_gamma = (Cy - Jy)/dsqrt((Cx-Jx)**2 + (Cy-Jy)**2)

! Output
if (mod(it,mooring_output) == 0) then
  if (it == its) then
    write(file_num,*) 'variables=time,X,Y,Z'
  end if

  do i = 1,N
    if (i == 1) then
      write(file_num,139)time
    end if

    write(file_num,"(f12.8,f10.3,f10.3,f10.3)")time,&
      (-Xs_A(i)*c_alpha+Ax)/clength,&
      (-Xs_A(i)*s_alpha+Ay)/clength,(Zs_A(i)+Az)/clength
  end do

  do i = 1,N
    if (i == 1) then
      write(file_num,140)time
    end if

    write(file_num,"(f12.8,f10.3,f10.3,f10.3)")time,&

```

```

        (Xs_B(i)*c_beta+Jx)/clength,&
        (Xs_B(i)*s_beta+Jy)/clength, (Zs_B(i)+Jz)/clength
    end do

    do i = 1,N
        if (i == 1) then
            write(file_num,141)time
        end if

        write(file_num,"(f12.8,f10.3,f10.3,f10.3)")time,&
            (Xs_C(i)*c_gamma+Jx)/clength,&
            (Xs_C(i)*s_gamma+Jy)/clength, (Zs_C(i)+Jz)/clength
    end do

end if

139 format('ZONE, T=',f8.4,' seconds Line JA''')
140 format('ZONE, T=',f8.4,' seconds Line JB''')
141 format('ZONE, T=',f8.4,' seconds Line JC''')
end subroutine crowfoot_visual_output

SUBROUTINE
crowfoot_initialization(Ax,Ay,Az,Bx,By,Bz,Cx,Cy,Cz,Jx,Jy,Jz,EA,W,L,CB,ratio)
!
! This subroutine is only used for timestep 1. It combines the crowfoot
! fairlead connection lines into 1 single, geometrically averaged line and then
! calculates an initial guess for the position of the junction point J.
! The guess is usually with 5 meters of the actual, converged position.
! In subsequent timesteps, the previous timestep's J-position is used for the
! initial guess.
!
!
IMPLICIT NONE
INTEGER,parameter :: N=1 ! Number of nodes where the line position and tension
! can be output (-)
integer, parameter :: double = 8
REAL(kind=double) :: CB ! Coefficient of seabed static friction drag
! (a negative value indicates no seabed) (-)
REAL(kind=double) :: EA ! Extensional stiffness of line (N)
REAL(kind=double) :: HA ! Eff. horizontal tension in line at anchor (N)
REAL(kind=double) :: HF ! Eff. horizontal tension in line at the fairlead (N)
REAL(kind=double) :: L ! Unstretched length of line (meters)
REAL(kind=double) :: s(N) ! Unstretched arc distance along line from anchor to
! each node where the line position and tension can
! be output (meters)
REAL(kind=double) :: Te(N) ! Effective line tensions at each node (N)
REAL(kind=double) :: Tol ! Convergence tolerance within Newton-Raphson
! iteration specified as a fraction of tension (-)
REAL(kind=double) :: VA ! Eff. vertical tension in line at the anchor (N)
REAL(kind=double) :: VF ! Eff. vertical tension in line at the fairlead (N)
REAL(kind=double) :: W ! Weight of line in fluid per unit length (N/m)
REAL(kind=double) :: X(N) ! Horizontal locations of each line node relative to
! the anchor (meters)
REAL(kind=double) :: XF ! Horizontal dist. betw. anchor and fairlead (meters)
REAL(kind=double) :: Z(N) ! Vertical locations of each line node relative to
! the anchor (meters)
REAL(kind=double) :: ZF ! Vertical dist. between anchor and fairlead (meters)

INTEGER :: i,conv
REAL(kind=double) :: L_B ! Amount of line sitting on seabed
REAL(kind=double) :: Ax,Ay,Az,Bx,By,Bz,Cx,Cy,Cz

```

```

REAL(kind=double)    :: Jx,Jy,Jz
REAL(kind=double)    :: p,A,B,XF_JA
REAL(kind=double)    :: cos_a,sin_a,cos_b,sin_b,tan_b,cos_c,sin_c,tan_c
REAL(kind=double)    :: L_JA,L_JBn,L_JBn1
REAL(kind=double)    :: T_JAx,T_JAy,T_JAz,T_JA
REAL(kind=double)    :: T_JBx,T_JBy,T_JBz,T_JB
REAL(kind=double)    :: T_JCx,T_JCy,T_JCz,T_JC
REAL(kind=double)    :: HF_JB,VF_JB,XF_JB,ZF_JB,fL,fLP
REAL(kind=double)    :: ratio      ! Ratio of lengths (L_JB/L_JA)

```

```

! Transform to JA frame

```

```

XF = dsqrt(((Bx+Cx)/2 - Ax)**2 + ((By+Cy)/2 - Ay)**2)

```

```

ZF = (Bz+Cz)/2 - Az

```

```

! Calculate HF and VF of single line using catenary code

```

```

! Divide line into N pieces

```

```

do i=1,N
  s(i) = L*i/N
enddo

```

```

Tol = 1.d-8

```

```

call Catenary ( XF, ZF, L , EA, W , CB, Tol, HF, &
  VF, HA, VA , N , s , X , Z , Te )

```

```

! Calculate position of J at p=(1-ratio)*L

```

```

L_B = L - VF/W      ! Amount of line on bed

```

```

p = (1-ratio)*L

```

```

if (L_B > 0.d0) then      ! Line sitting on bed

```

```

  A = L_B - HF/(max(CB,1.d-20)*W)

```

```

  B = W*(p - L_B)/HF

```

```

  if (p <= A) then

```

```

    XF = p

```

```

  else if (p <= L_B) then

```

```

    XF = p + CB*W/(2*EA)*(p**2 - 2*p*A + A*max(A,0.d0))

```

```

  else

```

```

    XF = L_B + HF/W*asinh(B) + HF*p/EA &
      + CB*W/(2*EA)*(-(L_B**2) + A*max(A,0.d0))

```

```

  end if

```

```

  if (p <= L_B) then

```

```

    ZF = 0.d0      ! This shouldn't happen

```

```

  else

```

```

    ZF = HF/W*(-1 + dsqrt(1 + ((VF + W*(p - L))/HF)**2)) &
      + p/EA*(VF-W*L + W*p/2) &
      + (VF - W*L)**2/(2*W*EA)

```

```

  end if

```

```

else      ! No line on seabed

```

```

  A = (VA + W*p)/HF

```

```

  B = VA/HF

```

```

  XF = HF/W*(asinh(A) - asinh(B)) + HF*p/EA

```

```

  ZF = HF/W*(dsqrt(1 + A**2) - dsqrt(1 + B**2)) + 1/EA*(VA*p + W/2*p**2)

```

```

end if

! Translate position of J into Earth coordinate system
cos_a = ((Bx+Cx)/2 - Ax)/dsqrt(((Bx+Cx)/2 - Ax)**2 + ((By+Cy)/2 - Ay)**2)
sin_a = ((By+Cy)/2 - Ay)/dsqrt(((Bx+Cx)/2 - Ax)**2 + ((By+Cy)/2 - Ay)**2)

Jx = XF*cos_a + Ax
Jy = XF*sin_a + Ay
Jz = ZF + Az

end subroutine crowfoot_initialization

SUBROUTINE crowfoot_force_block(Ax,Ay,Az,EA_A,W_A,L_JA,CB_A,&
  Bx,By,Bz,EA_B,W_B,L_JB,&
  Cx,Cy,Cz,EA_C,W_C,L_JC,&
  Jx,Jy,Jz,&
  HA_A,VA_A,HF_A,VF_A,HA_B,VA_B,HF_B,VF_B,HA_C,VA_C,HF_C,VF_C,&
  c_alpha,s_alpha,c_beta,s_beta,c_gamma,s_gamma,tolerance)
!
! This subroutine calculates the fairlead and anchor forces of the three
! component lines of the crowfoot mooring system.
!

implicit none

integer, parameter :: double = 8
integer, parameter :: N = 1
REAL(kind=double) :: CB_A ! Coefficient of seabed static friction
! drag (a negative value indicates no
! seabed) (-)
REAL(kind=double) :: EA_A,EA_B,EA_C ! Extensional stiffness of line (N)
REAL(kind=double) :: HA_A,HA_B,HA_C ! Effective horizontal tension in line at
! the anchor (N)
REAL(kind=double) :: HF_A,HF_B,HF_C ! Effective horizontal tension in line at
! the fairlead (N)
REAL(kind=double) :: VA_A,VA_B,VA_C ! Effective vertical tension in line at
! the anchor (N)
REAL(kind=double) :: VF_A,VF_B,VF_C ! Effective vertical tension in line at
! the fairlead (N)
REAL(kind=double) :: W_A,W_B,W_C ! Wt of line in fluid per unit lgth (N/m)
REAL(kind=double) :: L_JA,L_JB,L_JC ! Unstretched length of line (meters)
REAL(kind=double) :: Ax,Ay,Az ! Earth coordinates of A
REAL(kind=double) :: Bx,By,Bz ! Earth coordinates of B
REAL(kind=double) :: Cx,Cy,Cz ! Earth coordinates of C
REAL(kind=double) :: Jx,Jy,Jz ! Earth coordinates of J (current)
REAL(kind=double) :: c_alpha,c_beta,c_gamma ! Cosines of angles
REAL(kind=double) :: s_alpha,s_beta,s_gamma ! Sines of angles (only needed
! in horizontal plane)
REAL(kind=double) :: tolerance ! Convergence tolerance within Newton-
! Raphson iteration specified as a
! fraction of tension (-)

REAL(kind=double) :: p (N) ! Unstretched arc distance along line
! from anchor to each node where the
! line position and tension can be
! output (meters)
REAL(kind=double) :: Te (N) ! Effective line tensions at each node (N)

```

```

REAL(kind=double)  :: X_A(N),X_B(N),X_C(N) ! Horizontal locations of each line
! node relative to the anchor (m)
REAL(kind=double)  :: XF_A,XF_B,XF_C      ! Horizontal distance between anchor
! and fairlead (meters)
REAL(kind=double)  :: Z_A(N),Z_B(N),Z_C(N) ! Vertical locations of each line
! node relative to the anchor (m)
REAL(kind=double)  :: ZF_A,ZF_B,ZF_C      ! Vertical distance between anchor
! and fairlead (m)

integer :: i

! Translate all three lines into their respective local coord frames (XF, ZF)
XF_A = sqrt((Jx - Ax)**2 + (Jy - Ay)**2)
ZF_A = Jz - Az

XF_B = sqrt((Bx - Jx)**2 + (By - Jy)**2)
ZF_B = Bz - Jz

XF_C = sqrt((Cx - Jx)**2 + (Cy - Jy)**2)
ZF_C = Cz - Jz

! Calculate local forces (HF,VF,HA,VA) for all lines (using Jonkman's code)

! Line JA
! Divide line into N pieces
do i=1,N
  p(i) = L_JA*i/N
enddo

call catenary(XF_A,ZF_A,L_JA,EA_A,W_A,CB_A,tolerance,&
  HF_A,VF_A,HA_A,VA_A,N,p,X_A,Z_A,Te)

! Determine if any line sits on bed
! L_B = max(L_JA - VF_A/W,0.d0)

! Line JB
! Divide line into N pieces
do i=1,N
  p(i) = L_JB*i/N
enddo

call catenary(XF_B,ZF_B,L_JB,EA_B,W_B,-1.d0,&
  tolerance,HF_B,VF_B,HA_B,VA_B,N,p,X_B,Z_B,Te)

! Line JC
! Divide line into N pieces
do i=1,N
  p(i) = L_JC*i/N
enddo

call catenary(XF_C,ZF_C,L_JC,EA_C,W_C,-1.d0,&
  tolerance,HF_C,VF_C,HA_C,VA_C,N,p,X_C,Z_C,Te)

! Calculate Earth system x-y plane angles (well, cosines and sines, at least)
c_alpha = (Ax - Jx)/XF_A
s_alpha = (Ay - Jy)/XF_A

c_beta = (Bx - Jx)/XF_B
s_beta = (By - Jy)/XF_B

c_gamma = (Cx - Jx)/XF_C
s_gamma = (Cy - Jy)/XF_C

```

```
end subroutine crowfoot_force_block
```

```
subroutine crowfoot_forces_moments(Ax,Ay,Az,Bx,By,Bz,Cx,Cy,Cz,Jx,Jy,Jz, &
  x_rot,y_rot,z_rot,clength,surge,sway,heave,&
  CB,EA_in,W_in,L_JA,L_JB,L_JC, &
  Bfx,Bfy,Bfz,Cfx,Cfy,Cfz, &
  Bmx,Bmy,Bmz,Cmx,Cmy,Cmz, F_Tol)

!
! This subroutine is the main crowfoot solution subroutine. It returns the
! forces and moments of an individual crowfoot line/system
!

IMPLICIT NONE
integer, parameter :: double = 8
REAL(kind=double),parameter :: pi = 3.14159265

REAL(kind=double),intent(in) :: Ax,Ay,Az,Bx,By,Bz,Cx,Cy,Cz ! Input locations
REAL(kind=double),intent(inout) :: Jx,Jy,Jz ! Input locations
REAL(kind=double),intent(in) :: surge,sway,heave ! Motions of main object
REAL(kind=double),intent(in) :: x_rot,y_rot,z_rot ! Input centers of rot.
REAL(kind=double),intent(in) :: clength ! Reference length for dimensional
! to non-dimensional transforms
REAL(kind=double),intent(in) :: EA_in,W_in,L_JA,L_JB,L_JC ! Line properties
REAL(kind=double),intent(out):: Bfx,Bfy,Bfz,Cfx,Cfy,Cfz,Bmx,Bmy,Bmz,Cmx,Cmy,Cmz
! Forces and moments to be output
REAL(kind=double) :: rx_B,ry_B,rz_B,rx_C,ry_C,rz_C ! Components of vectors
! from center of rotation to fairleads B and C

REAL(kind=double) :: CB ! Coefficient of seabed static friction drag
! (negative value indicates no seabed) (-)
REAL(kind=double) :: EA(3) ! Extensional stiffness of line (N)
REAL(kind=double) :: HA(3),HA_n(3) ! Effective horizontal tension in line at
! the anchor (N)
REAL(kind=double) :: HF(3),HF_n(3) ! Effective horizontal tension in line at
! the fairlead (N)
REAL(kind=double) :: VA(3),VA_n(3) ! Effective vertical tension in line at
! the anchor (N)
REAL(kind=double) :: VF(3),VF_n(3) ! Effective vertical tension in line at
! the fairlead (N)
REAL(kind=double) :: W(3) ! Weight of line in fluid per unit length (N/m)
REAL(kind=double) :: L(3) ! Unstretched length of line (meters)
REAL(kind=double) :: A(3) ! Earth coordinates of A
REAL(kind=double) :: B(3) ! Earth coordinates of B
REAL(kind=double) :: C(3) ! Earth coordinates of C
REAL(kind=double) :: J(3),J_n(3) ! Earth coordinates of J
REAL(kind=double) :: delta_J(3) ! Vector of residuals
REAL(kind=double) :: co(3),co_n(3) ! Cosines of angles
REAL(kind=double) :: s(3),s_n(3) ! Sines of angles
REAL(kind=double) :: tolerance ! Convergence tolerance within Newton-Raphson
! iteration specified as a fraction of tens.

REAL(kind=double) :: omega(3,3) ! Current Jacobian (step n)
REAL(kind=double) :: omega_n(3,3) ! New Jacobian (step n+1)
REAL(kind=double) :: omega_inv(3,3) ! Inverse of Jacobian (step n)
REAL(kind=double) :: det ! Determinant of Jacobian
REAL(kind=double) :: omega_temp(3,3),numer,denom,omega_n_del_J(3)
! Intermediate Jacobian solution variables
```

```

REAL(kind=double)    :: d_J = 1.d-4 ! Amount to change J for initial Jacobian

REAL(kind=double)    :: F_Tol      ! Tolerance to check net force against
REAL(kind=double)    :: f(3),f_n(3) ! Net forces at J

INTEGER              :: i ! Counter variables

! BEGIN input variables
A(1) = Ax
A(2) = Ay
A(3) = Az

B(1) = Bx
B(2) = By
B(3) = Bz

C(1) = Cx
C(2) = Cy
C(3) = Cz

J(1) = Jx
J(2) = Jy
J(3) = Jz

L(1) = L_JA
L(2) = L_JB
L(3) = L_JC

! Line properties
do i = 1,3
  EA(i) = EA_in
  W(i)  = W_in
end do

! Tolerance for catenary subroutine
tolerance = 1.d-8

! Assume J for first step (otherwise, use the last known value)
if (J(1) == 0.d0 .and. J(2) == 0.d0 .and. J(3) == 0.d0) then ! First iteration
  call crowfoot_initialization(A(1),A(2),A(3),B(1),B(2),B(3),C(1),C(2),C(3), &
    J(1),J(2),J(3),EA(1),W(1),L(1)+L(2),CB,L(2)/L(1))
end if

! Create initial Jacobian
call crowfoot_force_block(A(1),A(2),A(3),EA,W,L(1),CB, &
  B(1),B(2),B(3),EA,W,L(2), &
  C(1),C(2),C(3),EA,W,L(3), &
  J(1),J(2),J(3), &
  HA(1),VA(1),HF(1),VF(1),HA(2),VA(2),HF(2),VF(2),HA(3),VA(3),HF(3),VF(3), &
  co(1),s(1),co(2),s(2),co(3),s(3),tolerance)

do i = 1,3
  ! Determine forces at moved J point
  J_n = J
  J_n(i) = J_n(i) + d_J

  call crowfoot_force_block(A(1),A(2),A(3),EA,W,L(1),CB, &
    B(1),B(2),B(3),EA,W,L(2), &

```

```

C(1),C(2),C(3),EA,W,L(3), &
J_n(1),J_n(2),J_n(3), &

HA_n(1),VA_n(1),HF_n(1),VF_n(1),HA_n(2),VA_n(2),HF_n(2),VF_n(2),HA_n(3),VA_n(3),HF
_n(3),VF_n(3), &
co_n(1),s_n(1),co_n(2),s_n(2),co_n(3),s_n(3),tolerance)

omega(1,i) = (HF_n(1)*co_n(1) + HA_n(2)*co_n(2) + HA_n(3)*co_n(3))/d_J &
- (HF(1)*co(1) + HA(2)*co(2) + HA(3)*co(3))/d_J

omega(2,i) = (HF_n(1)*s_n(1) + HA_n(2)*s_n(2) + HA_n(3)*s_n(3))/d_J &
- (HF(1)*s(1) + HA(2)*s(2) + HA(3)*s(3))/d_J

omega(3,i) = (-VF_n(1) + VA_n(2) + VA_n(3))/d_J &
- (-VF(1) + VA(2) + VA(3))/d_J

end do

! Begin iteration loop

do

! Evaluate f(J)
f(1) = HF(1)*co(1) + HA(2)*co(2) + HA(3)*co(3)
f(2) = HF(1)*s(1) + HA(2)*s(2) + HA(3)*s(3)
f(3) = -VF(1) + VA(2) + VA(3)

! Invert omega
det = omega(1,1)*(omega(3,3)*omega(2,2) - omega(3,2)*omega(2,3)) &
- omega(2,1)*(omega(3,3)*omega(1,2) - omega(3,2)*omega(1,3)) &
+ omega(3,1)*(omega(2,3)*omega(1,2) - omega(2,2)*omega(1,3))

omega_inv(1,1) = 1.d0/det*(omega(3,3)*omega(2,2) - omega(3,2)*omega(2,3))
omega_inv(1,2) = -1.d0/det*(omega(3,3)*omega(1,2) - omega(3,2)*omega(1,3))
omega_inv(1,3) = 1.d0/det*(omega(2,3)*omega(1,2) - omega(2,2)*omega(1,3))
omega_inv(2,1) = -1.d0/det*(omega(3,3)*omega(2,1) - omega(3,1)*omega(2,3))
omega_inv(2,2) = 1.d0/det*(omega(3,3)*omega(1,1) - omega(3,1)*omega(1,3))
omega_inv(2,3) = -1.d0/det*(omega(2,3)*omega(1,1) - omega(2,1)*omega(1,3))
omega_inv(3,1) = 1.d0/det*(omega(3,2)*omega(2,1) - omega(3,1)*omega(2,2))
omega_inv(3,2) = -1.d0/det*(omega(3,2)*omega(1,1) - omega(3,1)*omega(1,2))
omega_inv(3,3) = 1.d0/det*(omega(2,2)*omega(1,1) - omega(2,1)*omega(1,2))

! Calculate delta_J vector
do i = 1,3
delta_J(i) = -(omega_inv(i,1)*f(1) + omega_inv(i,2)*f(2) + &
omega_inv(i,3)*f(3))
end do

! Calculate J_n+1
J_n = J + delta_J

! Evaluate f(J_n+1)
call crowfoot_force_block(A(1),A(2),A(3),EA,W,L(1),CB, &
B(1),B(2),B(3),EA,W,L(2), &
C(1),C(2),C(3),EA,W,L(3), &
J_n(1),J_n(2),J_n(3), &
HA_n(1),VA_n(1),HF_n(1),VF_n(1),HA_n(2),VA_n(2),HF_n(2),VF_n(2), &
HA_n(3),VA_n(3),HF_n(3),VF_n(3), &
co_n(1),s_n(1),co_n(2),s_n(2),co_n(3),s_n(3),tolerance)

```

```

f_n(1) = HF_n(1)*co_n(1) + HA_n(2)*co_n(2) + HA_n(3)*co_n(3)
f_n(2) = HF_n(1)*s_n(1) + HA_n(2)*s_n(2) + HA_n(3)*s_n(3)
f_n(3) = -VF_n(1) + VA_n(2) + VA_n(3)

! Create new Jacobian
do i = 1,3
  omega_n_del_J(i) = omega(i,1)*delta_J(1) + omega(i,2)*delta_J(2) + &
    omega(i,3)*delta_J(3)
end do

denom = delta_J(1)**2 + delta_J(2)**2 + delta_J(3)**2

do i = 1,3
  numer = f_n(i) - f(i) - omega_n_del_J(i)
  omega_temp(i,1) = numer*delta_J(1)/denom
  omega_temp(i,2) = numer*delta_J(2)/denom
  omega_temp(i,3) = numer*delta_J(3)/denom
end do

omega_n = omega + omega_temp

if (maxval(abs(f_n),1) < F_tol) then ! Converged, so set values and exit
  ! Update final junction (J) position and forces
  Jx = J_n(1)
  Jy = J_n(2)
  Jz = J_n(3)

  Bfx = -HF_n(2)*co_n(2)
  Bfy = -HF_n(2)*s_n(2)
  Bfz = -VF_n(2)

  Cfx = -HF_n(3)*co_n(3)
  Cfy = -HF_n(3)*s_n(3)
  Cfz = -VF_n(3)

  ! Determine moments from forces
  ! Create rotation vectors. This requires translating the ship center of
  ! rotation into the Earth system.

  rx_B = B(1)-(x_rot + clength*surge)
  ry_B = B(2)-(y_rot + clength*sway)
  rz_B = B(3)-(z_rot + clength*heave)

  rx_C = C(1)-(x_rot + clength*surge)
  ry_C = C(2)-(y_rot + clength*sway)
  rz_C = C(3)-(z_rot + clength*heave)

  Bmx = (ry_B*Bfz-rz_B*Bfy)
  Bmy = (rz_B*Bfx-rx_B*Bfz)
  Bmz = (rx_B*Bfy-ry_B*Bfx)

  Cmx = (ry_C*Cfz-rz_C*Cfy)
  Cmy = (rz_C*Cfx-rx_C*Cfz)
  Cmz = (rx_C*Cfy-ry_C*Cfx)

  ! Produce some output to see what's happening
  !write(6,*) '***** Forces and Moments Due to Crowfoot Line *****'
  !write(6,320)Bfx,Bfy,Bfz
  !write(6,322)Cfx,Cfy,Cfz
  !write(6,321)Bmx,Bmy,Bmz

```

```

!write(6,323)Cmx,Cmy,Cmz
!write(6,*) '*****'

320 format('Bfx,Bfy,Bfz = ',3(3x,es12.4))
321 format('Bmx,Bmy,Bmz = ',3(3x,es12.4))
322 format('Cfx,Cfy,Cfz = ',3(3x,es12.4))
323 format('Cmx,Cmy,Cmz = ',3(3x,es12.4))
return
else
  HA = HA_n
  HF = HF_n
  VA = VA_n
  VF = VF_n
  co = co_n
  s = s_n
  J = J_n
  omega = omega_n
end if

end do

end subroutine crowfoot_forces_moments

SUBROUTINE mooring_thrust_torque(xxa,yya,zza,xxf,yyf,zzf,xr,yr,zr,&
  clength,surge,sway,heave,CB,EA,L,W,moor_forcecx,moor_forcecy,moor_forcecz,&
  moor_torquex,moor_torquey,moor_torquez)

!
! This subroutine is the main crowfoot solution subroutine. It returns the
! forces and moments of an individual 2-point line
!

IMPLICIT NONE

integer, parameter :: N = 1
integer, parameter :: double = 8

real*8 xr,yr,zr !Center of rotation
real*8 thrust,torque,dx,dy,dz,dmag,rx,ry,rz,clength
REAL(kind=double) :: surge,sway,heave ! Passed global motions of main object
REAL(kind=double) :: XXA ! x-coordinate for the anchor
REAL(kind=double) :: YYA ! y-coordinate for the anchor
REAL(kind=double) :: ZZA ! z-coordinate for the anchor
REAL(kind=double) :: XXF ! x-coordinate for the fairlead
REAL(kind=double) :: YYF ! y-coordinate for the fairlead
REAL(kind=double) :: ZZF ! z-coordinate for the fairlead
REAL(kind=double) :: moor_forcecx ! forces on ship due to mooring lines in x
REAL(kind=double) :: moor_forcecy ! forces on ship due to mooring lines in y
REAL(kind=double) :: moor_forcecz ! forces on ship due to mooring lines in z
REAL(kind=double) :: moor_torquex ! torque on ship due to mooring lines in x
REAL(kind=double) :: moor_torquey ! torque on ship due to mooring lines in y
REAL(kind=double) :: moor_torquez ! torque on ship due to mooring lines in z
REAL(kind=double) :: CB ! Coeff of seabed static friction (a negative
! value indicates no seabed) (-)
REAL(kind=double) :: EA ! Extensional stiffness of line (N)
REAL(kind=double) :: L ! Unstretched length of line (meters)
REAL(kind=double) :: W ! Wt of line in fluid per unit length (N/m)
REAL(kind=double) :: xf ! Local frame horizontal coordinate of
fairlead
REAL(kind=double) :: zf ! Local frame vertical coordinate of fairlead
REAL(kind=double) :: s(N) ! Unstretched arc distance along line from

```

```

                                ! anchor to each node
REAL(kind=double)  :: HA ! Eff horizontal tens in line at anchor (N)
REAL(kind=double)  :: HF ! Eff horizontal tension in line at the fairlead (N)
REAL(kind=double)  :: VA ! Eff vertical tension in line at the anchor (N)
REAL(kind=double)  :: VF ! Eff vertical tension in line at the fairlead (N)
REAL(kind=double)  :: X(N)! Horizontal locations of each line node relative to
                        ! the anchor (meters)
REAL(kind=double)  :: Z(N)! Vertical locations of each line node relative to the
                        ! anchor (meters)
REAL(kind=double)  :: Te(N) ! Effective line tensions at each node (N)

xf = dsqrt((xxf-xxa)**2+(yyf-yya)**2)
zf = zzf-zza

s(1) = L/2;

call Catenary (xf,zf,L,EA,W,CB,ld-8,HF,VF,HA,VA,N,s,X,Z,Te)

dx=xxa-xxf                                !vector from P1 to P2
dy=yya-yyf

! The z-axis of the earth system is parallel to the z-axis of the moor_force
! system. Therefore, the z-force seen at the fairlead is simply the negative of
! VF and HF needs to be split between x and y in a two-dimensional, xy plane.

dmag = dsqrt(dx**2 + dy**2)
dx=dx/dmag                                !normalized vector from P2 to P1
dy=dy/dmag

moor_forcecx=dx*HF                        !thrust in x,y,z in ship coordinates
moor_forcecy=dy*HF
moor_forcecz=-VF

! xxf/yyf/zzf are in Earth coords, but the ship center of rotations are in ship
! coords. Convert these to Earth coords for a proper position vector

rx=xxf-(xr + clength*surge)               !vector from center of rotation to P1
ry=yyf-(yr + clength*sway)
rz=zzf-(zr + clength*heave)

moor_torquecx=(ry*moor_forcecz-rz*moor_forcecy) !adds to torque the thrust comp
moor_torquecy=(rz*moor_forcecx-rx*moor_forcecz)
moor_torquecz=(rx*moor_forcecy-ry*moor_forcecx)

write(6,*) '*****'
write(6,*) 'total forces and torque due to the mooring line'
write(6,520)moor_forcecx,moor_forcecy,moor_forcecz
write(6,530)moor_torquecx,moor_torquecy,moor_torquecz
write(6,*) '*****'

520 format('fx,fy,fz = ',3(3x,es12.4))
530 format('mx,my,mz = ',3(3x,es12.4))

END SUBROUTINE mooring_thrust_torque

```